

Lattice Mismatched Epitaxy of Heterostructures
for Non-nitride Green Light Emitting Devices
by

Michael James Mori

B.S. in Materials Science and Engineering
Stanford University, 2001

M.S. in Materials Science and Engineering
Stanford University, 2002

Submitted to the Department of Materials Science and Engineering in Partial Fulfillment
of the Requirements for the Degree of

Doctor of Philosophy in Electronic Materials
at the
Massachusetts Institute of Technology

June 2008

© 2008 Massachusetts Institute of Technology. All rights reserved.

Signature of Author: _____
Department of Materials Science and Engineering
May 21st, 2008

Certified by: _____
Eugene A. Fitzgerald
Merton C. Flemings-SMA Professor of Materials Science and Engineering
Thesis Supervisor

Accepted by: _____
Samuel M. Allen
POSCO Professor of Physical Metallurgy
Chair, Departmental Committee on Graduate Students

Lattice Mismatched Epitaxy of Heterostructures for Non-nitride Green Light Emitting Devices

by

Michael James Mori

Submitted to the Department of Materials Science and Engineering on
May 21st, 2008, in Partial Fulfillment of the Requirements for the Degree
of Doctor of Philosophy in Electronic Materials

ABSTRACT

In this project, we implement modern metal organic chemical vapor deposition (MOCVD) technology to fabricate monolithic platforms which integrate traditionally incompatible materials with the ultimate goal of achieving high brightness green to amber light emitting diodes (LEDs) and laser diodes (LDs). Unconventional compositions of aluminum indium gallium phosphide (AlInGaP), with lattice constants less than that of GaAs, offer improved electrical and optical characteristics over commonly used GaAs-matched material. Also, integration of optical III-V material on the CMOS platform has long been a technological goal, and these compositions of AlInGaP are amenable to monolithic integration on the (100) Si platform. In this thesis, we pioneer technology to integrate high quality, novel AlInGaP alloys on III-V substrates (and elsewhere, this technology is successfully extended for III-V integration on (100) Si).

We first focus on creating a virtual substrate upon which any lattice constant intermediate to GaAs and GaP is available. Large amounts of lattice mismatch are ultimately relaxed through incremental introduction of strain in compositionally graded epitaxial layers, thus breaking the typical lattice-matched constraint of semiconductor systems. Tensile relaxed gallium arsenide phosphide (GaAsP) graded layers yield virtual substrates with extremely low threading defect densities ($\rho_t=10^4\text{cm}^{-2}$), while extremely thin, 1.3 μm compressively graded GaAsP buffers also yield low thread densities ($\rho_t=10^5\text{cm}^{-2}$). The lack of phase separation defects along with the atomically smooth nature of the tensile films leads to suppression of dislocation nucleation and efficient dislocation glide which together facilitate complete strain relaxation with minimal escalation of ρ_t . Next we present microstructural studies of AlInGaP lattice-matched to these virtual substrates. Atomic mechanisms of formation of defects including CuPt-B atomic order, phase separation defects and GaAsP surface undulation are understood. A competitive two-step model which describes their creation at the growth surface and subsequent destruction in a high diffusivity subsurface layer makes possible intuitive adjustment of MOCVD growth parameters for defect-free AlInGaP heterostructures. Finally, fabrication of LEDs is discussed. As predictions show, electroluminescence color ranges from green (570nm) to amber (606nm). These structures hold promise for LDs and high efficiency LEDs at wavelengths as low as 550nm.

Thesis Supervisor: Eugene A. Fitzgerald

Title: Merton C. Flemings-SMA Professor of Materials Science and Engineering

Table of Contents

List of Figures	5
List of Tables	10
Acknowledgements	11
Chapter 1 Motivation and Organization	13
1.1 The Green GaP	14
1.2 The Si Optoelectronic Integrated Circuit	18
1.3 Organization of Thesis	23
Chapter 2 Materials Design	24
2.1 Material Selection	25
III-V vs. Other Semiconductors	25
Band Gap.....	26
Lattice Constant.....	27
2.2 Lattice Mismatched Epitaxy.....	28
Working with Dislocations.....	31
Compositional Grading	36
2.3 Properties of AlInGaP and GaAsP	38
2.4 Device Design	45
Device Active Layer.....	45
Virtual Substrate.....	46
2.5 Engineering the Band Structure	47
Chapter 3 MOCVD Growth and Characterization	50
3.1 Introduction	51
3.2 MOCVD Process.....	52
MOCVD Reactors	52
Reactor subsystems	55
GaAsP growth	58
3.3 Characterization	60
TEM	60
XRD	61
PL	61
CL.....	62
AFM	62
EPD	62
Chapter 4 Virtual Substrates for Si to Ge Lattice Constants	63
4.1 Introduction	64
4.2 Experimental Method.....	65
4.3 Graded (Al)InGaP, Branch Defects.....	68
4.4 Graded GaAsP, Removal of Branch Defects	72
4.5 Conclusions	82
Chapter 5 Microstructural Control of (Al)InGaP on GaAsP	84
5.1 Introduction	85
5.2 Method and Results.....	85
5.3 Ordering	86
5.4 Phase Separation	94

5.5 GaAsP/InGaP Interface	105
5.6 Conclusions	112
Chapter 6 Device Fabrication	113
6.1 Introduction	114
6.2 Device Modeling	116
6.3 Device Fabrication and Testing.....	123
6.4 Device Performance	126
6.5 Conclusions and Future Work.....	131
Chapter 7 Results Summary, Suggestions for Future Work	133
7.1 Overview	134
7.2 Summary of Results	134
Virtual Substrate Technology.....	134
Microstructure Studies	135
Fabrication of Light Emitting Devices.....	136
Integration of GaAsP on SiGe.....	136
7.3 Suggestions for Future Studies.....	137
Appendix A Example GaAsP Growth Sheet.....	140
Appendix B Mathematica Code for InGaP strained QW Model.....	142
References	161

List of Figures

Figure 1.1 Device luminous performance compared to the CIE eye sensitivity curve. Adapted from OIDA 2002 and McGill ^{2, 3}	15
Figure 1.2 Wall plug (electron to photon conversion) efficiency for a variety of demonstrated LEDs (spots) and LDs (surface and edge emitters). Note the deficiency in the yellow region. Reproduced from OIDA 2002 ²	16
Figure 1.3 A recent summary of external quantum efficiencies of state of the art devices, also showing deficiency in the yellow-green part of the visible spectrum. Reproduced from Phillips ⁴	16
Figure 1.4 Absorption coefficient as a function of wavelength for a variety of semiconductors. Reproduced from Pierret ⁵	21
Figure 2.1 Band gap as a function of lattice parameter for many semiconducting materials. Ternary materials are represented by the lines connecting the binary materials data points. Figure adapted from poster by V.G. Keramidis and R.E. Nahory.....	25
Figure 2.2 A schematic representation of mismatched epitaxy. On the left is sub-critical thickness film that is therefore coherently strained. The right drawing represents the relaxation that occurs in films thicker than h_c . Figure reproduced from McGill ³	30
Figure 2.3 Several configurations of dislocations upon nucleation in a mismatched film. Note that the dislocation can only terminate at the crystal edge or on a heterogeneous defect. Portions of dislocations incline to the surface and are called threading dislocations. Image courtesy of McGill ³	32
Figure 2.4 Schematic of a misfit dislocation gliding through a mismatched film. Portions that extend through the surface of the film, threading dislocation, are deleterious to device performance. Figure reproduced from Pitera ¹⁹	34
Figure 2.5 Dislocations interact forcefully with features in the crystal. To avoid high threading dislocation densities, we wish to minimize interactions that might prevent effective dislocation glide and crystal relaxation. Figure reproduced from Pitera ¹⁹	35
Figure 2.6 a) Schematic and b) XTEM of the metamorphic graded buffer where GaP is graded to GaAs. Note that only a single dislocation is shown but that in reality many dislocation recycle threads to relax strain at many interfaces thus maximizing misfit length for threading length.....	37
Figure 2.7 a) PVTEM and b) XTEM of an InGaP graded buffer misfit dislocation array. Images from ³	37
Figure 2.8 Band gap as a function of lattice parameter for the AlInGaP quaternary system. Data obtained from Vurgaftman ⁷	38
Figure 2.9 The zincblende crystal structure consists of two interpenetrating FCC lattices. Reproduced from Stringfellow ³⁶	39
Figure 2.10 Calculated minimum band gap as a function of lattice constant for the quaternary AlInGaP system. Constant In-composition lines are shown in increments of 10% and constant Al-composition lines are in increments of 20%.	44
Figure 2.11 Energy vs. momentum schematic for a) direct ($E_g=E_0$) and b) indirect ($E_g \neq E_0$) semiconductors. When the indirect (X) band minimum is near or lower than direct (Γ) minimum, fewer carriers will be able to recombine radiatively. Reproduced from McGill ³	44

Figure 2.12 Schematic of band structure for an entire device integrated on a transparent virtual substrate (adapted from McGill ³).	47
Figure 2.13 The three possible type of band alignment at a heterojunction. For the SQW structure, we desire type I alignment.	48
Figure 2.14 Some example results of the computer model. Here we have specified that the cladding material, $\text{In}_{.29}\text{Ga}_{.71}\text{P}$, is lattice matched to the substrate and that the thickness and composition of the $\text{In}_x\text{Ga}_{1-x}\text{P}$ QW is varied.	49
Figure 3.1 Schematic of LPMOCVD reactor, not drawn to scale. Drawing courtesy of C. Dohrman.	53
Figure 3.2 Photograph of the close-coupled showerhead, flip-top reactor in the opened position. Note that pyrometry and reflectivity data are taken through the four ports visible in the showerhead. This reactor design enables excellent control over temperature and compositional profiles.	54
Figure 3.3 The composition calibration curve for GaAsP grown at 725°C and a V/III ratio of 100 is shown. Using equation 3.1 to fit experimentally derived composition calibration data, we get excellent predictability of GaAsP compositional control.	60
Figure 4.1 Threading dislocation density (ρ_t) as a function of final composition in the graded buffer. The system with the lowest ρ_t is the growth temperature-optimized, undoped InGaP. Set includes data from Kim ⁴⁶	69
Figure 4.2 Plan view TEMs of high quality temperature-adjusted InGaP, graded to a final composition of 24%In with ρ_t of $2.3 \times 10^6 \text{cm}^{-2}$. Note the even contrast throughout these images indicating the presence of no branch defects.	70
Figure 4.3 a) PVTEM of constant temperature AlInGaP graded buffer. Note the bright branched regions of contrast, the phase separation defects which impede dislocation glide. These branch defects elevated ρ_t to a relatively high value of $1.5 \times 10^7 \text{cm}^{-2}$. b) Applying the InGaP temperature optimization to AlInGaP reduced the branch defect strength and lowered ρ_t to $3.7 \times 10^6 \text{cm}^{-2}$. Pileups of dislocations such as the one pictured here account for a majority of the total thread density.	70
Figure 4.4 PVTEM image of tensile relaxed GaAsP with lattice matched InGaP layer on top. Note the lack of branch defects.	73
Figure 4.5 Comparison of ρ_t as a function of lattice constant for InGaP, tensile and compressive GaAsP. There is very little threading dislocation escalation in the GaAsP samples.	75
Figure 4.6 PVTEM image of tensile relaxed InGaP layer on high quality GaAsP graded buffer. Note the high density of threading dislocations and area of stacking faults.	76
Figure 4.7 5 μm square AFM scan of a typical on-axis (001) GaAsP tensile graded buffer showing atomic steps of approximately 4Å height. RMS roughness is 0.78nm.	78
Figure 4.8 Cross section, <022> bright field TEM of a) tensile graded GaAsP exhibiting a crack. b) Cracks can be avoided through slower grade rates but this requires the growth of relatively thick layers.	79
Figure 4.9 Cross section, <022> bright field TEM of compressively graded GAsP with P-fraction of 0.55 at top and GaP substrate on bottom. No phase separation or cracking is apparent.	80

Figure 4.10 Comparison of AFM scans on three metamorphic platforms. Each sample has relaxed identical absolute amounts of strain. All images are set at the same length scales.....	81
Figure 5.1 Perfect ordering in $\text{In}_5\text{Ga}_5\text{P}$ consists of alternation of the In and Ga species on $\{111\}$ planes. This additional crystal symmetry lowers the band gap of the crystal. Reproduced from Zunger ⁵⁹	88
Figure 5.2 Transmission Electron Diffraction (TED) allows simple detection of CuPt order. The presence of two types of superspots in a), the $[110]$ TED pattern, indicates CuPt-B order of both variants. From the $[1\bar{1}0]$ zone axis TED pattern in b), the lack of superspots indicates no CuPt-A order.....	89
Figure 5.3 Transmission electron diffraction images of InGaP. The presence of superspots in a) indicates CuPt-B ordering, the absence of superspots in b) indicates disorder, and the weakness of the superspots in c) indicates weaker order. The samples shown in a) and b) were grown at 650°C but b) also included a small flow of TMSb as surfactant. Sample c) was grown at 725°C	89
Figure 5.4 Plot of CL peak wavelength as a function of In fraction in InGaP and growth conditions. Also shown are traces for the expected wavelength of direct and indirect transitions, as predicted in the literature. Growth at 725°C results in higher band gap material and shorter wavelength CL as compared to 650°C growth.	91
Figure 5.5 20K PL intensity as a function of wavelength for $\text{In}_{0.33}\text{Ga}_{0.67}\text{P}$ grown at 650°C with and without TMSb as surfactant and at 725°C . Note that the high temperature blue-shifted the peak while surfactant broadened the peak, probably because of Sb incorporation. The small shoulder at 580nm on the 650°C sample is probably intensity from ordered domains with less order and higher band gap than other domains in the sample.	93
Figure 5.6 Cross section $\langle 022 \rangle$ bright field TEM of $\text{In}_{0.22}\text{Ga}_{0.78}\text{P}$ heterostructure on lattice-matched $\text{GaAs}_{0.46}\text{P}_{0.54}$ graded buffer on GaP. Dark streaks of contrast in the InGaP are short-range order defects and degrade the optical quality of the heterostructure.	96
Figure 5.7 Comparison of CL intensity of similar heterostructures where phase separation defects are uncontrolled (dashed line, sample shown in Figure 5.6) and have been removed (solid line).....	96
Figure 5.8 Comparison of similar structures grown at 725°C and 650°C . The sample in a) contains phase separation defects which begin at an interface where growth was halted for a ten-minute <i>in-situ</i> anneal. In b), 650°C growth did not result in separation defects. Figure 5.6 shows a sample at identical composition grown entirely at 725°C with no <i>in-situ</i> anneal.	100
Figure 5.9 Comparison of InGaP grown at 725°C under a) high and b) low V/III. Suppression of surface diffusivity at high V/III prevents the formation of short-range order.....	101
Figure 5.10 Comparison of V/III effect on defects in InGaP at higher In fraction (compared to Figure 5.9), where the alloy is more susceptible to phase separation defects. Note the higher V/III ratios as well as the contrast near the InGaP/GaAsP interface in b) which suggests minor phase separation defects despite the high V/III.	101
Figure 5.11 Comparison of InGaP grown under identical conditions a) without and b) with a small flow of TMSb.....	102

Figure 5.12 Phase diagram of InGaP, indicating the sensitivity of the InGaP solid to composition at In-fractions less than about 0.3. The melting point (solidus) of InGaP reveals much about the chemical nature of the alloy. Reproduced from Stringfellow³⁶. 103

Figure 5.13 Phase space for formation of short-range order defects. Reactor limitations prevent growth in the upper right quadrant of the plot, the region where we expect the highest quality material. By maintaining high V/III and reasonable growth rates ($\sim 5\text{\AA}/\text{s}$) we can avoid short-range order in our system. 104

Figure 5.14 Cross section $\langle 022 \rangle$ bright field TEM of a) unprotected GaAsP compressive graded buffer. During the post-growth cool down, a fixed ratio of AsH_3 and PH_3 gas was flowed, resulting in undulation of the surface, as shown in b). 105

Figure 5.15 Growth of InGaP on top of undulated or islanded GaAsP results in highly defective growth unsuitable for optical device fabrication..... 106

Figure 5.16 Three images of a GaAsP film capped with incomplete 25\AA GaAs film and cooled under AsH_3 overpressure. In a), the AFM surface height profile shows the distribution and shape of the As-rich GaAsP islands. In b), cross section TEM shows the formation of misfit dislocations underneath the islands which are also visible in c) plan view TEM of the same sample..... 107

Figure 5.17 Compressive GaAsP buffer graded to final composition of $\text{GaAs}_{0.45}\text{P}_{0.55}$ with high quality lattice-matched $\text{In}_{0.22}\text{Ga}_{0.78}\text{P}$ cap..... 109

Figure 5.18 High resolution TEM of a compressively strained 25\AA GaAs protective layer on a GaAsP graded buffer. This thin barrier allows the growth of high quality InGaP heterostructures lattice-matched to GaAsP virtual substrates. 110

Figure 6.1 Band gap as a function of lattice constant for several material systems. AlInGaP offers wide band gap as well as a lattice constant amenable to integration on Si and Ge. 115

Figure 6.2 Schematic of an example light emitting structure. The virtual substrate can be adapted for any AlInGaP composition required up to the GaAs lattice constant. A lattice-matched SCH and strained QW provide optical and electrical confinement. 118

Figure 6.3 Some example results of the computer model. Here we have specified that the cladding material, $\text{In}_{.29}\text{Ga}_{.71}\text{P}$, is lattice matched to the substrate and that the thickness and composition of the $\text{In}_x\text{Ga}_{1-x}\text{P}$ QW is varied. 119

Figure 6.4 Band alignment (VB referenced to InSb) as a function of lattice constant for the entire AlInGaP system. The type-II alignment between GaP and AlP and type-I offset between GaP and InP cause a kink in the CB band edge with composition. Note that for the widest direct band gap InGaP (near 5.58\AA) addition of Al lowers the CB edge. 120

Figure 6.5 20K PL intensity for two samples with different structures designed to demonstrate the range of accessible wavelengths. The left trace is a sample which contains three quantum wells and three characteristic peaks while the right trace has a single quantum well. 121

Figure 6.6 Ar-ion laser filtered photographs of 20K PL of various InGaP heterostructures showing luminescence ranging from 562nm (top left) to 584nm (lower right). 121

Figure 6.7 Predicted band schematic of the alignment test sample. Type-I transitions are expected at 566nm while type-II are expected at 580nm. 122

Figure 6.8 The observed CL emission of the sample indicated in Figure 6.7. The primary emission is precisely where expected, at 566nm and there is no significant peak at 580 or longer, indicating that the alignment is likely to be type-I.	123
Figure 6.9 Cross section <022> bright field TEM images of two device heterostructures. In a), and AlInGaP-based SCH structure is shown while b) is an Al-free InGaP strained QW.	124
Figure 6.10 Schematic of top contact ridge waveguide laser showing wet etched mesas, SiO ₂ passivation and lift-off metallization.	125
Figure 6.11 Comparison of I-V characteristics of a diode subjected to a 30s anneal at 450°C or 500°C. For comparison, also shown is data for conduction across the 500°C annealed device, from n to n contacts.	127
Figure 6.12 Photomicrographs of electroluminescence as seen from the top side of the devices. Colors correspond to a) 570nm (green), b) 575nm (yellow-green) and c) 606nm(amber).	128
Figure 6.13 Normalized spectra for a variety of devices tested, demonstrating access to a wide range of the visible spectrum with our very flexible device platform.	128
Figure 6.14 LED spectra from two similar devices with ordered domains in the QW, due to a relatively low growth temperature of 650°C. Preferential recombination in the lower bandgap ordered regions results in a primary “red” peak as compared to the secondary “blue,” disordered shoulder. Both devices consisted of In _{0.32} Ga _{0.68} P QWs with slightly varied cladding compositions.	129
Figure 6.15 LED spectra from two devices with disordered QWs grown at 725°C. Note the large blue-shift of the peaks compared to those in Figure 6.14 despite that fact that their QWs contain significantly more In (579nm peak from a In _{0.38} Ga _{0.62} P QW and 592nm from a In _{0.36} Ga _{0.64} P QW).	130
Figure 6.16 LED spectra from several devices from the same wafer where a composition gradient across the wafer resulted in tensile mismatch in the InGaP and incorporation of a high density of defects. Changes in In fraction of just 3-4% result in large shifts in color, of greater than 15nm.	131

List of Tables

Table 2.1 Lattice constants of some semiconductors of interest.....	29
Table 2.2 Lattice constant as a function of temperature for several III-V binary compounds. Data based on recommendations by Vurgaftman ⁷	41
Table 2.3 Γ and X band bowing parameters for several III-V ternary compounds. Data based on recommendations by Vurgaftman ⁷	41
Table 2.4 Compilation of Varshni parameters for the temperature dependence of the Γ and X bands of GaP, InP and AlP. Data based on recommendations by Vurgaftman ⁷	42
Table 4.1 Description of several GaAsP grades, showing relationship of grade rate, cracking, RMS roughness and ρ_t	82

Acknowledgements

First, I would like to thank my advisor, Professor Gene Fitzgerald, for providing me the opportunity to do this thesis work. I remember being challenged and inspired by Gene from the first day I met him; he has always been able to instill confidence in my own ability to overcome any research obstacle and he had me running from day one. Gene's genuine optimism and friendliness constantly remind me to dream big and never stop! I will always be grateful to Gene as my guide through graduate school research.

I would like to offer thanks to my thesis committee, Professors Rajeev Ram and Sam Allen. As their student, I have learned more from them than they probably know. I was attracted by their personalities, teaching style and their love of what they do as well as by their academic prowess. It has been an honor to know them during my time at MIT.

I remain convinced that the Fitzgerald Research Group is one of the healthiest at MIT. Thanks to our strong sense of camaraderie, we have always been united in our fight against "the machines" which always seem intent on stopping research in its tracks. My extended stay at MIT has given me the opportunity to meet an unusually large portion of the many Fitzgerald-ites, and each has added something valuable to my experience. I wish I could write something about everyone here, but then my acknowledgements would be longer than my thesis. Graduate school is all about the experience, and I think the experience is all about the people we meet. Roughly in order of appearance in my MIT career: Minjoo "Larry" Lee, Nate Quitariano, Lisa McGill, Juwell Wu, Gianni Taraschi, Nava Ariel, Arthur Pitera, Charles Cheng, John McGrath, Saurabh Gupta, Carl Dohrman, David Isaacson, Bai Yu, Ken Lee, Mayank Bulsara, Kamesh Chilukuri, Haryono Hartono Steve Boles, Chengwei Cheng, Yang Li, Charles Ho and Nan Yang.

Larry, thanks for helping me keep my feet on the ground and reminding me what's most important in life. You inspired my TEM ability! Lisa, you give meaning to the expression "standing on the shoulders of giants." Thank you for teaching me about AlInGaP and MOCVD, I couldn't have asked for a better mentor. See you in a couple of months. Nate, thank you for reminding me to laugh at life sometimes (loudly, even). Carl, I feel like we were in this together the whole way and I'm glad we're ending it together. Thanks for sticking it out with me. Ken, I think this thesis probably deserves your name on it as much as mine. Thanks for lending me the brain power! Kamesh, you taught me that rallying the resources gets things done! Thanks for leading such a great and fun project. Haryono, I will always remember our time together, you inspire me to keep plugging away. Bai Yu, Steve, Li, Chengwei, Charles and Nan, thanks for being an awesome research group.

As I have always said, grad school is fun because you get to play with really big, expensive machines that do some really amazing things. I want to acknowledge all of the people that kept those machines running—sometimes I envy your jobs. Yong Zhang, Tony Garratt-Reed and Mike Frongillo kept the TEMs and ion mills in top shape. Peter Kloumann, Joe Adario and Scott Speakman at MIT along with Prof. Frans Spaepen, Alex Donohue, Frank Molea and Richard Schalek at Harvard made XRD possible. Libby Shaw ran the AFM for us and Henry Choy built our PL setup. David Bono from the DMSE Undergrad Teaching Lab deserves kudos for helping on a number of fronts, but mostly for keeping our CL equipment in order. Thanks to Jurgen Michel for helping with the low

temp CL measurements as well. Also, thanks to Jen Yu from the Bulovic Group for providing us with the LED spectra.

I would like to acknowledge the sources of funding for this project: The Department of Defense NDSEG fellowship and Intel Foundation Ph.D. fellowship allowed me and my family to survive while MARCO IFC and ARO provided funding for the research.

Lastly and most importantly, I want to thank my family for their support and understanding. My family is my life. To my parents, Frank and Susan Mori who made everything possible (I really mean that): Mom, I miss you and I hope you're watching us now, and Dad, we're coming home soon! To Joy: I'm glad you're here, I cannot imagine living life without you. Toby: I live for your smile. Della: your arrival could hardly have been more well-timed, I can't wait to get to know you. I dedicate this work to all of you.

Chapter 1 Motivation and Organization

1.1 The Green GaP

Ever since their introduction into the commercial market in the middle of the 20th century, semiconductor-based light emitters have been sold for a huge range of applications, from telecommunications (infrared lasers) to indicator lights (visible light emitting diodes or LEDs). Compound semiconductors are uniquely situated as the material of choice for solid-state light emitters because of their potential for extremely efficient conversion of electrical to optical energy. III-V materials have proven to be quite flexible and reliable in their application. Typically, compounds with direct band gap which are lattice-matched to commercially available substrates are used. The availability of colors and the performance of devices is dictated by the electrical properties of the available semiconductor alloys. Great progress has been made and a wide range of high performance devices have been marketed.

Currently there is a strong thrust in the research community to develop white visible light emitters for energy efficient lighting applications. Since the emitted spectrum of most semiconductor-based devices is relatively narrow (i.e. pure in color), one primary obstacle to the white solid-state light is how to broaden the emitted spectrum to make it appear white. State of the art devices typically utilize a single material to generate photons from the high energy side of the visible spectrum (near-UV or blue) and down-convert most of the photons to a range of wavelengths using a phosphor. The efficiency of this paradigm relies on the conversion of the phosphor and hence has fundamental limits. Estimates suggest that UV- or blue-pumped phosphors can achieve efficacies of up to 203lm/W or 263lm/W, respectively, but there is no physical limitation to color-mixed lighting achieving over 400lm/W¹. A more energy efficient way to

produce the broad white spectrum is to mix two or more colors to give the appearance of white, in the same way color is generated in today's television and video displays. In such a light source, the overall efficiency would rely only on the external quantum efficiencies of the constituent devices.

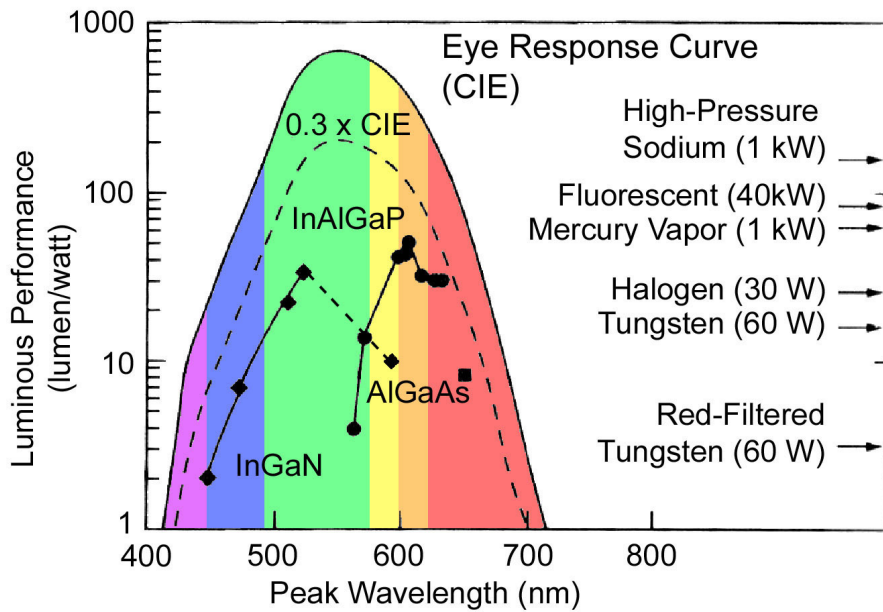


Figure 1.1 Device luminous performance compared to the CIE eye sensitivity curve. Adapted from OIDA 2002 and McGill^{2,3}.

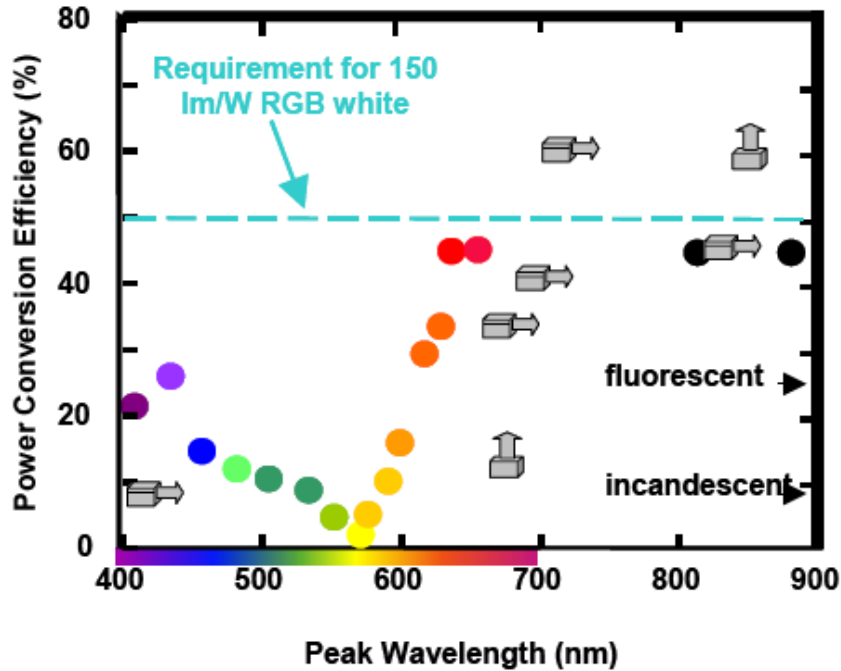


Figure 1.2 Wall plug (electron to photon conversion) efficiency for a variety of demonstrated LEDs (spots) and LDs (surface and edge emitters). Note the deficiency in the yellow region. Reproduced from OIDA 2002².

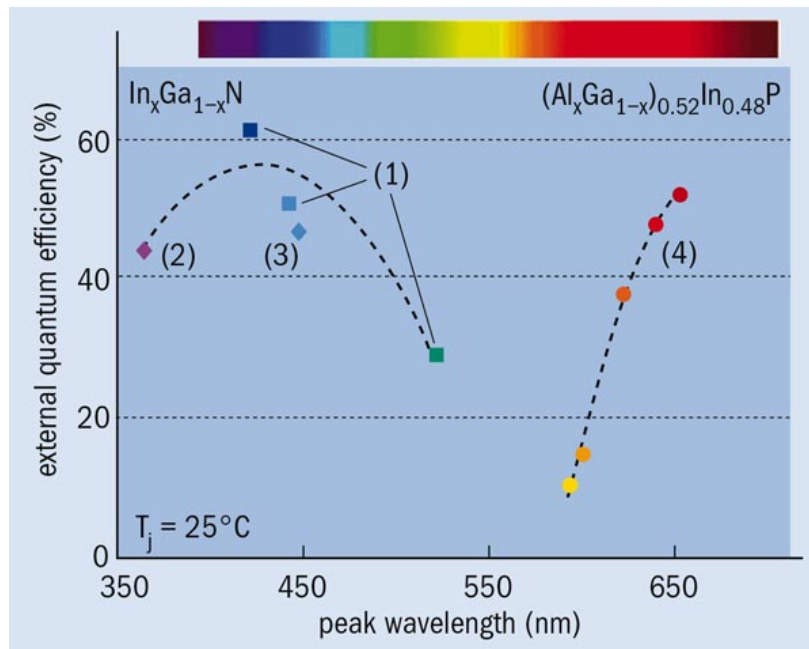


Figure 1.3 A recent summary of external quantum efficiencies of state of the art devices, also showing deficiency in the yellow-green part of the visible spectrum. Reproduced from Phillips⁴.

While the current market-dominating materials for blue and red LEDs perform quite well, materials for green emission lag behind; this is often referred to as the “Green Gap”^{2,4} and is shown in Figure 1.1, Figure 1.2 and Figure 1.3 in various forms. As (Al)InGaN-based devices reach into the green from the blue side of the spectrum, and as (Al)InGaP-based devices reach green from red, efficiency drops dramatically. As a result, nitride devices tend to be blue-green while phosphides tend to be yellow-green. These wavelengths are especially significant because of the sensitivity of the human eye to these colors. Deviations of as little as 2nm in wavelength are discernable, and broad spectral linewidths of devices are perceived as undersaturated and have poor color purity. With improved material we are theoretically able to attain higher efficiency and narrower spectral linewidth. Additionally, no yellow, yellow-green or pure green III-V semiconductor lasers are known to have been previously demonstrated. An efficient yellow-green or green emitter with a comparable efficiency to blue and red emitters does not yet exist.

In the GaN material system, green emission can be achieved through the use of InGaN quantum well or quantum dot layers. However, despite the very short minority carrier lifetimes induced by the quantum wells, the high dislocation density present in GaN layers combined with the inability to add enough indium (In) to form deep quantum wells (due to InGaN-GaN lattice-mismatch and thermodynamic constraints) can result in lower efficiency as compared with typical blue emission performance.

The other material system commonly considered for yellow-green emission is AlInGaP, at compositions lattice matched to GaAs (lattice constant of about 5.565Å). These alloys are traditionally used to produce red to yellow light emitters. As the band

gap of the active material is increased (by increasing the Al fraction of the alloy) the emitted wavelength becomes smaller (greener, rather than redder), but the limited band gap of the cladding material reduces the available electronic and optical confinement, making them less efficient. Green-emitting AlInGaP devices that are lattice-matched to GaAs also have poor internal quantum efficiency due to their proximity to the indirect-direct band gap crossover, as well as due to oxygen-related defects.

One motivating factor for this thesis project is our desire to improve light emitting materials in the green range. By expanding the range of available materials, we strive to demonstrate methods to attain high efficiency, pure green devices. We also strive to fabricate the first yellow and yellow-green lasers.

1.2 The Si Optoelectronic Integrated Circuit

Semiconductor optical devices offer great promise to the microelectronics industry, for they will prolong Moore's Law exponential growth in performance of CMOS technology over the next several decades. Traditionally, scaling down the size of the components in CMOS circuits has increased microelectronic performance, but as individual devices reach atomic dimensions, scaling size no longer makes them faster. Unlike transistors which speed up as they shrink, electrical interconnects slow as they are scaled due to higher RC line delays (smaller wire cross section increases resistance and capacitance). By removing the electrical interconnect from the circuits and instead transmitting signals by light in an optical interconnect, we can continue to increase performance through scaling. This concept, the optoelectronic integrated circuit (OEIC), hybridizes electronic and photonic technologies so that that today's high performance

CMOS circuits can continue to exist at the cutting edge of technology. Since hybridization integrates traditionally separate materials, the obstacles to the OEIC are fundamentally materials related.

This thesis project is largely motivated by the need to develop an essential piece of the OEIC: bringing light onto the Si platform. The realization of an optoelectronic integrated circuit will require a bright and efficient photon source, preferably laser as opposed to LED. This source could be directly driven or modulated externally, but with more flexible the design, fewer additional components are needed and OEIC design is simplified. The current research focus is on creating an efficient, small, electrically driven laser which can be manufactured on the wafer scale in a method compatible with current CMOS process technology. The poor light emitting qualities of silicon or the incompatibility of the best known light emitting devices with silicon remain the main limiters of silicon photonic systems. Traditionally, semiconductor light emitters utilize direct band to band transitions of carriers which ultimately combine an electron-hole pair across the band gap to emit a photon of corresponding energy. Silicon's indirect band gap separates free electrons and holes in momentum space making radiative recombination unlikely. Since the radiative lifetime of Si is long (milliseconds) and the non-radiative lifetime is relatively short (nanoseconds), internal quantum efficiency of Si emitters is very low (about 10^{-6}), many orders of magnitude lower than the efficiency of typical direct band gap semiconductor devices such as those based on GaAs and InP. Fabrication of light emitters integrated on a Si wafer is possible through a variety of mechanisms and the approaches stem from a wide range of physical principles, from coaxing band-to-band emission from native Si, using nonlinear optical properties of Si,

introducing luminescent impurities to the Si lattice to or through hybridization of Si with other luminescent systems.

Perhaps the most promising approach to integrating laser sources on Si is through integration of III-V materials directly onto the Si wafer. Decades of telecommunication technology have provided advanced designs for InP-based III-V diode lasers which emit around 1.3 μm and 1.55 μm . Using photons near these colors makes sense for a Si OEIC; silicon's transparency at these wavelengths makes it a natural choice for the core material of waveguides and with its high refractive index contrast, Si/SiO₂ waveguides have excellent potential for a convenient and high performance waveguiding system. But this color choice also requires development of integrated photodetectors using new materials. Figure 1.4 shows absorption as a function of wavelength for a variety of common semiconductors and indicates that at the telecommunication wavelengths of 1.3 μm and 1.55 μm , Ge's reasonable absorption makes it an excellent material of choice for photodetectors but requires integration of yet another material (lattice constant) into the CMOS process.

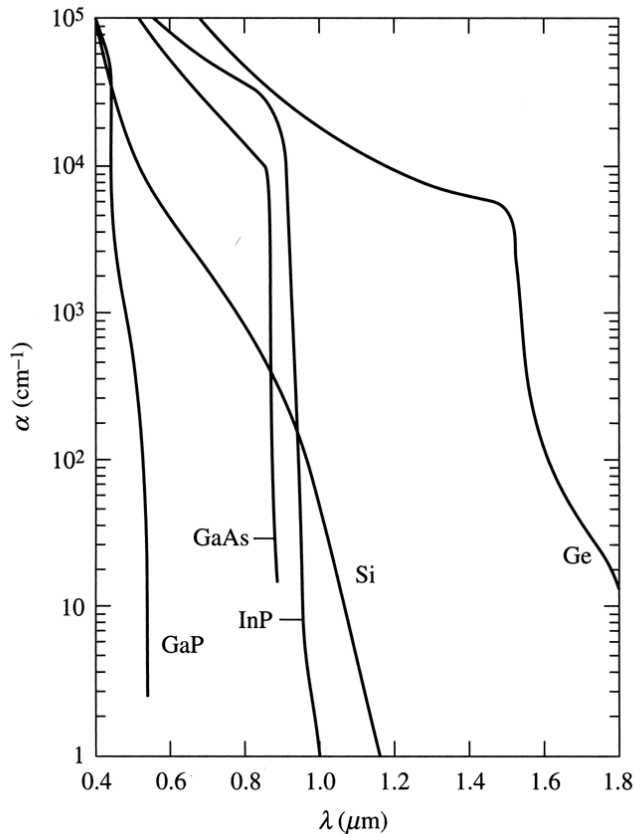


Figure 1.4 Absorption coefficient as a function of wavelength for a variety of semiconductors. Reproduced from Pierret⁵.

To reduce the burden of materials integration, we can look towards Si as the photodetector material. The key requirements of the photodetector are to convert optical to electrical signals efficiently, preferably with an explicitly designed method for coupling in light at low loss. This is typically done in semiconductors through generation of photocurrent: Photons impinge on a reverse biased p-i-n junction where the active material has a band gap lower than the photon energy. Excited carrier pairs are swept apart by the provided electric field and thus create an electrical current (signal). The speed at which the detector can operate is determined by the length of time it takes for carriers to reach the electrical contacts or by the capacitance of the device which creates

an RC time constant. Thick intrinsic regions allow sufficient length for efficient photon absorption (therefore high responsivity) and reduce device capacitance, but increase time of transit of carriers. Hence detector design must be optimized for tradeoffs in transit time, capacitance and responsivity.

Specifically, we envision an optoelectronic platform in which Si, the traditional, low-cost material for CMOS components is also used as the photodetector material and is integrated with III-V material that functions as the light emitter. In particular, yellow-green emission is of interest due to the convenient absorption length of wavelengths in this range in Si. As shown in Figure 1.4 in the 500-600nm range, the absorption coefficient of Si (α_{Si}) is close to 10^4 cm^{-1} . At shorter wavelengths, α_{Si} is larger, meaning that the active region of a Si *pin* photodetector must be quite thin, increasing device capacitance and slowing the performance of the device. Similarly, at longer wavelengths, α_{Si} decreases, making Si photodetectors inefficient; to work well at these wavelengths they would need to be thick and therefore would be also be quite slow (generated carrier extraction is slow) and cumbersome. The primary motivation of this thesis is demonstration of sources amenable to integration for this application.

Chilukuri et al.⁶ demonstrated monolithic integration of a well-known III/V device on a Si wafer while using CMOS compatible processing techniques. By developing photonic solutions for the yellow-green emitter and combining them with Chilukuri's integration technology, a ground-breaking OEIC can be demonstrated.

1.3 Organization of Thesis

This thesis is divided into two sections:

- *Motivation and review of methods used in the original research:* Chapter 2 gives “Materials Science” background, outlining the materials selection process, reviewing concepts in lattice mismatched epitaxy and introducing the basic physical properties of the materials studied. Chapter 3 provides “technology” background, giving information about the MOCVD and characterization systems used.
- *Original research:* Chapter 4 presents the results of investigation into virtual substrates designed to support the green light emitting heterostructures. Chapter 5 discusses the details of microstructural control of the (Al)InGaP heterostructures grown on virtual substrates. Chapter 6 presents the results of the light emitting device fabrication experiments. Finally, Chapter 7 concludes and offers suggestions for future directions of this work.

Chapter 2 Materials Design

2.1 Material Selection

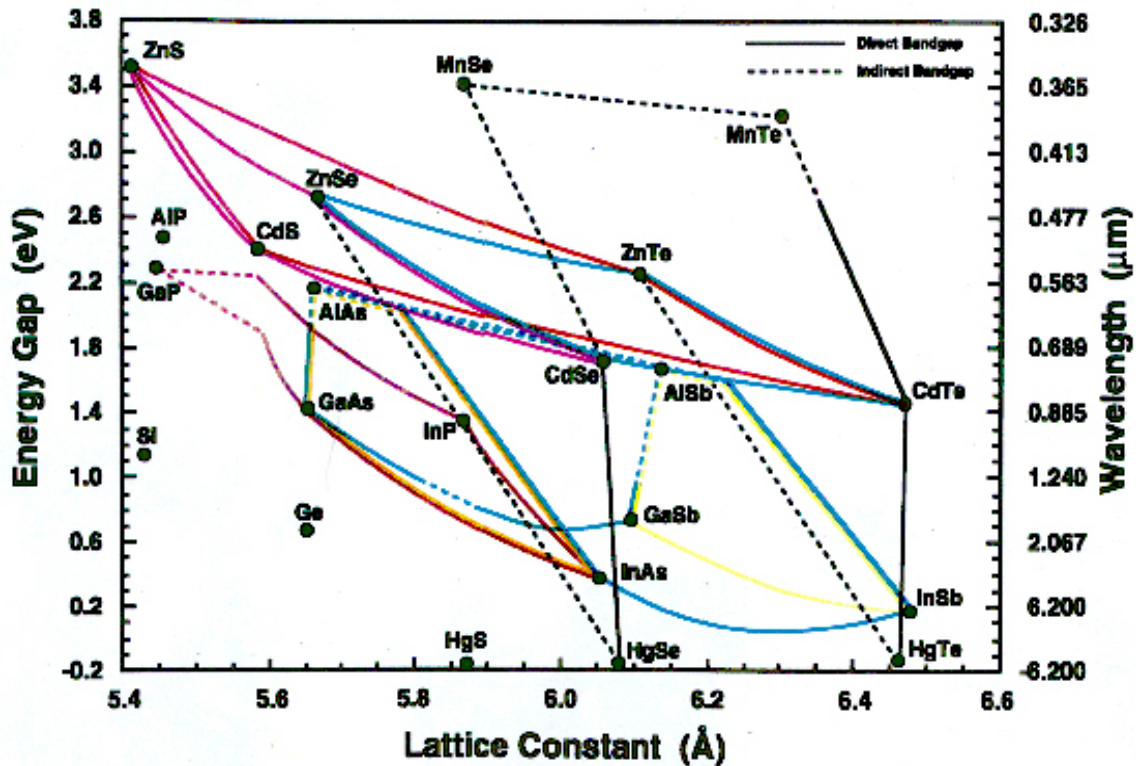


Figure 2.1 Band gap as a function of lattice parameter for many semiconducting materials. Ternary materials are represented by the lines connecting the binary materials data points. Figure adapted from poster by V.G. Keramidas and R.E. Nahory.

From the many available semiconductors, (see Figure 2.1), we set out to select a single materials system for improved green light emission. The target system must satisfy several basic requirements and we can identify several potential candidates:

III-V vs. Other Semiconductors

The III-V's provide an astounding range of electronic properties from relatively few constituent elements. Through compositional control of the III-V ternary and quaternary (or higher order) alloys we are able to choose a material's electronic structure with a high degree of freedom and excellent predictability. For example, the band gap of $\text{In}_x\text{Ga}_{1-x}\text{P}$ ($0 < x < 1$), a ternary alloy composed of GaP and InP, can be varied to any value

between those of GaP and InP through the control of the In fraction, x . By Vegard's law, the lattice constant of the alloy varies linearly with x . The band gap of the alloy is both theoretically and experimentally determined and usually well known for III-V materials.

Secondly, reliability of III-V semiconductor devices is demonstrated. II-VI semiconductors, although also flexible in terms of electronic design, have proven to be difficult in practical use due to their inherent softness and therefore susceptibility to material degradation over time.

Also of extreme importance is III-V's long history of commercial success. The compound semiconductor industry is founded around crystal growth and device processing technology separate from conventional CMOS microelectronics. Exploiting advanced growth techniques and reactor designs enables high quality growth of research materials. The many beneficial attributes of III-V compound semiconductors lead us to choose these over more exotic materials such as ZnO and other II-VI materials.

Band Gap

As mentioned previously, traditional light emitter designs require the use of a direct band gap material for radiative recombination of excited carriers across the band gap. The emitted color of the device can be engineered through selection of the band gap of the active material. For yellow to green designs we require band gap of at least 2.1-2.4eV. This immediately rules out many of the III-V materials shown in Figure 2.1. We immediately see that the AlInGaP and AlInGaN (not shown) quaternaries hold promise. In the case of AlInGaP, two of the three constituent compounds have indirect band gaps. Therefore to utilize AlInGaP we must understand how to design AlInGaP alloys with direct band gaps.

Lattice Constant

Perhaps the greatest restriction on the materials selection process is lattice constant. In most commercial applications, semiconductor alloys are limited to those at lattice constants close to that of available substrates (GaP, GaAs, InP, etc). Integration of materials with disparate lattice constant results in crystal defects (broken bonds) which behave unfavorably in electronic devices (as trap states, sources of leakage currents, etc.). By pseudomorphically straining material it is possible to deviate slightly from the substrate lattice, but low defect density, thick layers are not usually possible and not much freedom in alloy choice is yielded.

At very small lattice constant (4.52\AA for zincblende), GaN-based materials are particularly affected by lattice constant considerations as no low-cost, widely available substrate exists for compositions of InGaN with the appropriate “green” band gap or even GaN. Stretching the nitride materials systems toward green requires forcing as much In as possible into InGaN. This leads to strain and thermodynamic limitations on the system which lead to crystal defects at a detriment to device performance.

Similarly, AlInGaP is usually limited to the GaAs lattice constant. By increasing the fraction of Al in AlInGaP, lattice constant is kept essentially constant but band gap is increased. As the band gap moves toward energies for yellow green from red, the indirect character increases, causing carrier leakage to the indirect conduction band valley and therefore efficiency droop. Just as in the InGaN case, band gap can be tailored through control of In fraction (this time by decreasing it), but the same strain incorporation and defect limitations are encountered.

Thus we see that for exceptional improvement of green materials we must focus on eliminating the lattice constant constraint. A strong focus in the motivation of this thesis is the integration of the green material with Si; by comparing the phosphide and nitride systems we can see that the phosphides are much more amenable to monolithic integration on Si. The crystal structure of Si and the non-nitride III-Ns is zincblende ($a_{\text{Si}}=5.43102\text{\AA}$, $a_{\text{GaAs}}=5.65325$) while the equilibrium crystal structure of the GaN is Wurtzite (with $a=3.189\text{\AA}$ and $c=5.185\text{\AA}$)⁷. The incompatible lattice structures of GaN and Si make integration of the nitrides on $\langle 100 \rangle$ Si extremely difficult. The prospect of mismatched integration of GaAs-like lattice constants on Si is much more feasible.

Hence we finally see that the AlInGaP quaternary system is the material of choice for integration of wide band gap material on Si.

2.2 Lattice Mismatched Epitaxy

As alluded to above, successful operation of electrical and optical semiconductor devices requires low-defect density, single crystals. While the method of Czochralski growth has made possible production of very large, very perfect crystals at low-cost, it is limited to relatively simple crystal structures, such as elemental or binary compound semiconductors such as Si or GaAs. Unfortunately, growth of other very useful ternary or higher order compounds of similar quality is made very complex by effects such as solute segregation in the melt, and only elemental and binary compound semiconductors are widely available in bulk wafer form.

Integrating different semiconductors is a difficult task, again limited by the necessity for highly perfect crystals. The semiconductor industry has, for the most part,

been limited to building devices of materials of the same lattice parameter, to avoid crystal defects. Our research group specializes in fabrication of high quality crystals with lattice parameters very different from those of the conventional semiconductor substrates. Here we review a compositionally graded design which relaxes the lattice-matched requirement under controlled conditions therefore allowing integration of Si and AlInGaP with lattice constant far from that of Si all while maintaining high quality material. Table 2.1 shows the lattice parameters of some semiconductor materials of interest.

Table 2.1 Lattice constants of some semiconductors of interest.

	a (Å)
InP	5.86964 ⁷
GaP	5.45044 ⁷
AlP	5.46714 ⁷
GaAs	5.65317 ⁷
Si	5.43102 ⁸
Ge	5.6579 ⁸

Lattice mismatch is defined as:

$$f = \frac{a_s - a_f}{a_f},$$

where a_s is the lattice parameter of the substrate and a_f is the lattice parameter of the film. Mismatch can be accommodated in two ways, through elastic and plastic deformation of the thin film:

$$f = \varepsilon + \delta,$$

Where ε is elastic strain in the film and δ is the strain relaxed through dislocation nucleation. Introduction of these dislocations in epitaxial growth of mismatched materials

is schematically indicated in Figure 2.2. If the mismatch is relatively small ($f \sim 2\%$), then as the first layers of a mismatched film are deposited, the atoms of the film arrange themselves in a low energy configuration, with bonds strained such that the in-plane lattice parameter of the film matches that of the substrate. As subsequent layers are added, the total amount of energy stored by the strained bonds becomes large very quickly. Although there is an energy cost associated with a line defect, their introduction relieves strain and can reduce the total free energy of the crystal. This process is the formation of a misfit dislocation. Through an analysis that minimizes the sum of strain energy and defect energy, we can postulate at what film thickness defects form. This is the classical formulation of the Matthews-Blakeslee critical thickness, h_c . More complete descriptions are available in the references section^{3, 9-12}. In practice, a deposited film will typically remain fully strained beyond the critical thickness since there are kinetic barriers to breaking bonds and moving defects.

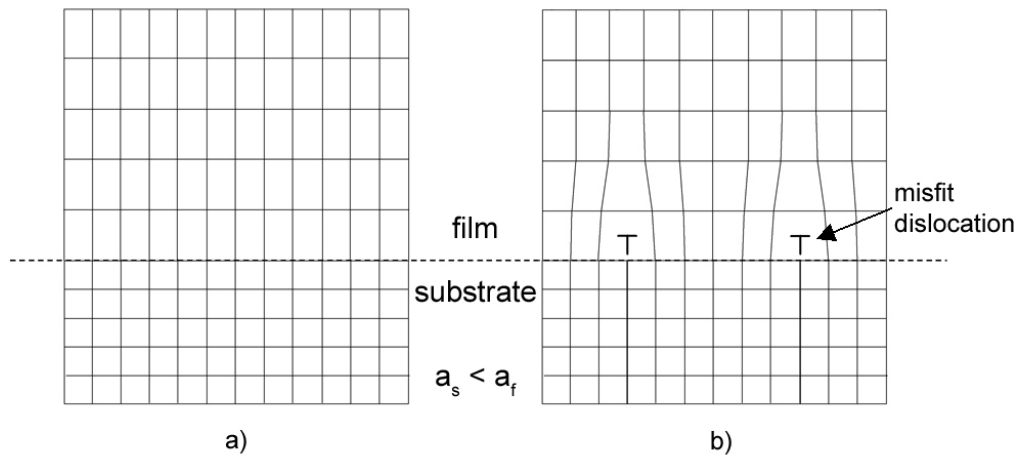


Figure 2.2 A schematic representation of mismatched epitaxy. On the left is sub-critical thickness film that is therefore coherently strained. The right drawing represents the relaxation that occurs in films thicker than h_c . Figure reproduced from McGill³.

Working with Dislocations

It is immediately obvious from the above discussion that in order to successfully engineer mismatched systems, incorporation of dislocations (to obtain plastic relaxation, δ) must be done in a controlled fashion. Extensive references for dislocation theory exist¹²⁻¹⁶ and will not be fully covered here. Instead we briefly review several details of dislocations in the zincblende system and conclude with design goals which, if satisfied, advantageously configure dislocations in a successful mismatched platform.

Our group seeks to release the lattice-match requirement by using misfit dislocations in a controlled manner to effectively relieve mismatch strain. Since dislocations can only terminate on themselves or at the surface of a crystal, portions of the misfit dislocation do not lie entirely at the film substrate interface. These parts of the misfit dislocations, called threading dislocations, intersect the surface and active portion of the device being grown, as shown in Figure 2.3. Since dislocations act as efficient recombination centers, they prevent radiative emission in light emitting devices and must be avoided.

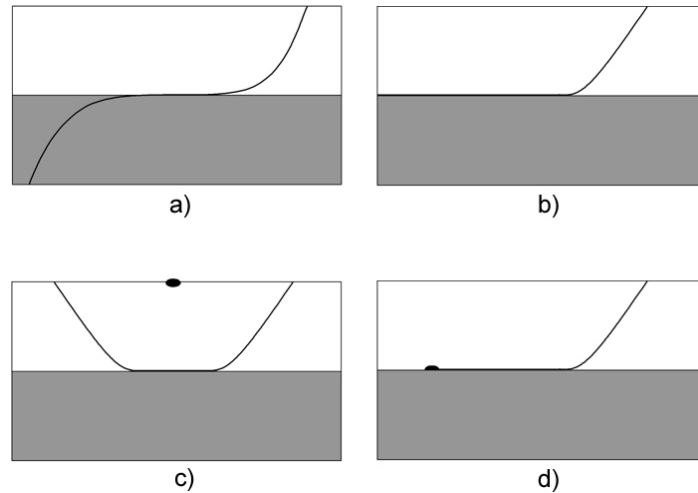


Figure 2.3 Several configurations of dislocations upon nucleation in a mismatched film. Note that the dislocation can only terminate at the crystal edge or on a heterogeneous defect. Portions of dislocations incline to the surface and are called threading dislocations. Image courtesy of McGill³.

Although a finite threading dislocation density (ρ_{TD}) is to be tolerated, it must be minimized. High quality GaAs substrates have typical ρ_{TDS} of 5000cm^{-2} or less. After heteroepitaxial growth, this density is usually higher; our goal is to prevent any device material from exceeding 10^6cm^{-2} , which we predict should be sufficient for the successful fabrication of optical devices. Without careful measures, a mismatch strain of 2.5% can result in TDD of over $5 \times 10^9\text{cm}^{-2}$.

In mismatched epitaxy, dislocations are formed by nucleation and propagation of preexisting threading dislocations in the substrate. Nucleation of dislocations most easily occurs heterogeneously at the surface or on particles or other defects. In zincblende systems, glissile dislocations have Burgers vector of $a/2\langle 110 \rangle$ and glide on $\{111\}$ planes (see Figure 2.4). Since only edge dislocations relieve strain (as opposed to screw dislocations which do not relieve strain), only a subset of all possible dislocations of this type can actively relieve mismatch on the (001). These dislocations are referred to as 60° dislocations due to the angle between their line direction and Burgers vector.

Additionally for zincblende, 60° dislocations can be divided into two types, α or β , based on the type of atom at the dislocation core (III or V). Since α and β dislocations can have very different glide velocities¹⁷ this can account for strain relaxation anisotropies in mismatched films.

Plastic strain, δ , is accommodated by misfits¹⁸:

$$\delta = \frac{\rho_{misfit} b_{edge}}{2}$$

where ρ_{misfit} is the linear misfit dislocation density and b_{edge} is the magnitude of strain relief which the edge dislocation provides (the component of the Burgers vector which relieves strain). Since the threading dislocation density of the substrate is typically not large enough to generate the required misfit length (plastic relaxation) to accommodate the several percent of mismatch we are interested in, additional dislocation segments must be nucleated¹². For an interfacial misfit segment that terminates with two threading dislocations at the surface, we can easily see that threading dislocation density, ρ_{TD} , is related to mean misfit dislocation length, L , and the linear misfit dislocation density, ρ_{misfit} :

$$\rho_{TD} = \frac{2\rho_{misfit}}{L}$$

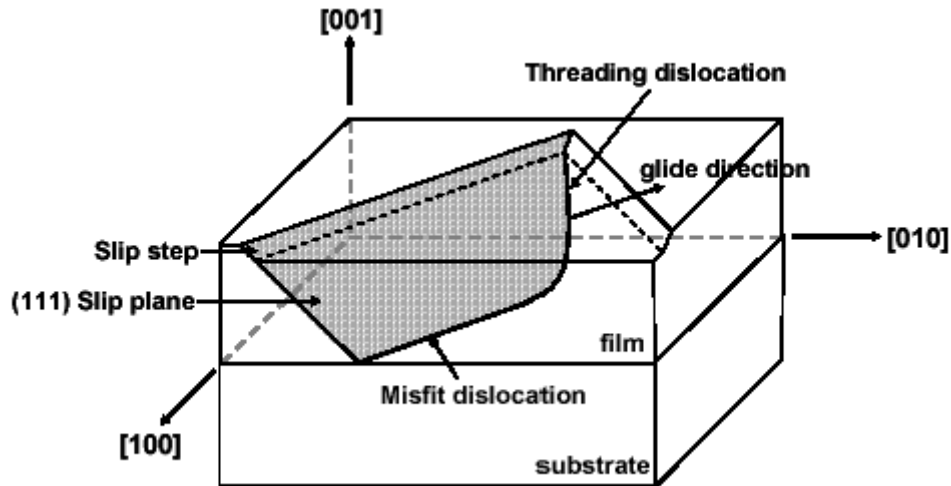


Figure 2.4 Schematic of a misfit dislocation gliding through a mismatched film. Portions that extend through the surface of the film, threading dislocation, are deleterious to device performance. Figure reproduced from Pitera¹⁹.

It is apparent that the mean misfit dislocation length, L , must be maximized for optimal films. To do this, the plastic strain rate in a growing film must be fast enough to maintain low elastic strain and thus enable relaxation by dislocation glide²⁰. Dislocation glide velocity (which determines L) is kinetically limited by the activation energy for dislocation glide, hence high temperature growth conditions are desirable. Also, a buildup of elastic strain leads to dislocation multiplication for which the activation energy is inversely proportional to the elastic strain. Lastly, ρ_{misfit} must be optimized: If it is too large, relaxation is suppressed and elastic strain builds up. Dislocations have associated strain fields and interact forcefully with one another as well as with other defects in the crystal, so if ρ_{misfit} is too small, dislocation-dislocation interactions serve to arrest movement, promoting elastic strain buildup and dislocation multiplication. Surface roughness is yet another consideration for dislocation interactions. Coherent surface roughening occurs in highly strained films and can impede dislocation motion or nucleate

additional dislocations. Figure 2.5 summarizes several possible dislocation interactions. We wish to minimize the likelihood that dislocation motion be impeded, so we must suppress dislocation populations and therefore maximize dislocation spacing under reasonable film thickness constraints.

To summarize, our objective is to promote free movement of 60° dislocations during growth, thus facilitating the formation of misfit dislocations and strain relief. To do this, we maintain the following design rules: Maximize dislocation glide velocity and minimize elastic strain since both promote a long mean misfit length. Minimize surface roughness and particle populations to prevent heterogeneous nucleation and dislocation pinning. Optimize dislocation spacing to prevent interactions and prevent “pile-ups.” These goals can be achieved through choice of crystal system, sense of strain relaxation (tensile or compressive), control of reactor environment and control of growth parameters such as V/III ratio and temperature. These observations lead us to the design of the compositionally graded buffer for high quality metamorphic layers which we will discuss next.

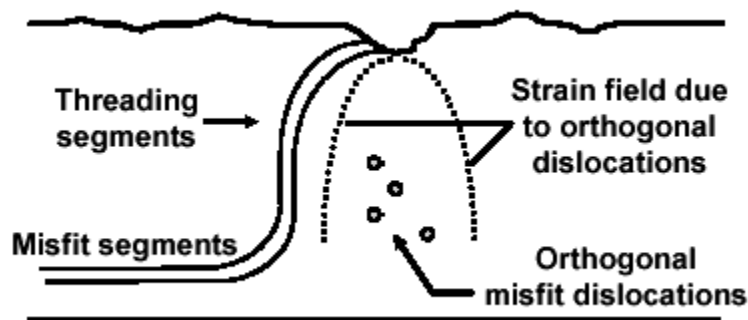


Figure 2.5 Dislocations interact forcefully with features in the crystal. To avoid high threading dislocation densities, we wish to minimize interactions that might prevent effective dislocation glide and crystal relaxation. Figure reproduced from Pitera¹⁹.

Compositional Grading

Early efforts at integrating lattice mismatched materials focused on a “two-step” growth method where a thin, two-dimensional but highly mismatched layer was grown at low temperature and annealed, with a subsequent thick layer on top grown at higher temperature to improve crystal quality. These methods have limited success and achieve device layers with a ρ_{TD} on the order of 10^8cm^{-2} ²¹⁻²³. The thick buffers they require are time-consuming to grow and therefore increase the cost of production. InGaP in particular is a difficult material to work with, as surface morphology has been reported to deteriorate with relatively small misfit values, greater than 0.1%²⁴. Lastly we note that the two-step initiation does not follow the design rules we derived from dislocation theory.

Alternatively, compositional grading can be used to spread mismatched layers across a distance during the crystal growth process. By slowly varying the lattice parameter in a crystal, we introduce misfit dislocations gradually, keeping dislocation spacing large. Our group has historically had great success in the growth of SiGe, InGaP and InGaAs graded buffers²⁵⁻²⁷. These growths consist of homoepitaxy followed by growth of layers with slowly increasing content of Ge or In. This is shown in Figure 2.6 for $\text{GaAs}_{1-x}\text{P}_x$ and Figure 2.7 for InGaP. Or, the growth is terminated with a uniform composition layer with x at any value less than one. Graded buffers have enabled several major accomplishments recently, including a record high τ_p of 7.7ns in GaAs on graded SiGe²⁸, epitaxial transparent substrate InGaP LEDs^{29, 30} and AlGaAs lasers on graded SiGe³¹.

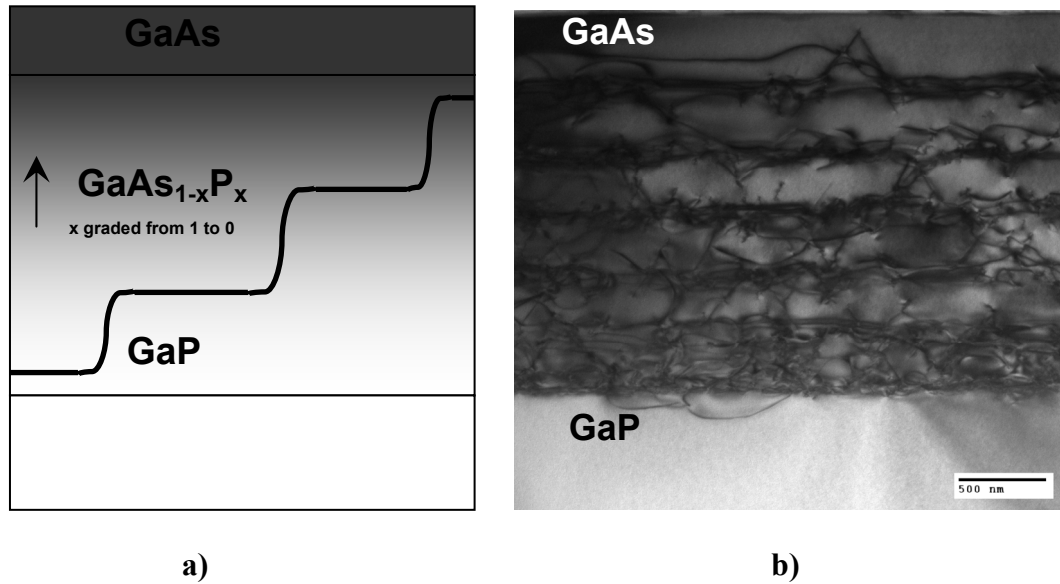


Figure 2.6 a) Schematic and b) XTEM of the metamorphic graded buffer where GaP is graded to GaAs. Note that only a single dislocation is shown but that in reality many dislocation recycle threads to relax strain at many interfaces thus maximizing misfit length for threading length.

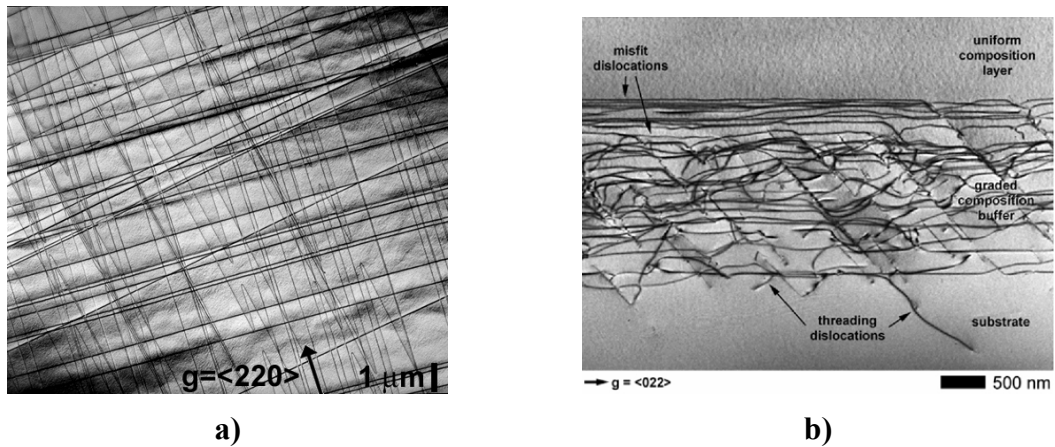


Figure 2.7 a) PVTEM and b) XTEM of an InGaP graded buffer misfit dislocation array. Images from³.

The optimized relaxed graded buffer has been used in a large number of different systems and has a rich history associated³²⁻³⁴. Abrahams³⁵ and Fitzgerald²⁵ presented a kinetic glide model in which threading dislocation density is independent of absolute strain incorporation and decreases exponentially with temperature. This model has more recently been confirmed by Leitz³⁵.

2.3 Properties of AlInGaP and GaAsP

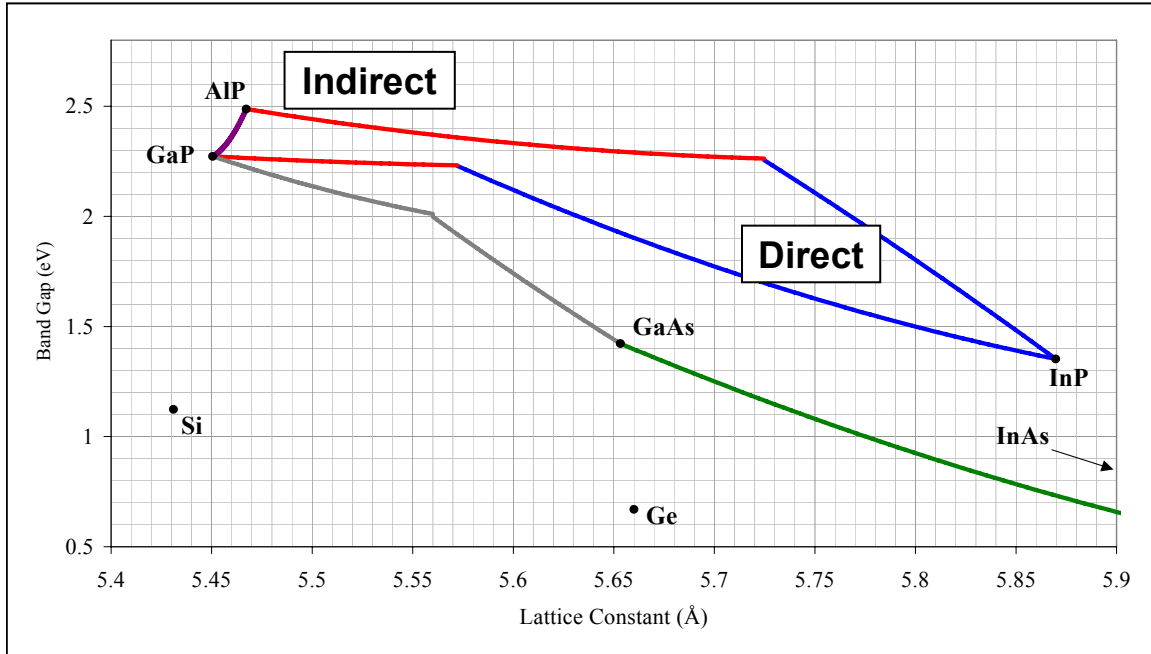


Figure 2.8 Band gap as a function of lattice parameter for the AlInGaP quaternary system. Data obtained from Vurgaftman⁷.

In discussions above we have already justified the choice of AlInGaP for green light emission. We also have chosen GaAsP as the “mechanical” material for building virtual substrate for the AlInGaP “optical” material. Here we discuss some of the properties of both materials and some of the aspects of microstructural control that will be required for successful device fabrication.

Aluminum indium gallium phosphide (AlInGaP) is a quaternary III-V compound semiconductor comprised of arbitrary fractions of the three binary constituent components GaP, AlP and InP. Similarly, gallium arsenide phosphide (GaAsP) is a ternary III-V compound made up of GaP and GaAs. By adjusting the compositional ratios of In, Ga and Al in AlInGaP or As and P in GaAsP, the physical properties of the materials can be adjusted widely. For example band gap ranges from 1.35eV (InP) to 2.49eV (AIP) in AlInGaP and the lattice constant of GaAsP varies from 5.4505Å (GaP)

to 5.65325 Å (GaAs). The entire compositional range of both compounds is accessible and both are of the zincblende crystal structure. This is like a diamond cubic structure with a two-atom basis, or two interpenetrating FCC lattices. Each III atom in the lattice is tetrahedrally coordinated and covalently bonded with four V atoms and vice versa.

Of extreme importance to this project is a perhaps at first superficial difference between the two compounds: AlInGaP is a mixed cation compound whereas GaAsP features mixed anion composition. This distinction does not affect the crystal structure of the materials and in fact the two lattices are inherently compatible. More important to the experimenter is the difference in the chemical behavior of the compounds which has profound effects on their fabrication via MOCVD growth. More will be discussed in a following section on MOCVD growth.

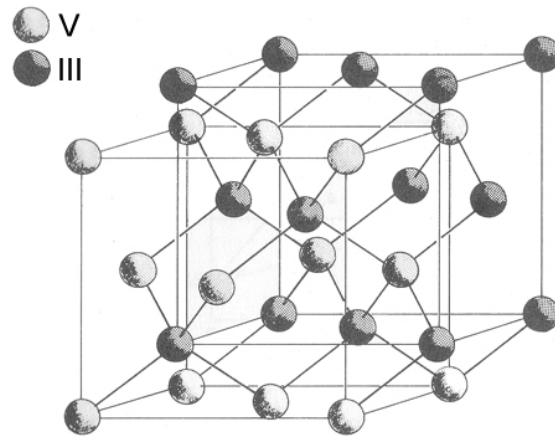


Figure 2.9 The zincblende crystal structure consists of two interpenetrating FCC lattices. Reproduced from Stringfellow³⁶.

In this document, the following conventions will be used to define the composition of both compounds. For GaAsP we use a single number, the phosphorus fraction z in $\text{GaAs}_{1-z}\text{P}_z$, to define the alloy composition. Note that z is always in the range of 0 to 1.

For the extra compositional degree of freedom in AlInGaP it is simplest to use two independent numbers to define the composition of AlInGaP. Since the lattice constants of AlP and GaP are quite close it is convenient to disregard the contribution of Al:Ga ratio to the lattice constant and consider only the contribution of In fraction instead. Hence we define AlInGaP composition in terms of a percentage of Al in total Al and Ga (y) and In fraction (x): $\text{In}_x(\text{Al}_y\text{Ga}_{1-y})_{1-x}\text{P}$. Although this formulation can be misleading (for example if x is large then the value of y carries very little significance), but for the compositions used in this project, using these definitions of x and y enhances clarity.

In order to build optoelectronic devices from exotic materials we must first make predictions about electronic properties of the materials by looking towards other studies of III-V properties. An excellent literature review of the properties of most III-V materials is provided by Vurgaftman⁷. Most of the materials properties predicted for AlInGaP in this paper come from the recommendations of these authors. Here we will discuss briefly the values used for lattice constant and band structure. A Mathematica script containing all values used is included in the appendix.

The lattice constant of mixed materials can be approximated through linear interpolation of its constituent components. This is Vegard's Law. For example, the lattice constant of any composition of $\text{In}_x\text{Ga}_{1-x}\text{P}$ is:

$$a_{\text{InGaP}} = (1 - x)a_{\text{GaP}} + xa_{\text{InP}} \quad \text{Equation 2.1}$$

Where a_i is the lattice constant of component i . The temperature dependent binary lattice constants used in this project are outlined in Table 2.2.

Table 2.2 Lattice constant as a function of temperature for several III-V binary compounds. Data based on recommendations by Vurgaftman⁷.

Binary Constituent	Lattice Constant (in Å, with T in K)
GaP	$5.4505 + 2.92 \times 10^{-5} (T-300)$
InP	$5.8697 + 2.79 \times 10^{-5} (T-300)$
AlP	$5.4672 + 2.92 \times 10^{-5} (T-300)$
GaAs	$5.65325 + 3.88 \times 10^{-5} (T-300)$

By adding a quadratically dependent bowing constant, this formulation is extended to describe ternary band gap parameters. For example the Γ conduction band position (direct) for $\text{In}_x\text{Ga}_{1-x}\text{P}$ is:

$$E_{\text{InGaP}}^{\Gamma} = (1-x)E_{\text{GaP}}^{\Gamma} + xE_{\text{InP}}^{\Gamma} + x(1-x)C \quad \text{Equation 2.2}$$

where C is the band bowing parameter for the InGaP Γ band. Table 2.3 lists parameters which describe the behavior of the Γ and X bands for InGaP and InAlP.

Table 2.3 Γ and X band bowing parameters for several III-V ternary compounds. Data based on recommendations by Vurgaftman⁷.

Ternary Compound	Band Bowing Parameter (eV)
InGaP, Γ	0.65
InGaP, X	0.2
InAlP, Γ	-0.48
InAlP, X	0.38
AlGaP, X	0.3

The band gaps of the binary compounds are temperature dependent and have been empirically observed to follow the Varshni form³⁷:

$$E_g(T) = E_g(T=0) - \frac{\alpha T^2}{T + \beta} \quad \text{Equation 2.3}$$

where α and β are the adjustable Varshni parameters. Relevant Varshni parameters are shown in Table 2.4. Note that the GaP Γ and InP X bands are described by a different temperature dependency than the Varshni formulation.

Table 2.4 Compilation of Varshni parameters for the temperature dependence of the Γ and X bands of GaP, InP and AlP. Data based on recommendations by Vurgaftman⁷.

Binary Compound	$E_g(T=0)$ (eV)	α (meV/K)	β (K)
GaP, Γ	2.886	-0.1081[1-coth(164/T)]	n/a
GaP, X	2.35	0.5771	372
InP, Γ	1.4236	0.363	162
InP, X	2.384	$-3.7 \times 10^{-4}T$	n/a
AlP, Γ	3.63	0.5771	372
AlP, X	2.52	0.318	588

Thus far we have given data to describe properties of the binary and ternary compounds used in this study. It is also useful to linearly interpolate these properties for quaternary systems. Glisson et al.³⁸ and Williams et al.³⁹ give a simple method for quaternary interpolation using general formulae for the ternary compounds. In the general case of a quaternary compound of the form $AB_mC_nD_o$ (with $0 \leq (m, n, o) \leq 1$ and $m + n + o = 1$) the quaternary interpolation of a property, Q is given by:

$$Q(m, n, o) = \frac{mnT_{BC}(u) + noT_{CD}(v) + moT_{BD}(w)}{mn + no + mo} \quad \text{Equation 2.4}$$

where T_{ij} is the calculated ternary property of the A_{ij} compound,

$$u = \frac{1 - m + n}{2}, \quad \text{Equation 2.5}$$

$$v = \frac{1 - n + o}{2}, \quad \text{Equation 2.6}$$

and

$$w = \frac{1 - m + o}{2} \quad \text{Equation 2.7}$$

Applying the formulation to AlInGaP and using our previously described composition parameters x and y, we have:

$$Q(x, y) = \frac{x(1-x)(1-y)T_{InGaP}(f) + y(x-1)^2(1-y)T_{GaAlP}(g) + xy(1-x)T_{InAlP}(h)}{(1-x)(x-xy+xy^2+y-y^2)} \quad \text{Equation 2.8}$$

where

$$f = \frac{1-x+y}{2}, \quad \text{Equation 2.9}$$

$$g = \frac{2-x-2y}{2}, \quad \text{Equation 2.10}$$

$$h = \frac{2-2x-y}{2}, \quad \text{Equation 2.11}$$

and in this case T is the interpolated property of the ternary compound defined by:

$$T_{ijP}(q) = qF^{jP} + (1-q)F^{iP} - q(1-q)C^{ijP} \quad \text{Equation 2.12}$$

with F^{iP} representing the value of the property of the binary constituent and C^{iP}

representing the relevant bowing parameter. Note that the order of the species listed for the ternary interpolation is significant and that Q is indeterminate if x or y are zero (and the compound is no longer a quaternary).

Now that we can easily calculate predicted values for lattice parameter and conduction band edges for all compositions of AlInGaP we can plot these values to create a visualization tool for optoelectronic device design. At thermal equilibrium, carriers relax to the lowest energy state available to them, hence electrons in the conduction band are distributed to the lowest of the Γ , X or L bands. The populated conduction band has strong implication on the optical nature of the material, thus when we wish to plot the band gap as a function of composition, we choose to show the minimum conduction band and denote the material as indirect (X is the minimal) or direct (Γ is minimal). Note that for nearly all compositions of AlInGaP, the L band is predicted to be much higher in energy than the Γ and X bands. Figure 2.10 shows the resultant plot. Band gap is plotted as a function of lattice constant for all GaAsP and AlInGaP materials.

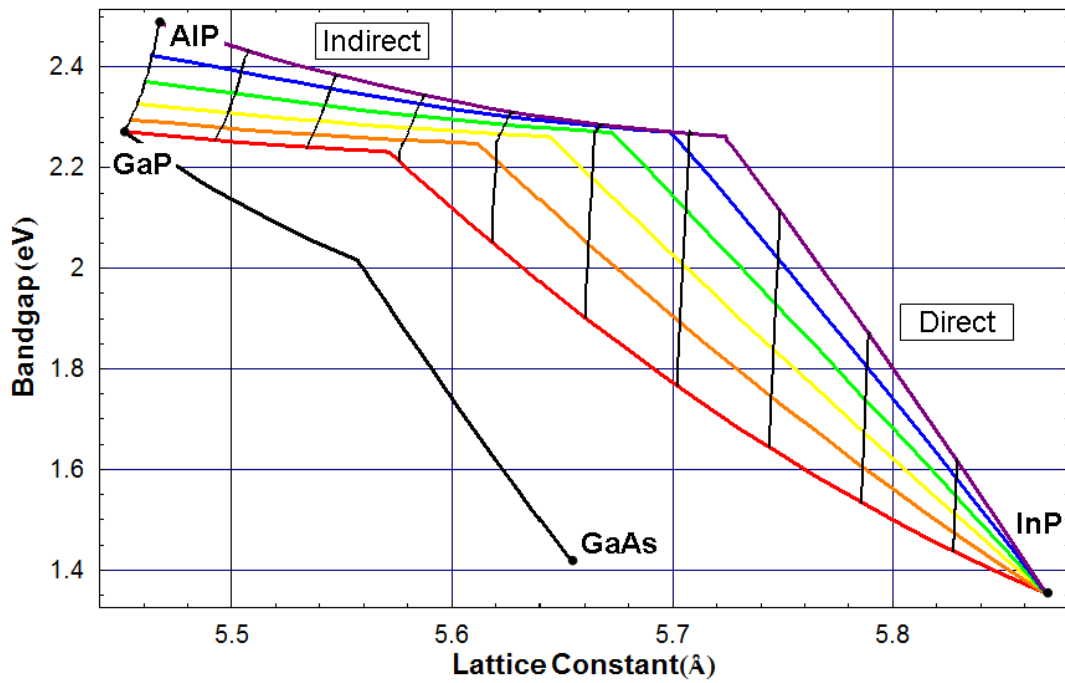


Figure 2.10 Calculated minimum band gap as a function of lattice constant for the quaternary AlInGaP system. Constant In-composition lines are shown in increments of 10% and constant Al-composition lines are in increments of 20%.

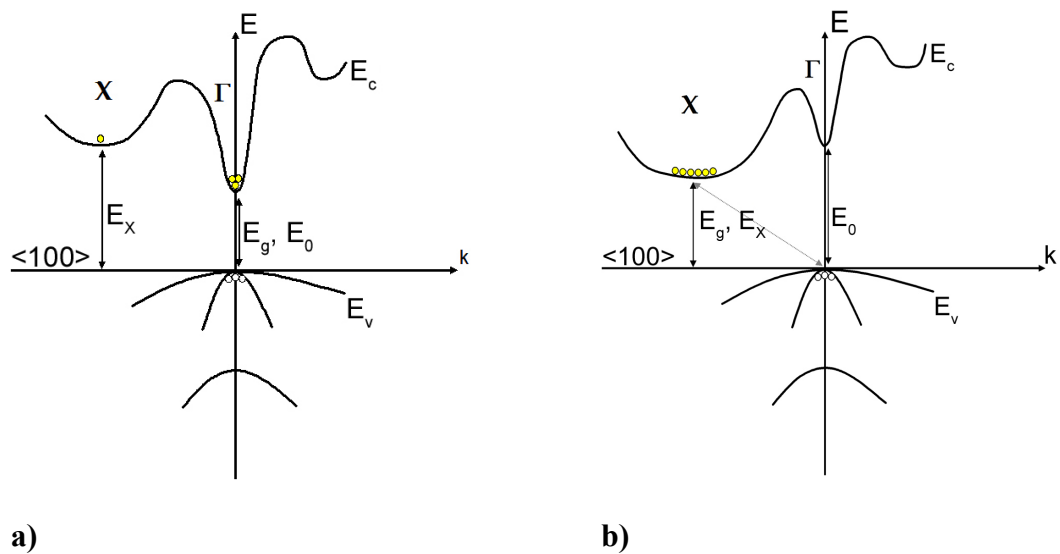


Figure 2.11 Energy vs. momentum schematic for a) direct ($E_g = E_0$) and b) indirect ($E_g \neq E_0$) semiconductors. When the indirect (X) band minimum is near or lower than direct (Γ) minimum, fewer carriers will be able to recombine radiatively. Reproduced from McGill³.

The schematic in Figure 2.11 illustrates the necessity of using a direct band gap material for the active region of a light emitter. Excited electrons in the Γ conduction band valley radiatively recombine with excited holes in the valence band valleys with no momentum change ($\Delta k=0$). For such a transition to occur from the X conduction band valley, a momentum change for electrons is needed. This Δk can be supplied with a phonon interaction, but since this is quite unlikely, other non-radiative recombination pathways predominate and emission is effectively prevented. Due to the high density of states of the indirect valley, even as the X and Γ valleys become close (the alloy composition is close to the indirect-direct crossover), excited carriers are distributed to the X valley. This effectively lowers in the internal quantum efficiency of a device.

2.4 Device Design

For the realization of yellow-green emitters, we are concerned with designing a device active region with as large of direct band gap as possible. We first select the active layer composition, and then select the virtual substrate to support it.

Device Active Layer

As the In:Ga ratio in (Al)InGaP increases, the material transitions from indirect to direct. Unfortunately there is not much agreement in the literature regarding the exact compositions of the direct-indirect crossover in AlInGaP, except for that which is lattice matched to GaAs. As described above, as the conduction band gains indirect character internal quantum efficiency is expected to drop. This effect might be counteracted by using nitrogen as an isoelectronic dopant⁴⁰. Incorporation of N as a point defect delocalized states in momentum space and enhances radiative recombination from the X minimum to the valence band maximum. Future study of N-doping in InGaP may

improve internal quantum efficiencies. Also, the use of a quantum well design is expected to increase recombination efficiency and counteract the closeness to the indirect-direct crossover. We intend our device designs to test the lower limit of In content in order to increase the device band gap as much as possible.

The largest direct band gap InGaP is near $\text{In}_{0.3}\text{Ga}_{0.7}\text{P}$ at a lattice constant of about 5.57\AA with a band gap of about 2.21eV . Photons of this energy have a wavelength of 560nm . This material will be the basis of our active layer.

Virtual Substrate

Given our choice of active material, we must focus on a virtual substrate with a lattice parameter around 5.57\AA , but the exact composition will depend on the device design. We have made a computer model to help us predict the electronic parameters of AlInGaP devices, and we will discuss this below.

A lattice parameter of 5.57\AA represents a strain of about -2.5% with respect to the lattice constant of Si, thus we must engineer a high quality virtual substrate for our device studies. Previous work by Kim^{12,29} and McGill^{3,41} focused on InGaP graded buffers on GaP to achieve substrates with lattice parameters intermediate to GaP and GaAs. Their work was successful in optimizing buffers to 5.57\AA and resulted in TDDs on the order of $2 \times 10^6\text{cm}^{-2}$ to $7 \times 10^6\text{cm}^{-2}$. One major conclusion of the work was that segregation of the group III material led to defects that escalated TDD. In efforts to avoid this, we have implemented a different grading scheme wherein we grade group V content instead of group III.

Our system of choice is GaAsP and the composition of interest at 5.57\AA is $\text{GaAs}_{0.62}\text{P}_{0.38}$. To minimize total mismatch incorporation and 5.57\AA is closer to GaAs than

GaP, our initial efforts have focused on starting the grade from GaAs. This requires a tensile grade rather than the compressive grade that our group expertise lies in (such as InGaP on GaP, InGaAs on GaAs or SiGe on Si). We note that the physics of a tensile grade are very different than the physics of a compressive grade. This aspect of the project alone is an avenue for rich study. Besides avoiding group III segregation, an additional advantage of turning to a GaAsP on GaAs grade is that the absolute value of total strain which must ultimately be incorporated is much less than in the InGaP on GaP case (1.44% versus -2.15%).

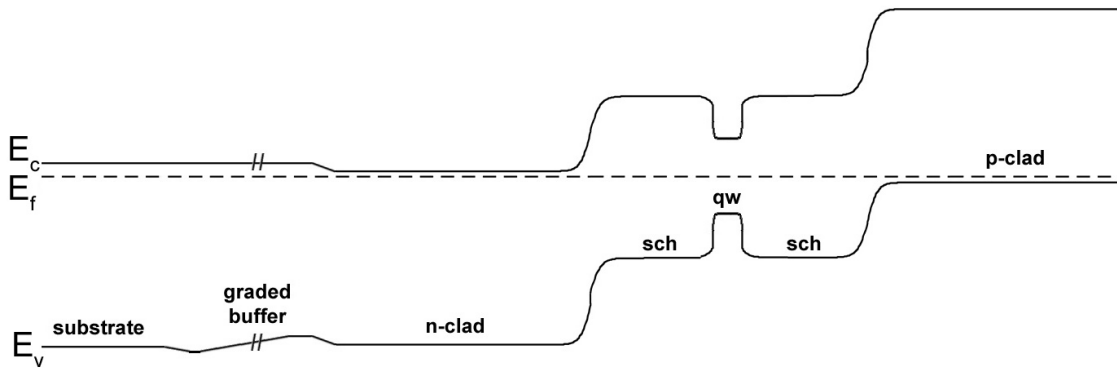


Figure 2.12 Schematic of band structure for an entire device integrated on a transparent virtual substrate (adapted from McGill³).

2.5 Engineering the Band Structure

Due to the fact that the active material of our device design is close to the indirect-direct crossover, we expect to find significant carrier leakage. We hope to minimize this through the use of a strained quantum well (SQW) design that provides good electrical confinement, such as that shown in Figure 2.12. We must design the active region of the device to provide the desired band structure. To supply the confinement, we must use a material with a wider band gap and type I offset with respect to the QW. (Figure 2.13 reviews the three possible types of band alignment.) By adding Al or removing In from

the barrier material, we increase the band gap. Since all radiative recombination must happen in the QW, it is not a concern that this material is indirect. In order to fully understand the implications behind selecting a design we must be able to predict the electronic structure and alignment of the AlInGaP band structure as much as possible. Unfortunately there is even less agreement in the literature regarding band offsets in AlInGaP than there is regarding band gaps. We have based our model on recommended band parameters⁷.

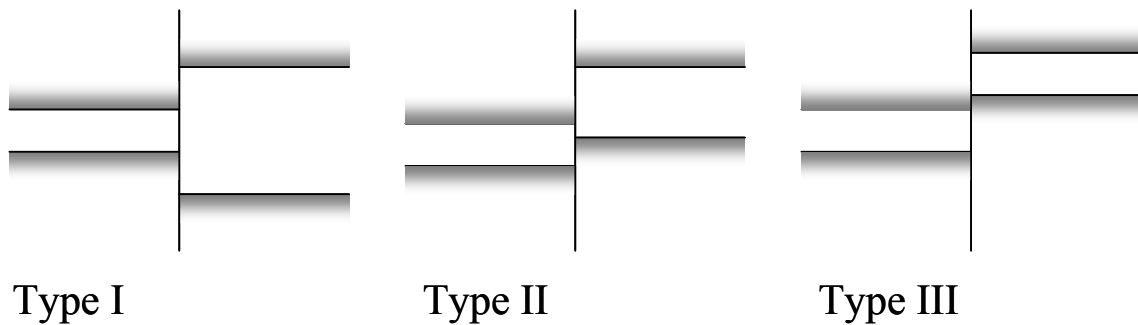


Figure 2.13 The three possible type of band alignment at a heterojunction. For the SQW structure, we desire type I alignment.

Using the normalized infinite quantum well approximation for confined levels⁴² we have modeled the emission wavelength and confinement available for various compositions of barrier and quantum well with quantum well thickness as a parameter. Mathematica code used for this simulation is included in Appendix B. We immediately find that, as predicted, our device design will be limited at short wavelengths by the available confinement. An example calculation result is shown in Figure 2.14. More details of the results of the model will be discussed in Chapter 6.

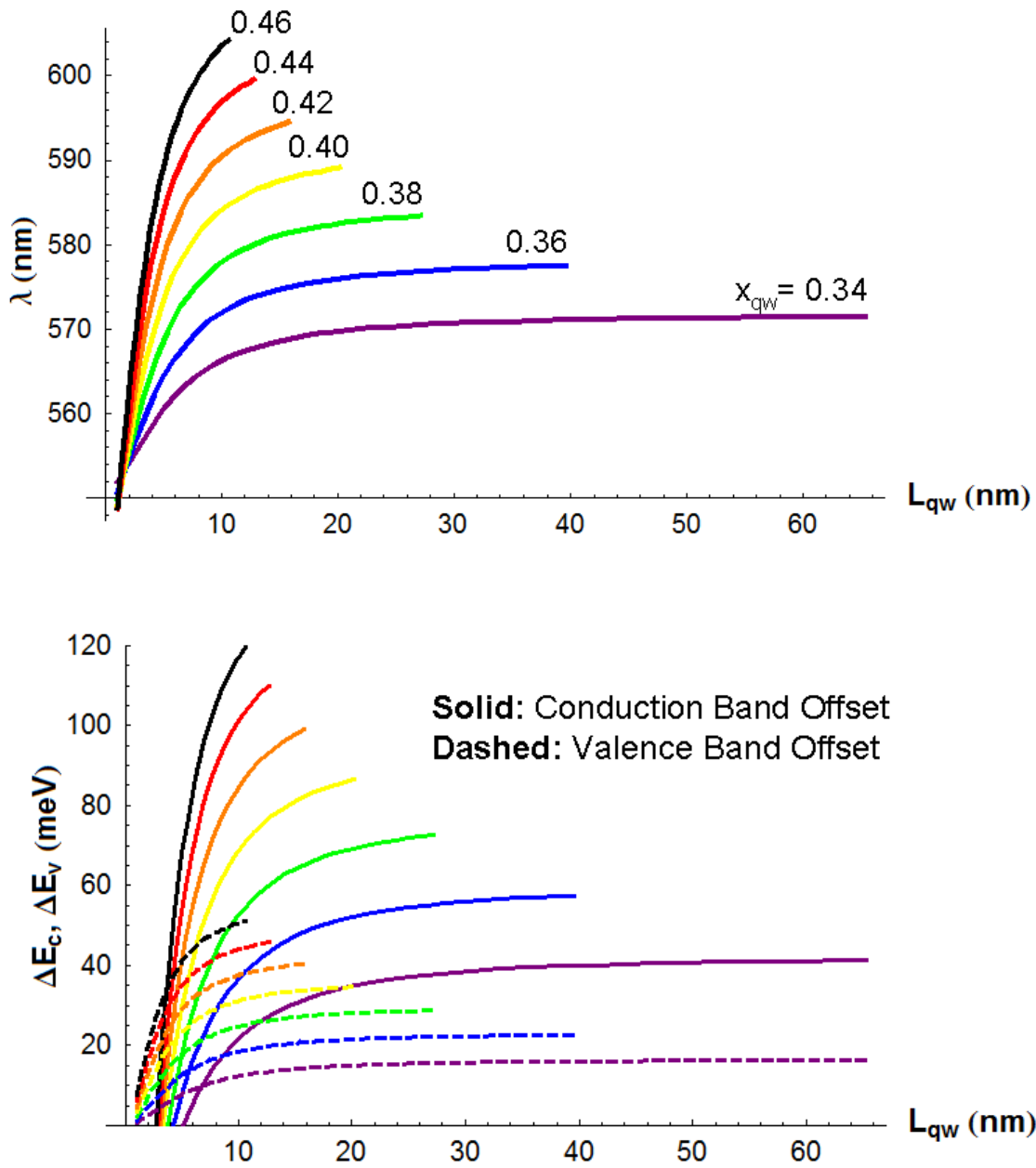


Figure 2.14 Some example results of the computer model. Here we have specified that the cladding material, $\text{In}_{.29}\text{Ga}_{.71}\text{P}$, is lattice matched to the substrate and that the thickness and composition of the $\text{In}_x\text{Ga}_{1-x}\text{P}$ QW is varied.

Chapter 3 MOCVD Growth and Characterization

3.1 Introduction

The work in this thesis focuses on the synthesis and characterization of new alloys of III-V semiconductors for visible light emitting applications. The crystal growth method used exclusively in this study is metalorganic chemical vapor deposition (MOCVD), also commonly known as organometallic chemical vapor deposition (OMCVD), organometallic vapor phase epitaxy (OMVPE) and metalorganic vapor phase epitaxy (MOVPE). MOCVD is to be distinguished from other growth techniques such as hydride vapor phase epitaxy (HVPE) or liquid phase epitaxy (LPE) which use other categories of precursors, reaction mechanisms and reactor geometries. MOCVD is commonly held as the most technologically advanced of the crystal growth methods and is the preferred technique in commercial production of III-V semiconductor devices. Extremely high purity precursors are readily available for deposition of a very large array of materials under many conditions.

The existence of advanced MOCVD and ancillary technologies allow our research group to leverage this industry and create economically viable solutions to technological problems. Specifically, the results we have obtained were implemented using a production-style MOCVD reactor and thus carry extra weight outside of the research community. These results are not just proof-of-concept, but more advanced demonstrations of technology development.

The purpose of this chapter is to briefly review some of the concepts behind the MOCVD process, sometimes directing the reader to other sources for details, but primarily to introduce the special capabilities of the laboratory and equipment used to support the MOCVD growth done in this study.

3.2 MOCVD Process

In MOCVD, precursor gases are passed over the heated wafer such that controlled pyrolysis occurs, depositing the desired reagents (In, Ga, P, etc.) while waste products are carried away (H_2 , CH_4 , etc.). Stringfellow provides an excellent reference for MOCVD technology³⁶. Details of precursor properties will not be covered here and the reader is directed to this reference for more information. Additionally, growth models used in this study have been described well¹². Modifications of this growth model were used and an example growth worksheet is included in Appendix A of this document.

Essential process parameters include gas flow rates and ratios, reactor pressure, susceptor temperature, and ratio of group V to group III partial pressures at the growth front³⁶. The APMOCVD reactor has been well calibrated and characterized for GaAs, GaP, InP, InGaP, GaAsP, and AlInGaP growth, while the LPCVD system has been carefully documented across the course of this project. The essentials of InGaP growth parameters have been laid out previously⁴³ and served as a starting point for our own growth. GaAsP growth will be discussed shortly below and in further detail in Chapter 4 and Chapter 5. As growth and characterization results are presented in this thesis, details about these process parameters will be discussed.

MOCVD Reactors

The research in this thesis project was carried out using two reactors designed and built by Thomas Swan Scientific Equipment Ltd. (TSSEL). The first reactor is a manually controlled atmospheric pressure research tool (APMOCVD), in a horizontal configuration capable of deposition on single 2" wafers. Growth was carried out using

ultra-high purity hydrogen carrier gas, phosphine and arsine precursor gases along with H_2 bubbled trimethylgallium (TMGa), trimethylindium (TMIn), and trimethylaluminum (TMAI) sources. Dopant sources include dilute silane and dimethylzinc (DMZn). The system has been well documented⁴⁴⁻⁴⁶.

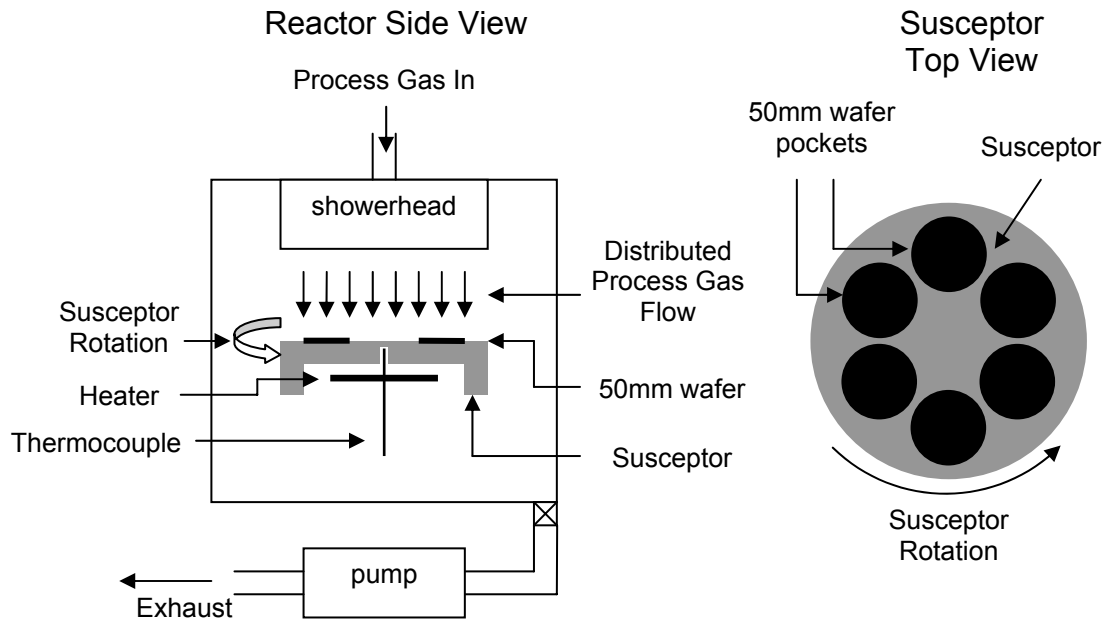


Figure 3.1 Schematic of LPMOCVD reactor, not drawn to scale. Drawing courtesy of C. Dohrman.

The second reactor was newly installed in the Substrate Engineering Laboratory at MIT during the course of the thesis project. Hence many of the processes reported here were demonstrated on both systems. The advanced, production-style system (schematically shown in Figure 3.1) is completely computer controlled. It is capable of low-pressure epitaxy using a close-coupled showerhead configuration which prevents mixing of hydride and metal-organic precursors until approximately 1cm from the wafer surface. Such a design prevents parasitic vapor phase reactions and particle formation above the wafer surface. This reactor utilizes 8" SiC coated graphite susceptors heated by a graphite resistance heater for growth on 2", 4", 6", or 8" wafers. This reactor has been

customized for group IV growth as well as III-V and includes the same source chemicals as the APMOCVD reactor in addition to trimethylantimony (TMSb), dimethylhydrazine (UDMHy), pure silane, and hydrogen-diluted germane, disilane and diborane. The system includes *in-situ* analysis capabilities with a Laytec® EpiTT reflectivity measurement system which provides real time pyrometry and single wavelength reflectivity data. Several details of this reactor system will be outlined here.

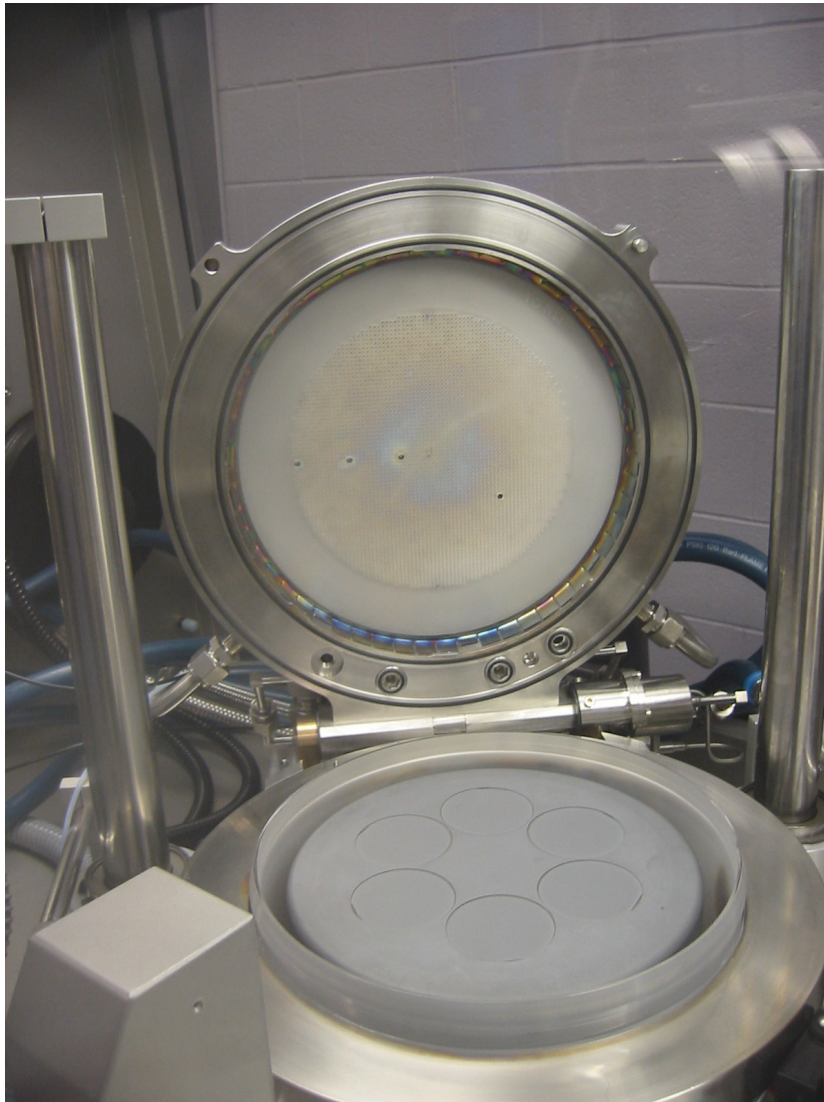


Figure 3.2 Photograph of the close-coupled showerhead, flip-top reactor in the opened position. Note that pyrometry and reflectivity data are taken through the four ports visible in the showerhead. This reactor design enables excellent control over temperature and compositional profiles.

Reactor subsystems

The centerpiece of the MOCVD reactor is the reaction chamber, shown in Figure 3.2. This consists of a vertically oriented stainless steel vessel lined with quartzware which is easily removed for cleaning. The showerhead design injects precursors evenly directly over the wafer surface through hundreds of small holes. This assures consistent boundary layer thickness and uniform gas composition across the rotating susceptor. The showerhead and chamber is temperature controlled through a heated and cooled water recirculation system which maintains temperature during all run and idle conditions. This maximizes reactor stability.

The reaction chamber is contained within an inert nitrogen atmosphere glovebox. Motivations for this feature include maintaining process cleanliness (reducing exposure of reactor internals to air (primarily of concern are oxygen and water vapor) as well as offering an extra level of safety to the operator from toxic substances in the chamber. The glovebox atmosphere is constantly recirculated through particle filters and de-oxy driers to maintain a low dew point of -75°C to -40°C . The resin drier column is regenerated under heat, vacuum and reducing atmosphere at operator's discretion to maintain optimal dew point.

As will be discussed below with regards to GaAsP growth, of paramount importance to this thesis was the effective and precise control of the susceptor temperature during growth runs. Using broadband optical pyrometry we achieve our goal of temperature measurement accuracy to within 1°C and uniformity variation of less than 1.5°C across the 8" susceptor. Calibration was accomplished under well controlled conditions including freshly cleaned and coated quartzware, uncoated susceptor and

growth pressure and gas flow rates. Real temperature measurements at three points across the susceptor were taken using quartz probes calibrated with a black-body temperature standard. In this way, power delivery requirements and thermostat setpoints which provided an accurate and flat temperature profile could be determined for any temperature up to 850°C. Optical probes cannot be used *in-situ* since coating of the probes and the changing emissivity of the various coatings on the susceptor make optical pyrometry impractical, so they are removed for growth. Ideally, stability of the temperature settings is excellent—drift of approximately +5°C with less than 1°C profile flatness change after 8 months and about 150 growth runs has been demonstrated. This performance can be degraded by aging of the graphite heater (drooping of the heating coils for example), but this was counteracted by careful observation and propping of the heater with alumina rods.

An *in-situ* reflectivity monitor (Laytec EpiTT) is also featured on the MOCVD system. This consists of a single wavelength pyrometry sensor at 950nm as well as dual wavelength reflectivity sensors—at 635nm and 950nm. While in principle this device can be set up to monitor real time growth rates and actual wafer temperatures, in practice for lattice mismatched epitaxy of a large variety of materials its use is more limited. The single wavelength pyrometry feature is useful for providing an approximate wafer temperature, but needs to be calibrated based on the wafer type being used for each growth run. Deposition of films with varying optical parameters is typically the primary goal in epitaxy; differing indices of refraction result in “Snell’s Law” reflections from the surface and layer interfaces, leading to constructive and deconstructive interference from incident and reflected light beams. Hence reflectivity of the growing wafers oscillates

with time and gives direct information about the condition of the growing layers. This is useful for gauging thickness of films (number of oscillations), growth rate (period of oscillations) and qualitative overall film quality (roughness reduces reflected intensity).

Excellent control of MOCVD growth requires accurate control of precursor injection rates to the reaction chamber. Commercially available mass flow controllers (MFCs) work well for this application and can be calibrated to deliver virtually any gas source reliably. Most typical metalorganic sources are liquid at their process temperatures (which are controlled though simultaneously heated and cooled ethylene-glycol solution baths). Usually, bubbling a carrier gas such as nitrogen or hydrogen through a liquid MO saturates the carrier so that obtaining a controllable and repeatable flow of MO vapor is relatively simple; all that is required is the MFC's reliable mass flow of the bubbling carrier gas. Unfortunately, TMIIn's high melting point of 88°C dictates that TMIIn be dealt with as a solid. TMIIn has a reasonable vapor pressure near room temperature, but since solid surface area changes as TMIIn granules vaporize, saturated flow of TMIIn in the carrier becomes difficult to maintain. The result is an unreliable delivery rate of TMIIn as a function of carrier gas flow. Although it is possible to use solution-source TMIIn to solve this problem, most crystal growers view this solution as an intentional incorporation of contaminant to the precursor. Instead, we use real time gas concentration monitors (TSSEL model Epison III) to regulate TMIIn flow. These gas concentration monitors measure the velocity of sound in the delivered gas mixture and interpolate gas composition based on expected velocity of sound through of the two constituent flows. Through monitoring of the actual flow rate of TMIIn vapor output from the bubbler, we implement a feedback loop to control the flow rate of TMIIn reliably. Unfortunately,

injecting high flow rates of carrier into warmed bubbler exacerbates thermal equilibrium problems (the carrier is chilling the TMI_n source, reducing output flow). We are able to further stabilize TMI_n flow by implementing a specially designed TMI_n bubbler (the Akzo-Nobel Hiperquad bubbler). In this design, the exposure path length of TMI_n to carrier gas is increased relative to typical bubbler design. This increases the exposure time for any incremental volume of carrier gas to TMI_n, simultaneously ensuring equilibrated temperature of the carrier and TMI_n and saturation of the carrier with TMI_n vapor.

GaAsP growth

The growth of a mixed group V compound like GaAsP is subtly more complicated than the growth of mixed cation compounds like InGaP. Some of the details of GaAsP growth will be discussed here. At elevated temperatures (approximately 450°C and above), III-V materials exhibit high group V vapor pressures. To prevent spontaneous desorption from the crystal, group V overpressures must be provided. Without a V-oversaturation, point defects form and in severe cases this can lead to wafer pitting and “balling-up,” or the formation of metallic group III droplets on the wafer surface.

In the MOCVD process chamber we typically inject the group V precursor species in great excess while limiting group III precursor flow to control reaction rates (keeping $V/III \gg 1$). Since under most growth conditions the group III precursors fully decompose, compositional control is relatively easily realized through measured injection ratio of the III precursors. Indeed, compositional calibration parameters for mixed cation compounds are *not* extremely sensitive to temperature and targeted alloy.

With growth of mixed anion compounds we must still satisfy the need for large V overpressure, but the ratio of the V precursors must also be controlled to set alloy composition. The composition of GaAsP that is deposited is determined by the relative rates of decomposition of AsH₃ and PH₃. These processes are highly variable and dependent on reaction conditions, so extra care must be taken when calibrating GaAsP growth. Figure 3.3 shows a typical calibration curve for GaAsP with a growth temperature of 725°C and V/III ratio of 100. The curve has been empirically observed to have the following behavior:

$$z = \frac{1}{\frac{1}{\alpha} \left(\frac{1}{x} - 1 \right) + 1}, \quad \text{Equation 3.1}$$

where z is the P-fraction of the deposited alloy, x is the percentage of PH₃ in the total group V precursor mass flow, and α is the fitting parameter. In practice, the excellent temperature stability of the LPMOCVD system has led to very reliable GaAsP composition calibration.

725°C GaAs₁₋₇P₇ Calibration

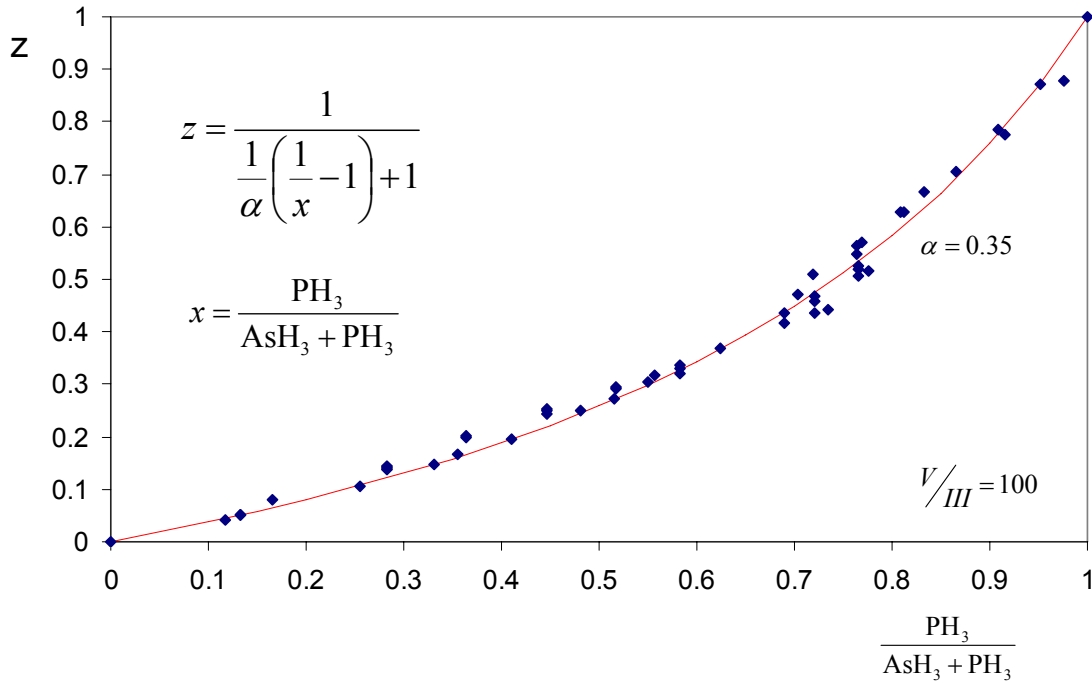


Figure 3.3 The composition calibration curve for GaAsP grown at 725°C and a V/III ratio of 100 is shown. Using equation 3.1 to fit experimentally derived composition calibration data, we get excellent predictability of GaAsP compositional control.

3.3 Characterization

The bulk of this project is the growth and characterization of device material. Accurate characterization of material quality was essential for success. More details about characterization techniques used here can be found in other work^{12, 30}. The following techniques were used and will be referred to throughout the thesis:

TEM

Transmission electron microscopy (TEM) is an extremely important tool used to *directly* obtain crystallographic information. By imaging defects in real space we can deduce the nature and quantity of dislocations, observe APBs, stacking faults and strain, and obtain information about the morphology and structure of complicated growths.

Electron diffraction patterns give us reciprocal space information about the samples and indicate sample crystallinity, Burgers vectors of dislocations and the presence of ordering. Cross section analysis gives layer thickness and morphology information while plan view analysis permits threading defect density counts.

All TEM specimens were thinned through wet grinding by hand, using continually finer grades of SiC sandpaper to an ultimate thickness of about 10 μ m. This was followed by a polishing step to remove visible scratches, using 0.03 μ m alumina particle slurry. Next, samples were mounted to a 3mm copper TEM grid and ion milled to perforation prior to viewing.

XRD

Triple axis x-ray diffraction (TAXRD) allows us to obtain rocking curves and reciprocal space maps of the structures we grow. The rocking curves give complete information about the strain state and relaxed lattice parameter of the films we grow. Reciprocal space maps (RSMs) give additional information about the quality and morphology of the samples. RSMs indicate crystallographic tilt, or deviation of the epitaxial growth orientation from the substrate crystal orientation. Analysis of the dynamical diffraction of the samples also indicates the degree of crystallinity and mosaicity of the grown layers.

PL

Room temperature and low temperature photoluminescence (PL) data probes the electronic structure of samples and indicates the nature of radiative recombination in crystals. PL gives information about quantum well and interface quality and can be used for compositional information.

CL

Complimentary to PL, cathodoluminescence (CL) also gives information about the electronic structure of crystals. CL is also available at liquid helium temperatures (down to about 9K, in practice). In CL, electrons are directly injected into the specimen using a scanning electron beam. Since the specimen is typically at an unbiased equilibrium this method removes effects of the electric field which injects carriers in electroluminescence.

AFM

Atomic Force Microscopy (AFM) was used to characterize the roughness and morphology of the sample surface. AFM is an important method for quantitatively characterizing the effects of anneals, etches and growth parameters on surface morphology.

EPD

Etch pit density (EPD) measurements were used to characterize the density of defects in low defect density samples. The etch used was (3:1):1=(x:y):z where x, y and z were volume parts with x = CrO₃ (33wt.%) aqueous solution, y=HF (48%) and z=H₂O to total (x+y)⁴⁷. PVTEM uses high magnification to discern threading dislocations that are very close together but limits overall counting area. Contrarily, EPD enlarges the defects such that they can be seen with the optical microscope and allows defect counting over very large areas. The two counting techniques are complimentary, PVTEM is ideal for densities well over 10⁶cm⁻² and EPD is best for densities well under 10⁵cm⁻².

Chapter 4 Virtual Substrates for Si to Ge Lattice Constants

4.1 Introduction

In Chapter 1 we discussed the motivation to break the GaAs lattice constant constraint of AlInGaP-based devices. In this chapter we present the enabling technology: high quality virtual substrates.

Several groups have studied the lattice engineering approach to improving green devices, but in this paper we specifically focus on improving the material quality of the engineered substrate. Other lattice engineering efforts have focused on selected area growth, epitaxial lateral overgrowth (ELOG) and hybridization (wafer bonding, individual device soldering, etc). These techniques add significant complexity and cost to manufacturing and often limit the wafer area available for device fabrication. On the other hand, compositional grading can be carried out *in-situ*, prior to device layer deposition and does not add other fabrication processing steps or reduce usable wafer area. By depositing layers with continuously increasing mismatch to the substrate, strain is introduced gradually and is relaxed through misfit dislocations parallel to the wafer surface. Dislocation glide relaxes elastic strain, using existing threading dislocations to extend misfit length. Efficient compositional grading maintains strain levels low enough to glide dislocations but not nucleate excessive dislocation populations. One requirement for efficient relaxation without dislocation nucleation is uninhibited dislocation glide. Glide can be blocked by any crystal inhomogeneity including defects, surface roughness, phase separation, and more.

GaAsP in particular was for many years a workhorse material for visible LEDs. Thick graded layers (20-50 μm) grown by hydride vapor epitaxy (HVPE) were common, but total threading dislocation densities of the structure were still much higher than those

of the native GaAs substrates (around 10^6cm^{-2})^{33, 34}. More recent work has also been done⁴⁸⁻⁵⁰, but these research projects seem to have been abandoned in favor of the then newly demonstrated GaN-based materials as excellent short wavelength visible emitters. Work has also been done with InGaP graded layers, but if studies even quote dislocation densities, they are typically relatively high (10^6 - 10^7cm^{-2})⁵¹⁻⁵³.

Using modern MOCVD reactors, we have revisited several graded material systems which give access to all lattice parameters intermediate to GaAs and GaP and we have gained the ability to minimize threading defect density and surface roughness with relatively simple methods. In this chapter we discuss our efforts with (where ∇_i denotes chemically graded layers with i varying) $\nabla_x[\text{In}_x(\text{Al}_y\text{Ga}_{1-y})_{1-x}\text{P}]/\text{GaP}$ (with y both =0 and $\neq 0$ while x increases from 0) and $\nabla_z[\text{GaAs}_{1-z}\text{P}_z]/\text{GaAs}$ (with z both increasing from 0 and decreasing from 1 for tensile and compressive relaxation, respectively).

Through the use of the high quality, low defect density (ρ_i) and simple to manufacture virtual substrates presented here, we believe our green devices will hold the greatest “real-world” promise. We present methods of lattice mismatch engineering which lead to low threading dislocation density (10^4 - 10^5cm^{-2}) virtual substrates. This technology will enable fabrication of improved green light-emitting diodes and even yellow-green semiconductor lasers and will be naturally extended to integrate III-V visible materials onto the Si platform as well.

4.2 Experimental Method

The AlInGaP and GaAsP crystal growth presented in this paper was executed by metal organic chemical vapor deposition (MOCVD) using two Thomas Swan/Aixtron

reactors. One was an atmospheric pressure horizontal 2" reactor. Carrier gas was Pd-diffused hydrogen and precursors were phosphine, arsine, trimethylgallium, trimethylaluminum and trimethylindium along with silane as an n-type dopant and dimethylzinc as the p-type dopant. A majority of the GaAsP crystal growth was performed by a low pressure, 7x2" production-style close-coupled showerhead reactor. In this reactor design, group III and V precursor gases are mixed less than 1cm from the wafer surface, avoiding parasitic gas-phase reactions prior to reaching the reaction chamber. Reactor and vent line pressures as well as gas switching sequences are computer controlled to ensure sharp compositional interfaces. To maintain composition calibrations, optical pyrometry was used to calibrate wafer surface temperature to within 0.5°C of setpoint and to maintain a flat temperature profile across the graphite susceptor. GaAsP precursors in this reactor are the same as the atmospheric reactor, but purified nitrogen was used as the carrier gas. Differences in reactor design contributed to calibration differences for GaAsP growth in the two reactors and particle counts were lower in LPMOCVD process runs, but otherwise differences in material quality were not apparent.

GaAs wafers nominally $\langle 100 \rangle$ oriented and 2° miscut towards the nearest $\langle 110 \rangle$ were prepared for growth as described in⁵⁴. $\langle 100 \rangle$ GaP wafers miscut 10° towards the nearest $\langle 110 \rangle$ were employed for the AlInGaP growth and GaP wafers offcut 2° towards an orthogonal $\langle 110 \rangle$ were used for compressive GaAsP growth. All GaP wafers were prepared with a 60s etch in 15:1:1 H₂SO₄:H₂O₂:H₂O followed by a DI H₂O rinse and nitrogen blow dry.

Low pressure growth was carried out at 100Torr. To avoid pit formation, V/III ratio was maintained at greater than 100 for all growth. Growth rates were typically set near 7Å/s. All growth was initiated with a 500nm homoepitaxial layer to bury residual contamination on the wafer surface.

Composition and strain relaxation of each sample was evaluated through (004) and (224) rocking curves on either a Bede triple-axis x-ray diffractometer with a Rigaku RU200 rotating Cu-anode generator operating at 60kV, 200mA, or a Bruker D8 Discover using parabolic mirror focusing optics and a LiF analyzing crystal with a sealed tube Cu anode generator running at 40kV and 40mA. For quaternary growth, composition was determined approximately by both lattice constant (x-ray) and band gap (cathodoluminescence) measurements. Sample microstructure was characterized by TEM in cross section (XTEM) and plan view (PVTEM) using either a JEOL 200CX, 2000FX or 2011 microscope, each operated at 200kV. XTEM samples were cleaved along $\langle 110 \rangle$ directions. PVTEM and XTEM samples were manually polished to about 10 μm and thinned by ion mill (4-6kV Ar-ion guns). PVTEM threading dislocation counts were carried out through imaging of $>1000\mu\text{m}^2$ in a $g=\langle 220 \rangle$ -type diffraction condition. Etch pit density measurements were used to count low threading dislocation densities ($\rho_t \leq \sim 10^6 \text{cm}^{-2}$) following the method in⁴⁷. Surface morphology was studied and RMS roughness measurements calculated with a Nanoscope III Si-cantilever AFM run in tapping mode.

4.3 Graded (Al)InGaP, Branch Defects

Previous work by Kim²⁹ and McGill⁴¹ described techniques to obtain graded InGaP virtual substrates of good quality (threading defect density, ρ_t , of about $3 \times 10^6 \text{cm}^{-2}$, acceptably low for optical device fabrication). These results show that growth temperature adjustments during graded buffer growth delay the onset of “branch defect” formation and dislocation density escalation. By avoiding branch defects, the primary impediment to dislocation glide in graded InGaP, we expect that lower ρ_t is attainable.

Our initial focus was to further optimize the early InGaP/GaP virtual substrate platform by removing branch defects with the addition of other chemical species to the graded region. Several different material systems were analyzed and their effect on final threading dislocation density was ascertained. These compositionally graded buffers were compressively relaxed layers of AlInGaP or AlInGaP:Si, where the strain incorporation rate was controlled at $-0.4\% \mu\text{m}^{-1}$. In the $\nabla_x \text{In}_x(\text{Al}_y\text{Ga}_{1-y})\text{P}$ buffers, y was kept constant at a value of approximately 0.2 while the n-type doped $\nabla_x \text{In}_x(\text{Al}_y\text{Ga}_{1-y})\text{P}$ buffers additionally employed a Si concentration of about $2.0 \times 10^{18} \text{cm}^{-3}$ as measured by SIMS analysis. For these studies the Al fraction y was intentionally kept relatively low to prevent growth difficulties commonly experienced with high Al fraction, especially at low In fraction.

For all conditions tested we observed an increase in threading dislocation density compared to the early InGaP work (results are shown in Figure 4.1). Despite improvements on the MOCVD reactor design, at best we were only able to reproduce early results ($2.3 \times 10^6 \text{cm}^{-2}$ at 5.55\AA , PVTEM shown in Figure 4.3). The addition of

aluminum to the graded layers did improve ρ_t by as much as a factor of four over the higher ρ_t , constant-temperature InGaP buffers, but introduced weak branch defects which are visible in Figure 4.3a). Attempts to further lower ρ_t using Kim's temperature-adjustment method offered relatively little improvement. Even with graded growth temperature, we observed an increase in ρ_t by approximately a factor of two over the best InGaP data. Additionally, adding Si to the graded structure increased ρ_t by a factor of almost ten, to $1.5 \times 10^7 \text{ cm}^{-2}$ at 5.54 \AA . Thus, if doping the InGaP graded buffer is required as in bottom contacted devices, then higher dislocation densities must be tolerated or top contact devices should be used on InGaP graded buffers.

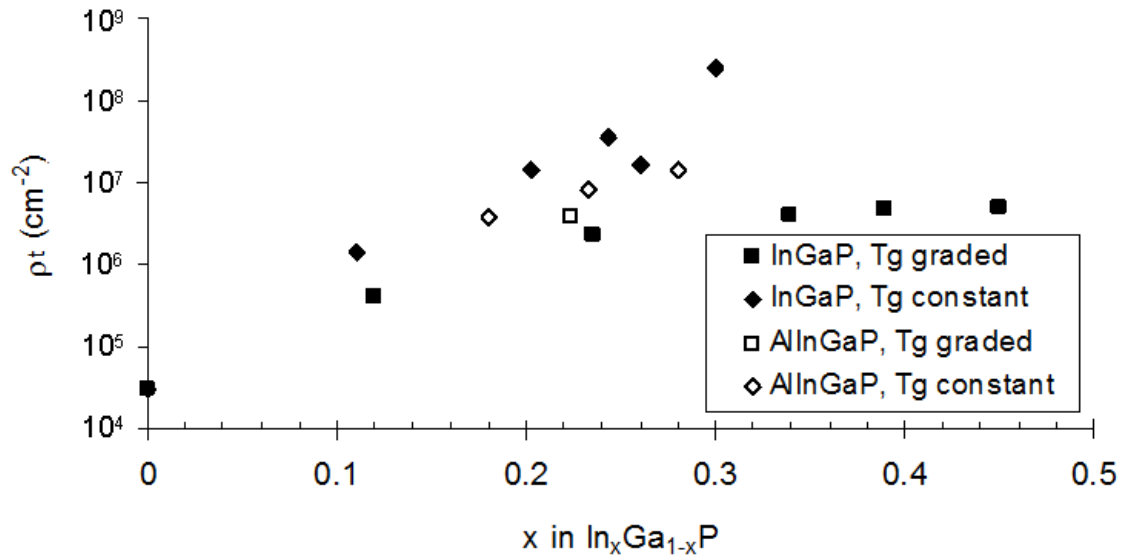


Figure 4.1 Threading dislocation density (ρ_t) as a function of final composition in the graded buffer. The system with the lowest ρ_t is the growth temperature-optimized, undoped InGaP. Set includes data from Kim⁴⁶.

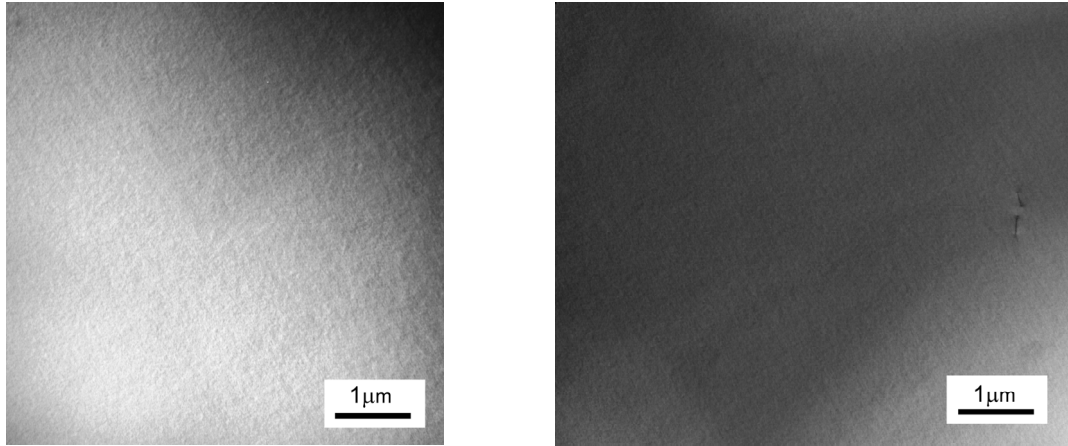
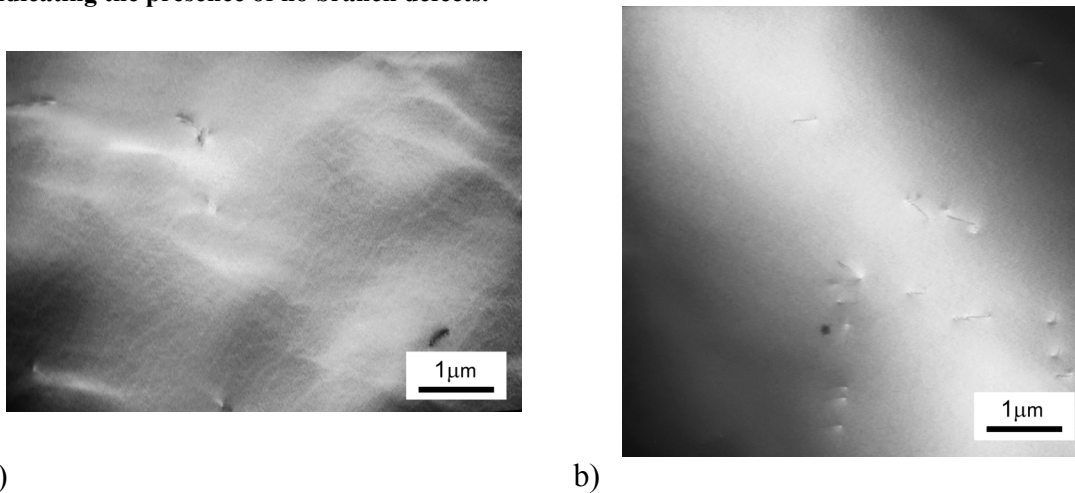


Figure 4.2 Plan view TEMs of high quality temperature-adjusted InGaP, graded to a final composition of 24%In with ρ_t of $2.3 \times 10^6 \text{ cm}^{-2}$. Note the even contrast throughout these images indicating the presence of no branch defects.



a)

b)

Figure 4.3 a) PVTEM of constant temperature AlInGaP graded buffer. Note the bright branched regions of contrast, the phase separation defects which impede dislocation glide. These branch defects elevated ρ_t to a relatively high value of $1.5 \times 10^7 \text{ cm}^{-2}$. b) Applying the InGaP temperature optimization to AlInGaP reduced the branch defect strength and lowered ρ_t to $3.7 \times 10^6 \text{ cm}^{-2}$. Pileups of dislocations such as the one pictured here account for a majority of the total thread density.

Kim et al.⁴⁶ optimized graded InGaP to a maximum ρ_t of about $3 \times 10^6 \text{ cm}^{-2}$. Kim concluded that the formation of branch defects contributed to the escalation of threading dislocation density. Quitoriano and Fitzgerald recently published results that support the hypothesis that branch defects are actually regions of phase separation⁵⁵. Kim presented a temperature optimization scheme in which progressive lowering of the growth temperature with grading kinetically inhibits the material. Thus, as the graded layer in

increasingly InP-rich (mechanically softer with higher dislocation velocities), reduced growth kinetics subdue phase separation defects.

Quitoriano and Fitzgerald⁵⁵ attributed observed threading dislocation escalation to phase separation defects in both InGaAs and In-rich InGaP films (In fraction >0.7). McGill further concluded that these types of defects arise from In-clustering at the growth surface⁴¹. We argue that similar clustering and phase separation takes place in Ga-rich (Al)InGaP systems (In fraction <0.3) as well. Weak branch defects were observed in this work and associated with increased threading defect density as shown in Figure 4.3a).

Indium and gallium do not completely intermix at the growth surface and instead segregate to Ga-rich and Ga-poor regions. This surface clustering causes strain undulations in the crystal which later blocks dislocation glide in the bulk^{41, 46, 55}. Without free dislocation movement, relaxation is inhibited, building up strain and increasing dislocation nucleation rates. Dislocation blocking manifests higher threading dislocation densities; as shown in Figure 4.1, which shows the dramatic divergence of ρ_t data between the constant-temperature and graded-temperature InGaP graded buffers near an indium fraction of 0.2.

The improvement of the temperature-graded AlInGaP buffers over the constant-temperature InGaP buffers indicates that different optimization scheme may further improve the quality of the AlInGaP graded buffers. Dislocation velocity dramatically increases as InGaP becomes more InP-rich⁵⁶⁻⁵⁸. Similarly, it is expected that the addition of Al to InGaP will lower dislocation velocity overall and delay the onset of this velocity shift with In fraction. Therefore improvement of the AlInGaP graded buffers may be

possible through higher temperature growth and/or delay of the growth temperature grade.

The addition of aluminum and silicon to the graded layers was hypothesized to change the kinetics of chemical species at the growth surface; our hope was to increase intermixing by reducing adatom mobility with the addition of a greater range of adatom sizes at the growth front. The improvement of the constant temperature buffers with Al shows that we were mildly successful. As evidenced by the by the overall increase in ρ_t of the Al-containing structures and the observation of increased branch defect density in plan view TEM, these quaternary structures actually experience greater phase separation than the Al-free structures. It may be possible to find process conditions which better avoid branch defect formation, but this solution is not expected to be particularly successful. Instead, to dramatically reduce the defect density of the system we must look towards selection of a materials system with advantageous thermodynamics of mixing.

4.4 Graded GaAsP, Removal of Branch Defects

Despite the fact that the AlInGaP growth temperatures (725°C) are well above the material's calculated thermal equilibrium miscibility gap of 688°C⁵⁹ (even higher growth temperatures are not practical as the growth mode enters into the thermodynamically limited regime where growth rate drops precipitously), the non-equilibrium nature of MOCVD and high adatom surface mobility allows clustering to take place at the growth surface. To alleviate this, we look towards other graded materials systems where intermixing is thermodynamically more stable, i.e. systems with a smaller enthalpy of mixing. In GaAsP, calculated phase diagrams show a miscibility gap at only 4°C⁵⁹ and

the system is often quoted as being completely miscible⁶⁰. Additionally, using the regular solution model, Stringfellow⁶¹ showed that for III-V ternary systems with non-negligible lattice mismatch (systems other than AlGaAs and AlGaSb), InAsP and GaAsP have the smallest interaction coefficients and therefore have the smallest propensity for phase separation. With reduced thermodynamic driving force for phase separation, we hypothesized and confirmed that branch defects should be weak or non-existent in GaAsP graded systems. Figure 4.4 shows PVTEM and Figure 4.8 shows XTEM of graded GaAsP free from branch defects.

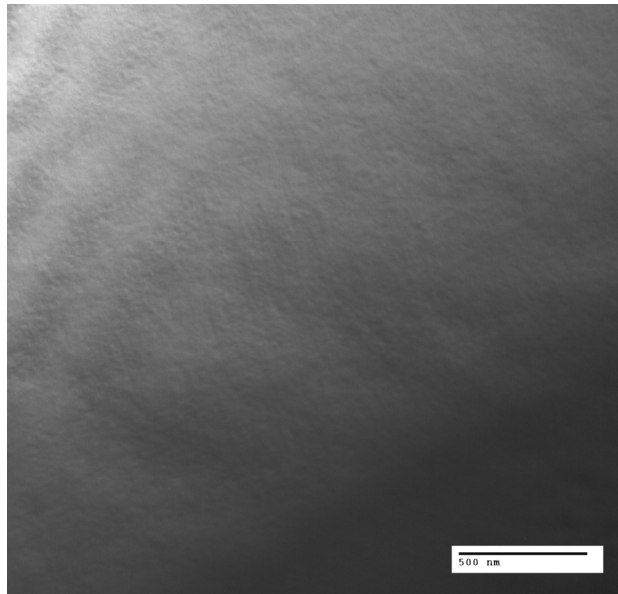


Figure 4.4 PVTEM image of tensile relaxed GaAsP with lattice matched InGaP layer on top. Note the lack of branch defects.

We have studied the growth of tensile and compressive GaAsP on GaAs and GaP substrates. Control over MOCVD growth of mixed-anion compounds is notoriously more difficult than mixed-cation compounds due to the increased sensitivity of the group-V distribution coefficients. Relative incorporation rate of P to As depends on the decomposition rates of the group V hydrides, and the difference in bond strengths in

phosphine and arsine molecules dictates their very different cracking dependence on temperature. Therefore, composition calibration of MOCVD grown GaAsP is quite temperature sensitive and non-linear. At higher temperatures, phosphorus incorporates more readily than arsenic resulting in as much as a twofold increase in solid P fraction for a set phosphine to arsine ratio with 50°C temperature increase. For this reason, optical pyrometry was used to carefully calibrate the reaction chamber to ensure a flat and accurate temperature profile across susceptor under growth conditions.

Tensile GaAsP was grown at a grade rate of approximately $0.2\% \mu\text{m}^{-1}$ while compressive GaAsP was grown at about $1.8\% \mu\text{m}^{-1}$. Each sample growth process began with a 500nm homoepitaxial layer followed by constant grade rate and growth rate buffer and finished with an approximately 1000nm layer of constant composition growth at the same composition as the final layer in the graded buffer. The compositional grading was executed in two-minute growth steps.

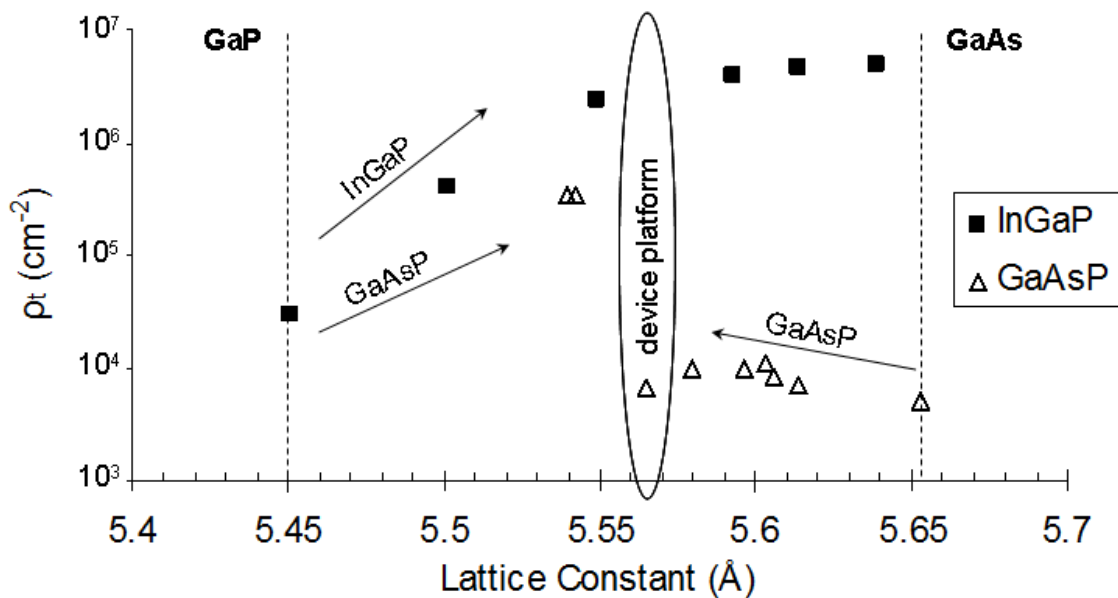


Figure 4.5 Comparison of ρ_t as a function of lattice constant for InGaP, tensile and compressive GaAsP. There is very little threading dislocation escalation in the GaAsP samples.

As predicted, GaAsP growth exhibited no signs of branch defects (Figure 4.4), and threading dislocation density measurements showed a dramatic reduction in ρ_t (of several orders of magnitude) compared to the mixed-cation grades. A comparison of ρ_t for a variety of virtual substrates is shown in Figure 4.5. As expected in compositionally graded layers, the uniform cap layers contained small residual strains, of typically +/- 0.1% to 0.2% (tensile on GaAs, compressive on GaP).

The highest quality virtual substrates we have produced are tensile relaxed GaAsP on GaAs. Etch pit density (EPD) measurements corroborated by plan view TEM (PVTEM) dislocation counts show very low dislocation densities in our final virtual substrates, near 10^4cm^{-2} . The limitations of PVTEM here are apparent when we note that imaging a single threading dislocation in $1000 \mu\text{m}^2$ of sample area (15-25 TEM images) corresponds to a thread density of 10^5cm^{-2} .

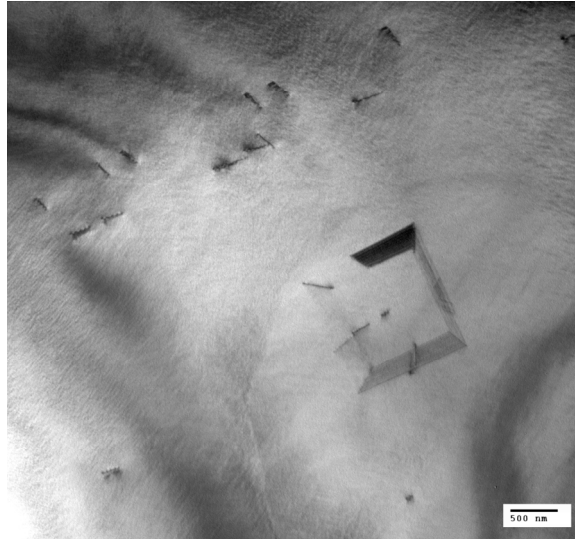


Figure 4.6 PVTEM image of tensile relaxed InGaP layer on high quality GaAsP graded buffer. Note the high density of threading dislocations and area of stacking faults.

The movement of dislocations is dramatically influenced by the sign of strain in the host crystal. Compressive strain is typically chosen for metamorphic systems because this sense of the strain tends to prevent dislocations from dissociating into partial dislocations as they do in tensile layers^{62,63}. Alternately in tension, greater glide force is exerted on the leading 90° partial dislocation giving rise to dissociation and a trailing 30° partial. Given their greater physical volume compared to the full dislocation, partial dislocations separated by an area of stacking fault are more likely to encounter an inhibiting force (from another dislocation, impurity, or surface roughness for example) and therefore tend to pile up and increase threading defect populations (see Figure 4.6 where a mildly tensile relaxed InGaP film led to a large increase in threading defect density). For this reason, a tensile metamorphic system must be graded more slowly to result in a low defect density structure which avoids entanglement of the dislocations. As shown in Figure 4.6, tolerance of ρ_t to tensile strain in InGaP is quite limited, and tensile InGaP was not studied in this work.

Although the strain incorporation rate of $0.2\%\mu\text{m}^{-1}$ used here is low by modern standards of MOCVD, this is much higher than typical grade rates used in HVPE ($\sim 0.03\%\mu\text{m}^{-1}$). We have shown that this dramatic increase in grade rate, when used in a modern reactor, does not also increase the final TDD of the material. Therefore we must conclude that dislocation-dislocation interactions are not preventing efficient glide in the MOCVD samples and that factors other than self-interactions were present in the older HVPE work. We believe that the present material benefits from growth in the cleaner well-controlled environment of a modern production reactor. Heterogeneous nucleation of dislocations was likely very prevalent in HVPE reactors and decades of improvement in precursor purity and reactor design have reduced gas phase nucleation and particle population at the growth surface, effectively removing heterogeneous dislocation nucleation sites. Note that one of the primary design goals of the close-spaced showerhead reactor used in this study was the prevention of particulate generation due to parasitic reactions in the gas phase above the wafer.

Additionally, we observe that the tensile GaAsP layers are much smoother than the other compressive epitaxial layers we observed. AFM studies of as-grown buffers show that the grown layers are extremely smooth. Step bunching is avoided in favor of step flow for buffers grown on on-axis GaAs, as shown by the 4\AA step height in Figure 4.7. We believe that the lack of heterogeneous dislocation nucleation sites and smooth surfaces combine to effectively starve the graded system of dislocation nucleation resulting in the extremely low dislocation densities we have observed.

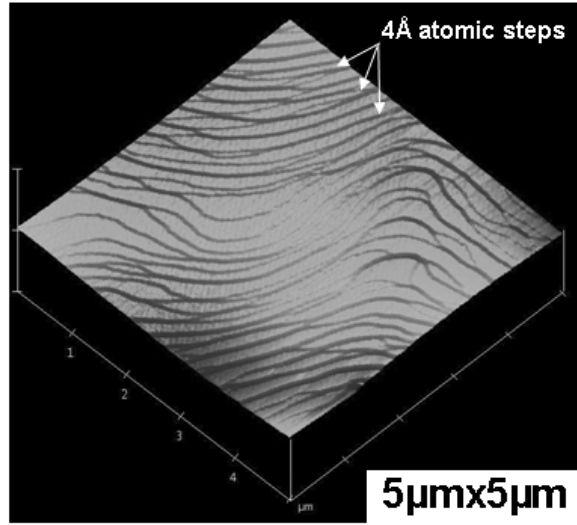


Figure 4.7 5µm square AFM scan of a typical on-axis (001) GaAsP tensile graded buffer showing atomic steps of approximately 4Å height. RMS roughness is 0.78nm.

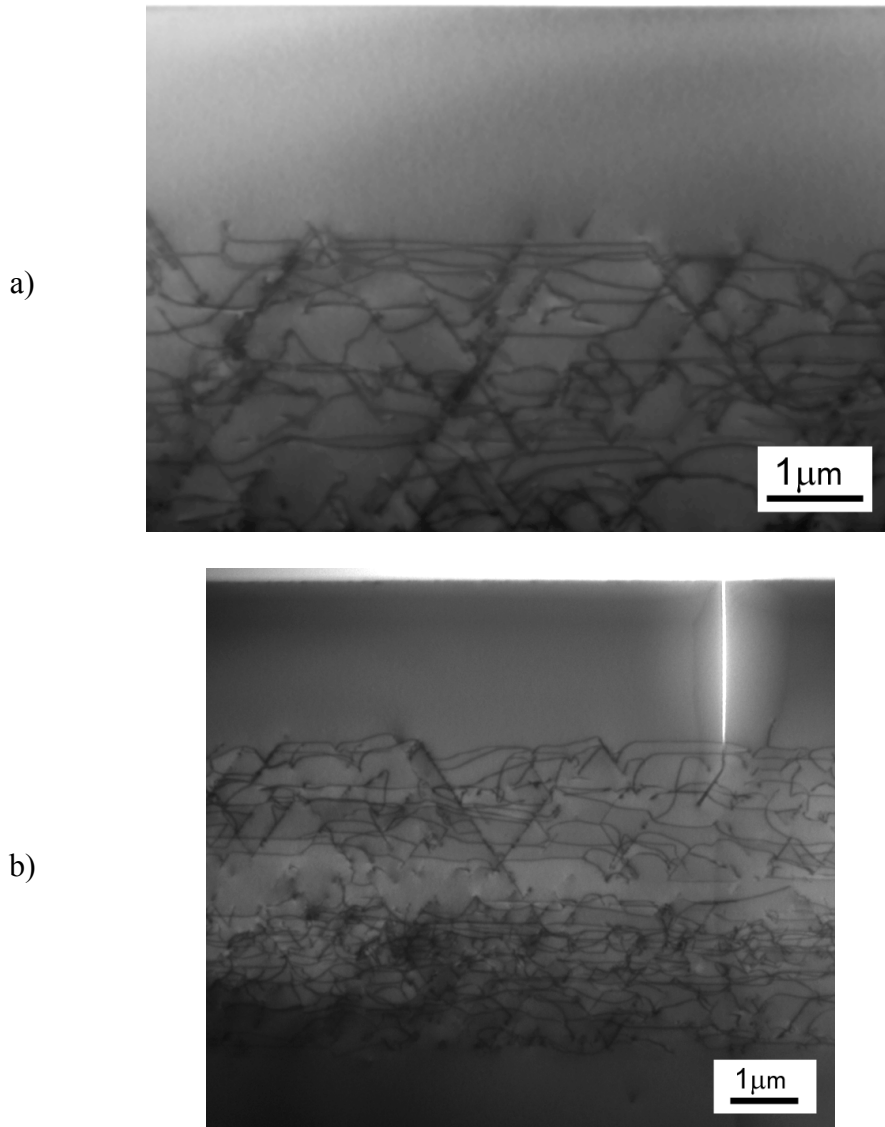


Figure 4.8 Cross section, $\langle 022 \rangle$ bright field TEM of a) tensile graded GaAsP exhibiting a crack. b) Cracks can be avoided through slower grade rates but this requires the growth of relatively thick layers.

Unlike compressive films, tensile layers are also subject to cracking (Figure 4.8 b)); we found this to be the greatest limitation of tensile GaAsP metamorphic buffers. For a grade rate of $0.2\% \mu\text{m}^{-1}$, as P fraction of 0.5 is approached, threading dislocation and stacking fault densities are very low but cracking begins (buffer thickness at this point is already $\sim 10 \mu\text{m}$). Thus, to relax tensile graded GaAsP buffers beyond about $z=0.5$ without

initiating cracks, very slow grade rates or crack-hardening techniques (such as strained superlattices) must be employed. This makes virtual substrate growth long or complicated, respectively.

Compressive GaAsP relaxation on the other hand is not subject to cracking or dislocation dissociation, and therefore along with the absence of phase separation, extremely high grade rates can be employed with minimal deterioration of final film quality. In a typical sample (see XTEM in Figure 4.9), we measure a ρ_t of $3.3 \times 10^5 \text{ cm}^{-2}$ for a structure where z has been graded from 1 to 0.55 at $1.5\% \mu\text{m}^{-1}$. Note that this is only a factor of ten increase over ρ_t of the native GaP substrate and that the GaP substrates used were relatively worse than the GaAs. This very low final dislocation density is not expected to be detrimental to the performance of optical devices built on this platform. Higher quality GaP substrates are also commercially available and should provide even lower final values of ρ_t .

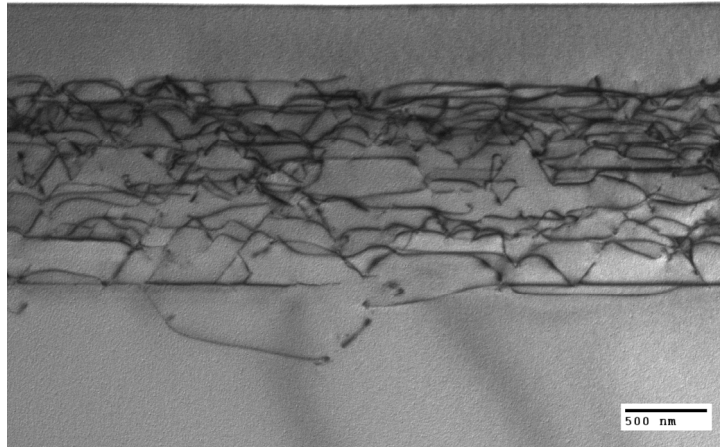


Figure 4.9 Cross section, $\langle 022 \rangle$ bright field TEM of compressively graded GaAsP with P-fraction of 0.55 at top and GaP substrate on bottom. No phase separation or cracking is apparent.

We also note that the increase in ρ_t is relatively more rapid with the same amount of absolute strain incorporation in the compressive system than in the tensile. We believe

that this is due to the different nature of the surface roughness of the compressive layers since the compressive have higher overall roughness than the tensile.

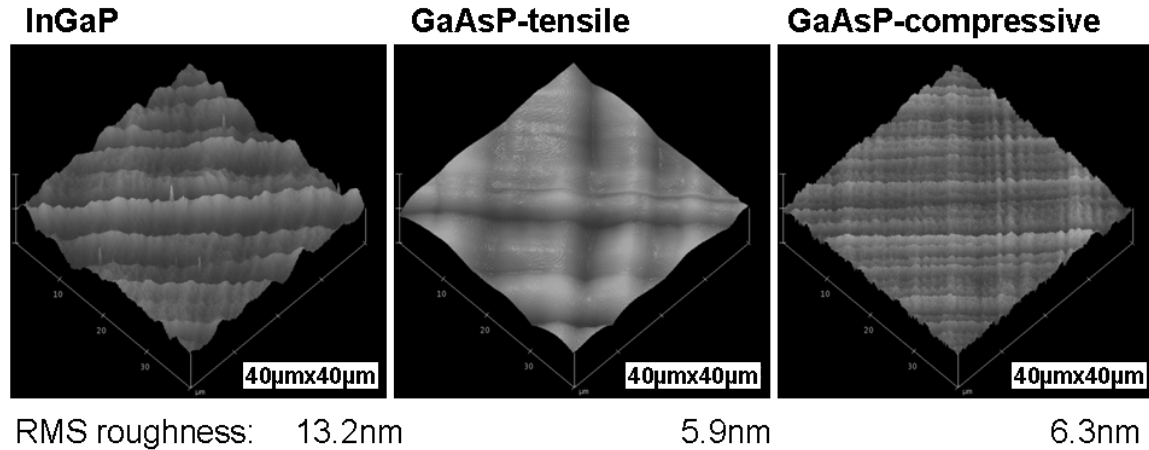


Figure 4.10 Comparison of AFM scans on three metamorphic platforms. Each sample has relaxed identical absolute amounts of strain. All images are set at the same length scales.

As shown in Figure 4.10, the surface morphology of the compressive and tensile GaAsP with equal strain relaxation is significantly different. While the RMS roughness in a $40\mu\text{m}$ square scan is very nearly the same (5.9nm for the tensile and 6.3nm for the compressive) and much less than the compressive InGaP buffers (13.2nm), the compressive GaAsP films show a much shorter characteristic roughness wavelength while the tensile GaAsP buffer is locally much smoother. This is quantified in $5\mu\text{m}$ square scans: the tensile buffer has an RMS roughness of 0.78nm (Figure 4.7) while that of the compressive buffer is 3.7nm. Tensile strain tends to keep layers smooth, but crosshatch in high grade rate films roughens the layers. Strain fields extending to the growth surface from underlying misfit dislocations cause chemical potential fluctuations and uneven adatom sticking rates. This causes slight local growth rate differences which are observed as crosshatch roughness. In the high grade rate compressive films, misfit dislocations are relatively closer to the crystal surface during growth and therefore the

crosshatch effect is enhanced. Although the local roughness of the tensile sample is very low, the presence of cracks increases roughness of the 40 μ m scan. This is confirmed by looking at the roughness of a sample with few cracks (at 1.34% misfit). Here the 40 μ m square scan has a lower RMS of 2.4nm and a similar roughness in a 5 μ m scan of 1.2nm. The faster grade rate of this sample resulted in slightly greater local roughness, and minimal discrepancy between roughness in large and small scan sizes. Most importantly, we see that ρ_t correlates well with local surface roughness; this highlights the importance of simultaneously removing surface roughness and branch defects to maximize dislocation glide velocity and therefore minimize threading defect density. To summarize, Table 4.1 shows how RMS roughness increases with grade rate.

Table 4.1 Description of several GaAsP grades, showing relationship of grade rate, cracking, RMS roughness and ρ_t .

	A	B	C
Grade rate	slow	medium	very fast
GaAsP Misfit	+1.55%	+1.3%	-1.65%
Crack Density	high	low	zero
RMS 40μm	5.9nm	2.4nm	6.3nm
RMS 5μm	0.78nm	1.2nm	3.7nm
ρ_t	$6.5 \times 10^3 \text{cm}^{-2}$	$1.0 \times 10^4 \text{cm}^{-2}$	$3.3 \times 10^5 \text{cm}^{-2}$

4.5 Conclusions

From our discussion we see that the final threading dislocation density of the graded buffers studied depends on surface roughness and phase separation defects, both of which slow dislocation glide velocity, increasing nucleation rates. Very smooth mismatched GaAsP films have extremely low defect densities and experience very little escalation in defect density with continued grading. These films contain very few heterogeneous dislocation nucleation sites and dislocation velocities are high during growth at a relatively high temperature of 725 $^{\circ}$ C. Compressive GaAsP does not suffer

from the phase separation issues found in InGaP but has slightly greater surface roughness than tensile GaAsP. This results in slightly increased impedance to dislocation glide and therefore faster escalation of defect densities. InGaP graded buffers suffer from branch defects as well as higher surface roughness and thus have the highest values of ρ_t . Maximizing dislocation velocity in (Al)InGaP graded buffers requires adjusting growth temperature to delay onset of branch defect formation. While adding Al to the InGaP buffer seems to delay defect formation as well, new growth temperature optimization schemes will be needed but are not expected to be particularly successful compared to the GaAsP buffers.

In conclusion, we have demonstrated several approaches to growing high quality metamorphic layers at all lattice constants intermediate to GaP and GaAs (Si and Ge). By avoiding mixed-cation alloys of (Al)InGaP, we also avoid phase separation defects and minimize surface roughness. Our methods yield very low ρ_t virtual substrates in very manufacturing-friendly structures on GaP or GaAs. Integration of these structures on Si, SiGe or Ge is also very feasible and holds promise for new technological applications.

Chapter 5 Microstructural Control of (Al)InGaP on GaAsP

5.1 Introduction

In Chapter 4 we presented an excellent virtual substrate technology to bridge the lattice mismatch between GaP or GaAs and compositions of AlInGaP of interest. In this chapter we present work focusing on optimization of AlInGaP microstructure on the GaAsP platform. Crystal growth and characterization results showing excellent control over the InGaP/GaAsP interface, CuPt-B ordering in InGaP, and phase separation defects in InGaP will be covered.

5.2 Method and Results

MOCVD growth of a large range of InGaP alloys was carried out. All InGaP samples were lattice-matched to high quality fully relaxed virtual substrates of GaAsP. The virtual substrates consisted of compositionally graded GaAsP buffers grown on 2° offcut GaP. Growth precursors were TMGa, TMin, PH₃ and AsH₃, while TMSb was used as a surfactant. All growth was carried out using an 8” production-style Thomas Swan/Aixtron close-coupled showerhead MOCVD reactor operated at 100mTorr with 20slm of N₂ as the carrier. Except when noted, minimum V/III ratio for all growth was 75.

TEM, XRD, AFM, CL and PL were carried out to characterize the microstructure and electronic nature of the InGaP. (022) and (004) bright field TEM images were generated using a JEOL 2011 High Contrast Digital TEM operated at 200kV. A Nanoscope III AFM operated in tapping mode generated surface images. Luminescence spectra were taken using standard lock-in techniques: CL data was generated using a JEOL 6320 SEM at 10kV; spectra were obtained with an Oxford MonoCL parabolic

collection mirror and spectrometer along with a cooled Hamamatsu Multialkali PMT. PL was provided with an approximately 80mW, 488nm Ar ion laser; spectra were taken using an Acron SpectroPro spectrometer with 1nm resolution and Si photodiode.

CuPt-B atomic ordering in InGaP was observed under most growth conditions. Disorder was controlled through variation of growth temperature or the use of TMSb as a surfactant. The color of direct band to band photoemission was measured across a wide range of InGaP compositions. This data provides a mapping of band gap for completely relaxed InGaP at largely unstudied lattice constants.

Phase separation defects in InGaP were observed under low V/III ratio and low growth rate conditions. While these defects do not seem detrimental to the overall morphology of the InGaP heterostructures, they do serve as non-radiative recombination centers, preventing luminescence. Through optimization of growth parameters, these defects are suppressed.

Instability of the mixed cation GaAsP virtual substrate surface during temperature ramps in the MOCVD reactor led to extremely high defect densities in the subsequently grown InGaP layers. Deposition of thin single-cation passivation layers such as strained GaAs or lattice matched InGaP immediately after growth of GaAsP stabilized the material ensuring high quality growth.

Mechanisms for each of these growth defects and their resolutions will be discussed below.

5.3 Ordering

A well-known phenomenon in the GaAs-matched AlInGaP system is CuPt-B type ordering^{64, 65}, segregation of indium and gallium to alternating {111} planes (see Figure

5.1). Ordering reduces the band gap of InGaP by a considerable amount, from 50meV to as much as 160meV, by lowering the conduction band edge⁶⁶. CuPt-B ordering is indicated by the presence of superspots in a [110] zone-axis transmission electron diffraction (TED) pattern. Similarly CuPt-A order is seen in $[1\bar{1}0]$ TED patterns. In order to obtain the highest possible band gap, active regions we must be able to control (i.e. prevent) ordering. It is suggested that ordering is made possible by the particular surface reconstruction of the wafer during crystal growth^{44, 59, 67, 68}; P-dimers arrange to create groves along a $\langle 110 \rangle$ direction which help to facilitate the separation of In and Ga atoms at the growth front. Specifically, in a P-rich environment, a 2x1 surface reconstruction arises, consisting of P-dimers aligned along the $[\bar{1}\bar{1}0]$. Due to the InGaP alloy size mismatch, the 2x1 reconstruction produces alternating compressed and dilated regions in the cation sublayer. This in turn promotes the alignment of In and Ga atoms in alternating [110]-oriented rows. This surface structure is propagated and metastably frozen into the bulk during subsequent deposition, yielding CuPt-B ordering domains throughout the bulk.

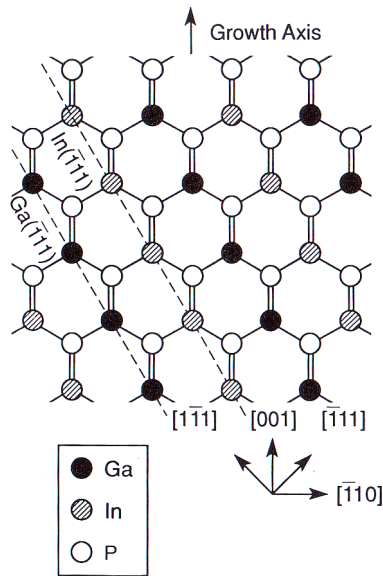


Figure 5.1 Perfect ordering in $\text{In}_5\text{Ga}_5\text{P}$ consists of alternation of the In and Ga species on {111} planes. This additional crystal symmetry lowers the band gap of the crystal. Reproduced from Zunger⁵⁹.

One suggested solution to avoiding ordering is to use surfactant-mediated growth where a chemical species immiscible in the crystal is included in the precursor flow⁶⁹. The surfactant rests at the growth front, impeding the diffusivity of other species and preventing the surface reconstruction that leads to ordering. One surfactant precursor choice is trimethylantimony, which cracks to leave Sb atoms on the surface. One major requirement of this approach is that these relatively large atoms do not incorporate at significant rates into InGaP and thus do not otherwise change the electrical or mechanical properties of the crystal.

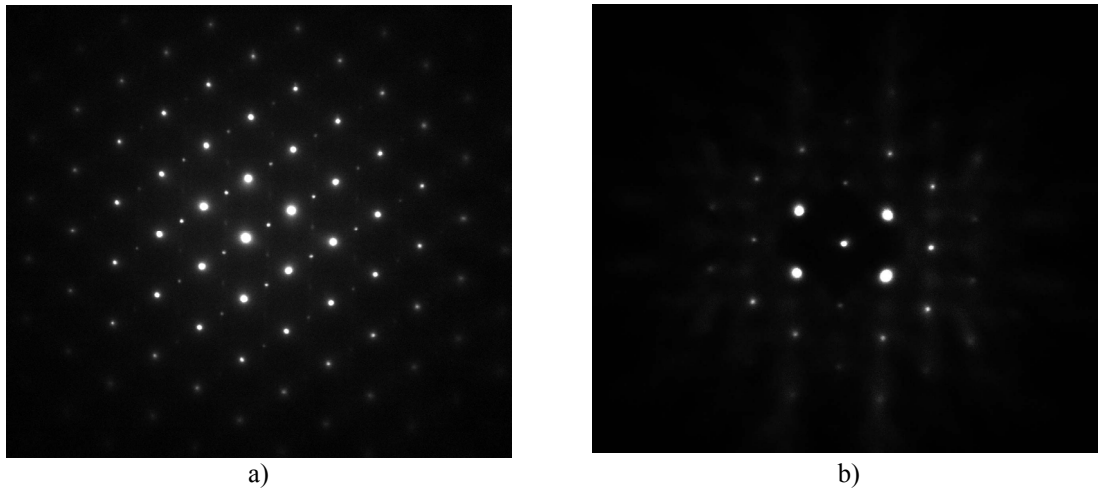


Figure 5.2 Transmission Electron Diffraction (TED) allows simple detection of CuPt order. The presence of two types of superspots in a), the [110] TED pattern, indicates CuPt-B order of both variants. From the $[1\bar{1}0]$ zone axis TED pattern in b), the lack of superspots indicates no CuPt-A order.

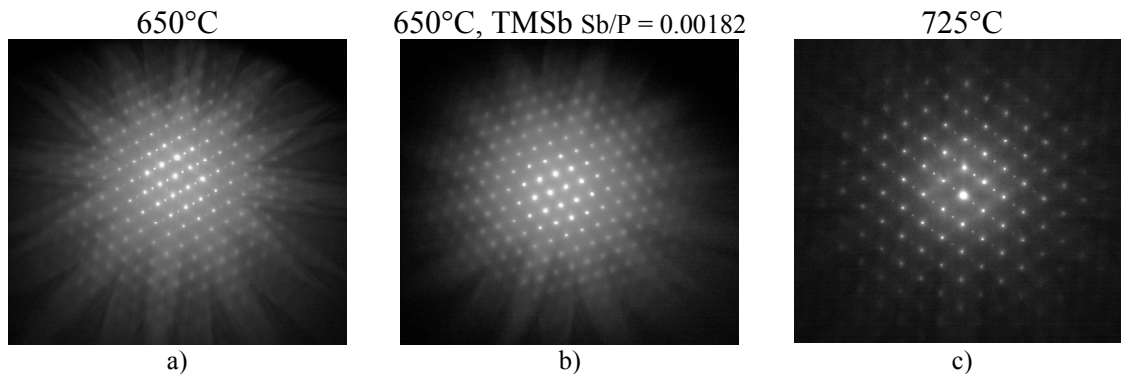


Figure 5.3 Transmission electron diffraction images of InGaP. The presence of superspots in a) indicates CuPt-B ordering, the absence of superspots in b) indicates disorder, and the weakness of the superspots in c) indicates weaker order. The samples shown in a) and b) were grown at 650°C but b) also included a small flow of TMSb as surfactant. Sample c) was grown at 725°C.

Because our objective is to obtain the shortest wavelength possible in the AlInGaP system, we have investigated the control of CuPt ordering in $\text{In}_x\text{Ga}_{1-x}\text{P}$ (with x between 0.2 and 0.4) through manipulation of growth temperature as well as the use of surfactant-assisted growth (see Figure 5.3). As shown in Figure 5.2, InGaP growth at 650°C (wafer temperature) exhibits strong CuPt-B order of both variants, but no CuPt-A order. The effect on band gap, as indicated by cathodoluminescence (CL) of the relaxed InGaP

layers, is quite strong at all compositions studied. Recombination of carriers injected by the electron beam is expected to occur across the direct band gap, generating photons of the band gap energy. As indicated in Figure 5.4, the observed transition energies are 10-20 nm longer than the predicted value, corresponding to 45-85 meV lower in energy.

By increasing the growth temperature of the InGaP layers to 725°C we are able to remove the effect of ordering. CL measurements show transitions very close to those predicted for direct material and TED patterns show the presence of only a low degree of ordering. In fact one variant of ordering was completely removed while the other was much decreased. These results are consistent but typically more successful than earlier reports regarding removal of atomic order in GaAs-matched InGaP. We can understand mechanism of this effect through a relatively simple growth model wherein the significantly greater growth temperature serves to increase solid-state diffusion close to the growth surface, effectively randomizing the crystal.

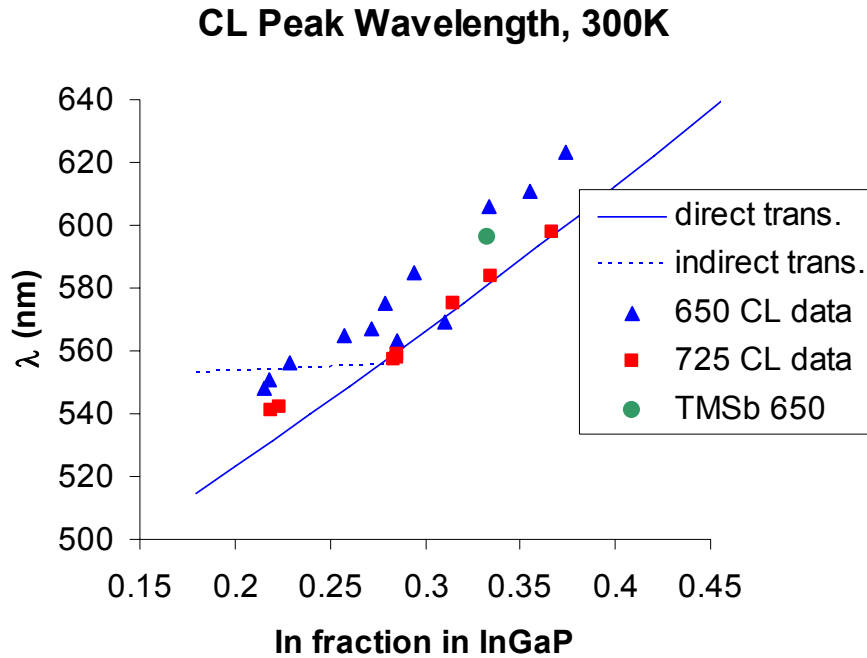


Figure 5.4 Plot of CL peak wavelength as a function of In fraction in InGaP and growth conditions. Also shown are traces for the expected wavelength of direct and indirect transitions, as predicted in the literature. Growth at 725°C results in higher band gap material and shorter wavelength CL as compared to 650°C growth.

One suggested model of ordering is given by Kurtz et al.⁷⁰ wherein the observed dependence of degree of ordering on growth rate was explained through the comparison of characteristic timescales of microscopic events. The model assumes a two-step process to the incorporation of cations into the frozen film. The first step is the surface diffusion of adatoms for a time t_s , the surface residence time. This is essentially the span of time from adatom arrival and adhesion to incorporation into the film and is equal to L_s/R_g where L_s is about the thickness of a monolayer and R_g is the growth rate. For the growing crystal to be ordered, there must be sufficient time for the adatoms to be arranged in the ordered configuration. The characteristic timescale for this to take place is τ_s , where $\tau_s = \delta_s^2/D_s$ with D_s is the relevant atomic diffusivity and δ_s is several atomic spacings (the

average distance the adatom travels to find the ordered configuration). In this model, surface order is achieved when $t_s > \tau_s$.

After attachment is a second time span, t_t , during which the adatom exists in a high diffusivity subsurface transition-layer prior to incorporation in the bulk crystal. This transition-layer is in reality a subsurface region of the crystal wherein a gradient of injected vacancies exists, but is modeled as a layer of specific thickness and constant diffusivity. We have $t_t = L_t/R_g$ with L_t the transition-layer thickness. Since CuPt-B order is actually not thermodynamically favored in the bulk, subsurface interdiffusion tends to destroy any surface order. Similar to the surface ordering timescale, we have a transition-layer randomization timescale, $\tau_t = \delta_t^2/D_t$, where D_t is the effective transition-layer diffusivity and has a value intermediate to D_s and bulk diffusivity and δ_s is again several atomic spacings (distance needed to randomize crystal) with $\delta_t \leq \delta_s$. When $t_t < \tau_t$ then the ordered surface is frozen into the bulk crystal. Control of ordering then is presumed based on control of the actual adatom residence times and diffusivity at the growth front.

Increased growth temperature is expected to diminish τ_s and τ_t through increased cation diffusivity, and to increase t_s and t_t . While this effect increases the likelihood of adatoms finding the ordered state upon arrival at the substrate, it is also more likely that the crystal will be subsequently randomized in the subsurface layers. Variation of V/III ratio primarily affects surface diffusivity. With higher V overpressure, surface diffusivity of cation species is suppressed, decreasing t_s . Hence we see that the high temperature and high V/III used in this study supports disordered material. It should also be noted that high growth rate also diminishes t_s and t_t (which may prevent or remove order), but increasing growth rate typically requires increasing group III flow and thus may diminish

V/III depending on reactor limits on total V flow rates. Optimized paths for disordered growth are therefore reactor dependent and will certainly vary widely in success with different reactor configurations.

Thus high growth temperature is preferred for applications where wide band gap is required, but may bring with it other growth restrictions such as limits on QW strain and thickness due to increased undulation.

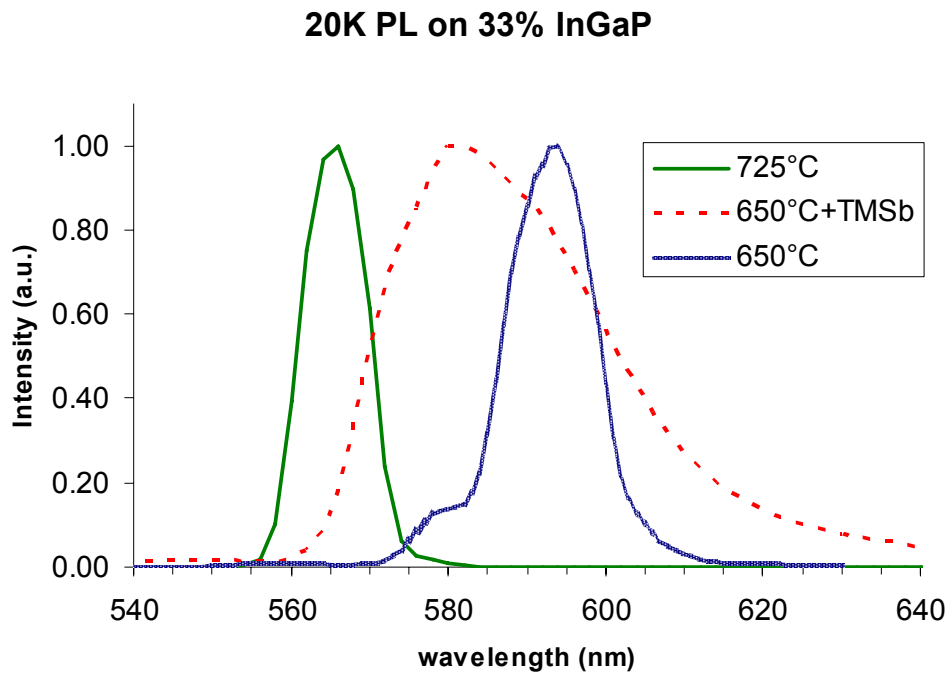


Figure 5.5 20K PL intensity as a function of wavelength for $\text{In}_{0.33}\text{Ga}_{0.67}\text{P}$ grown at 650°C with and without TMSb as surfactant and at 725°C. Note that the high temperature blue-shifted the peak while surfactant broadened the peak, probably because of Sb incorporation. The small shoulder at 580nm on the 650°C sample is probably intensity from ordered domains with less order and higher band gap than other domains in the sample.

We have also shown complete alleviation of ordering through the introduction of a very small amount of TMSb during InGaP growth. Using a Sb/P ratio of about 1.82×10^{-3} , we increased the band gap of InGaP by about 30meV and observed no ordering in TED images. Unfortunately the resulting band gap was still about 45meV less than that

predicted for completely disordered InGaP. Additionally, the PL spectrum was severely broadened, as shown in Figure 5.5. We conclude that Sb was likely incorporated into the crystal at an unexpectedly high rate resulting in a quaternary InGaPSb alloy with Sb/(P+Sb) as high as 2.7% (based on CL emission wavelength). Decreasing the Sb/P ratio may result in a reduction of degree of alloying while also destroying CuPt-B order.

5.4 Phase Separation

Another crystal defect observed in the growth of InGaP on GaAsP is compositional inhomogeneities in InGaP. Kim⁴⁶ coined the term “branch defects” to describe a feature found in TEM images of InGaP graded buffers. These heterostructures experienced onset of branch defects as a function of growth temperature and composition of InGaP. It was found that the defect has variable strength of interaction with dislocations—the stronger the defects are, the greater their ability to block dislocation glide. Quitariano and Fitzgerald recently published results that support the hypothesis that branch defects are actually regions of phase separation⁵⁵. McGill also concluded that these types of defects arise from In-clustering (also known as short-range order) at the growth surface in strained Ga-rich InGaP⁴¹. We show here that short-range order also occurs in unstrained (Al)InGaP films lattice matched to GaAsP. The segregation of indium and gallium to Ga-rich and Ga-poor regions is apparent as streaks of strong contrast in TEM images show throughout this chapter.

Figure 5.6 shows XTEM of In_{0.22}Ga_{0.78}P layers grown on a GaAsP virtual substrate. In this image defects clearly propagate through the thickness of the InGaP. These defects are not conventional (they are not dislocations, stacking faults, antiphase domains, etc.)

but are three dimensional and have associated strain fields (as apparent by their enhanced contrast in the $\langle 022 \rangle$ two-beam TEM diffraction condition). Although they do not appear to interfere with the overall morphology and dislocation structure of the sample their extremely high density dictates that we must understand their impact. Kim, McGill and Quitoriano observed initiation of phase separation defects in strained layers where dislocation propagation and hence relaxation was impeded by these defects. Since the function of the InGaP layers in this study is not strain relaxation but as optical material instead, we are concerned with their effect on radiative recombination. In Figure 5.7 CL intensity is compared in similar structures (In_{0.24}Ga_{0.76}P cladding with thin In_{0.35}Ga_{0.65}P SQW) where phase separation defects have been uncontrolled or prevented. Detected peak intensity of the defective sample is approximately 50× smaller than the defect-free sample.

The consequence of the phase separation defects on optical quality has been previously described for more common alloys. For In_{0.5}Ga_{0.5}P, wave-function calculations suggest that the conduction band minimum will localize on Ga₄ clusters, producing an impurity-like trap level in the energy gap⁷¹. This disrupts efficient radiative recombination translating to diode leakage currents in optical devices. Thus we can see that it is essential that phase separation be prevented for successful fabrication of optical devices.

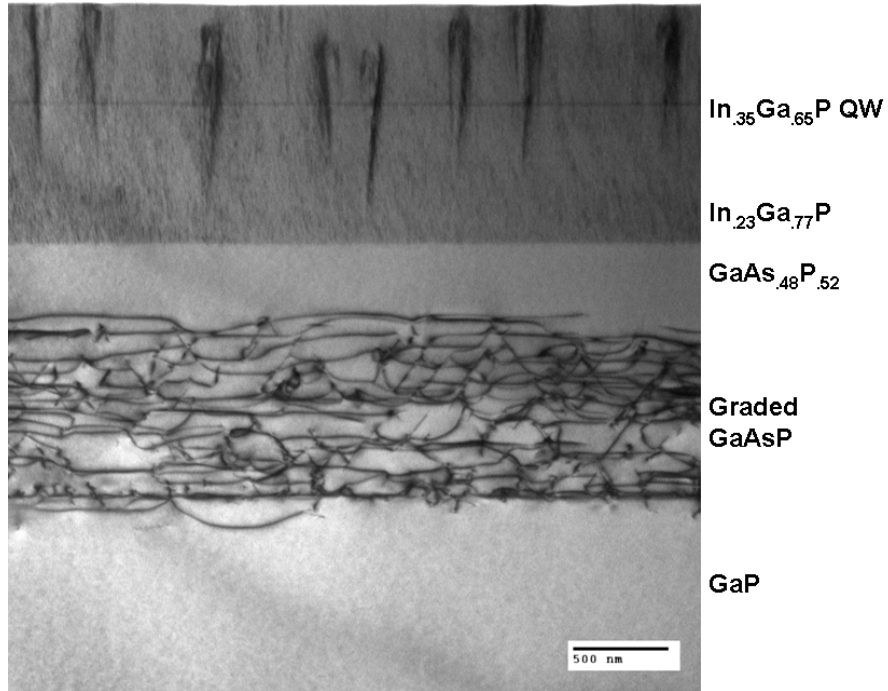


Figure 5.6 Cross section $\langle 022 \rangle$ bright field TEM of $\text{In}_{0.22}\text{Ga}_{0.78}\text{P}$ heterostructure on lattice-matched $\text{GaAs}_{0.46}\text{P}_{0.54}$ graded buffer on GaP. Dark streaks of contrast in the InGaP are short-range order defects and degrade the optical quality of the heterostructure.

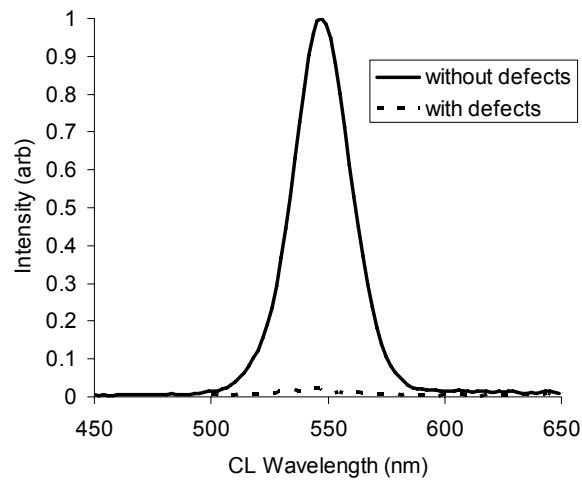


Figure 5.7 Comparison of CL intensity of similar heterostructures where phase separation defects are uncontrolled (dashed line, sample shown in Figure 5.6) and have been removed (solid line).

Several observations of the defects are consistent with the hypothesis that they are in fact phase separation. First, the defects do not exhibit an explicit starting point

common to all defects in the film (such as a single interface where contamination or heterogeneous particles like As-P clusters where they might be nucleated). In fact the initiating points of the various defects are scattered at various depths inside the InGaP film and do not correlate to any visible crystal defect such as dislocations, precipitates, anti-phase domains or stacking faults. Additionally the defects seem to be completely missing from the first 100-200 nm of InGaP grown. This indicates that there is some incubation time required for the defects to develop at the growth surface. These observations are consistent with phase separation: such defects are not nucleated at broken bonds but rather require a local accumulation of In or Ga.

Second, the shape of the defects also indicates that the phenomenon is surface-driven. Judging from the cross section TEM, once established in the growing film, the defective region grows in strength (of strain contrast) and area with the thickness of the film. The effect is self-propagating and typically (but not always) lasts for the entire remaining thickness of the film. Again this is consistent with phase separation: local coherent strain is reduced by continued segregation such that the composition of the growing film inside a defect is different from that away from the defect. Thus local lattice constant in the strain contrast region is different than that of neighboring areas.

Quitoriano argued that elastic considerations possibly as well as the non-equilibrium nature of the MOCVD growth surface must account for the presence of phase instability well outside of the calculated miscibility gaps of InGaP. It was argued that the strain undulations at the surface which lead to crosshatch also lead to the phase separation phenomenon. In this study, the defective InGaP layers are lattice matched to the underlying virtual substrate and are therefore nominally unstrained. Despite this, the

InGaP layers are crosshatched because of the underlying graded buffer, but this crosshatch is fundamentally different—it consists of simple local height differences on the wafer rather than strain undulations. Hence these defects must not originate at strain undulations as Quitoriano observed; we glean from this that the driving force for separation in this case must be a manifestation of the nonequilibrium MOCVD growth surface. We must also believe then that the phenomenon is reaction-condition specific and not a general effect expected in all MOCVD grown InGaP. Indeed this observation holds as we were able to optimize growth conditions to prevent the defects.

To summarize, slight thermodynamic and/or kinetic instabilities at the InGaP growth front cause a slight preference for In segregation to and from locally In-rich and In-deficient regions which are subsequently frozen into the film. Many mechanisms for the initiation of short-range order have been proposed in the literature, but much remains to be understood. For the purposes of this microstructural study we have focused on learning how to remove these defects.

By applying the Kurtz et al. model on long-range ordering to short-range, we are able to derive design rules which prevent phase separation. Like atomic ordering, phase separation initiates at the growth surface but is thermodynamically unfavorable in bulk InGaP at our growth temperature, so a similar competitive-process model can be applied. Again we are interested in adjusting growth parameters that increase intermixing at the growth front thus preventing self-organization of the adatoms into either short- or long-range ordered configurations. We experimentally tested the parameters of growth temperature, V/III, growth rate and use of surfactant to determine conditions under which short-range order could be avoided.

We have previously concluded that increases in growth temperature increase surface and transition-layer diffusivity such that, despite the increased probability for adatoms to arrange in an ordered manner, the lattice is better randomized in the subsurface layer. Again we expect that increasing growth temperature will increase the likelihood of originating the branch defect but, since the length scale of the effect is quite different, τ_t is now much longer than in the ordering case. To randomize CuPt-B order, a cation needs to move a short distance (δ_s is on the order of a couple of $\{111\}$ spacings at most) but to randomize the branch defect, much larger diffusion distances are needed (δ_t is now $\sim 100\text{nm}$). Since τ_t depends on δ_t^2 , the difference in δ_t dictates that randomization in the transition-layer would be very difficult and require very long residence times (100-1,000 times longer). Contrarily, the surface mobility of adatoms is great enough that δ_s is not prohibitively large to create the defects. In fact, surface diffusion lengths much larger than δ_s , of $1\mu\text{m}$ are reported³⁶. From this we see that avoiding branch defects requires suppression of their formation at the surface.

In Figure 5.8a) we show InGaP grown at 725°C with a ten-minute *in-situ* growth break. Here, defects are observed from the annealed interface indicating that the *in-situ* anneal afforded extra time for arrangement of the short-range order which subsequently propagated and was frozen into the bulk with continued growth. As predicted, solid-state diffusion was not sufficient to randomize the defects. Figure 5.6 and Figure 5.8b) are a direct comparison of growth temperature with no *in-situ* anneal. Again we observe, as predicted, greater incidence of the branch defects at higher growth temperatures (Figure 5.6) when controlling other factors. Since we cannot reasonably increase growth temperature before entering a thermodynamically limited regime (where growth rate

drops exponentially) we can see that subsurface diffusivity is not sufficient to randomize branch defects. Hence we must focus instead on preventing defect formation at the surface while also preventing formation of CuPt-B order.

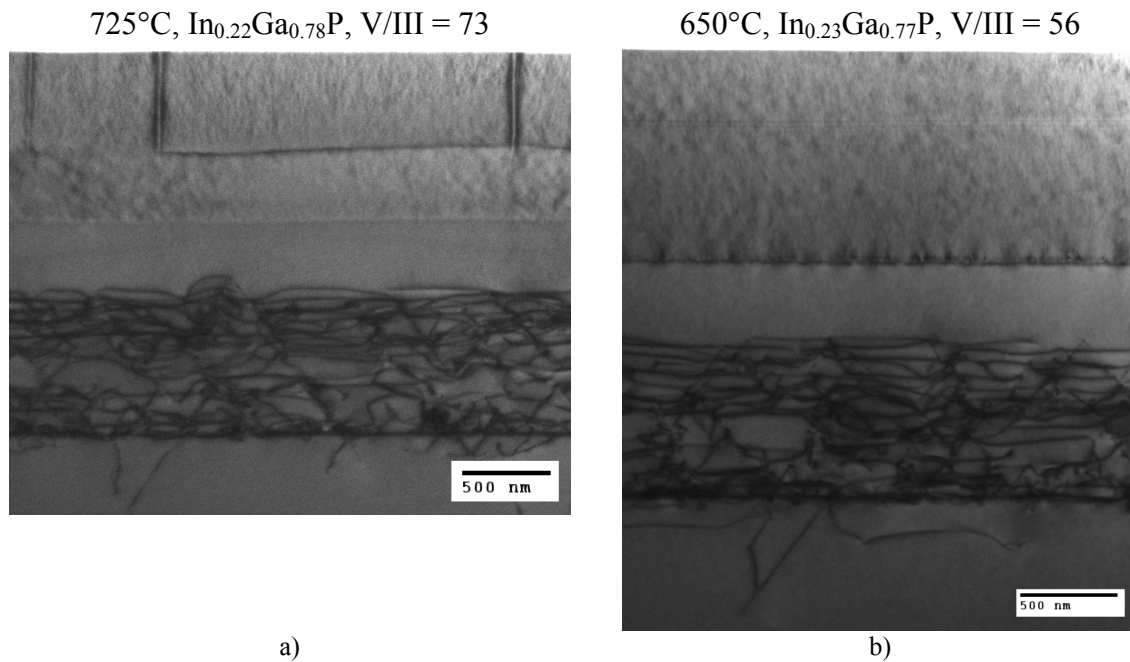


Figure 5.8 Comparison of similar structures grown at 725°C and 650°C. The sample in a) contains phase separation defects which begin at an interface where growth was halted for a ten-minute *in-situ* anneal. In b), 650°C growth did not result in separation defects. Figure 5.6 shows a sample at identical composition grown entirely at 725°C with no *in-situ* anneal.

The primary effect of V/III on the Kurtz parameters is also clear: high V/III suppresses surface diffusivity and residence time at the surface. The effect of V/III on the transition-layer is less apparent, but we hypothesize that very high or low V/III injects a greater number of point defects thus thickening the sublayer and increasing diffusivity in it. High point defect densities are deleterious to luminescence and should be avoided. But, if surface order can be avoided, then subsurface randomization need not be considered. The predominant surface impact of high V/III assures that short-range order

is never achieved and will prevent branch defects. In practice this is exactly what we observe, as shown for two compositions of InGaP in Figure 5.9 and Figure 5.10.

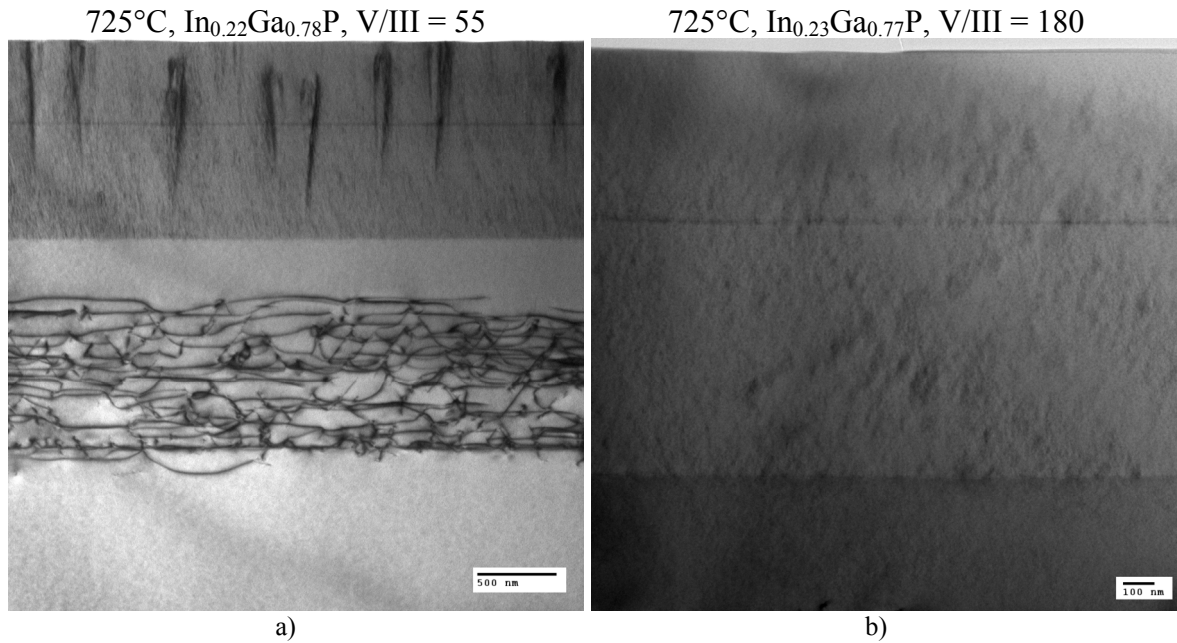


Figure 5.9 Comparison of InGaP grown at 725°C under a) high and b) low V/III. Suppression of surface diffusivity at high V/III prevents the formation of short-range order.

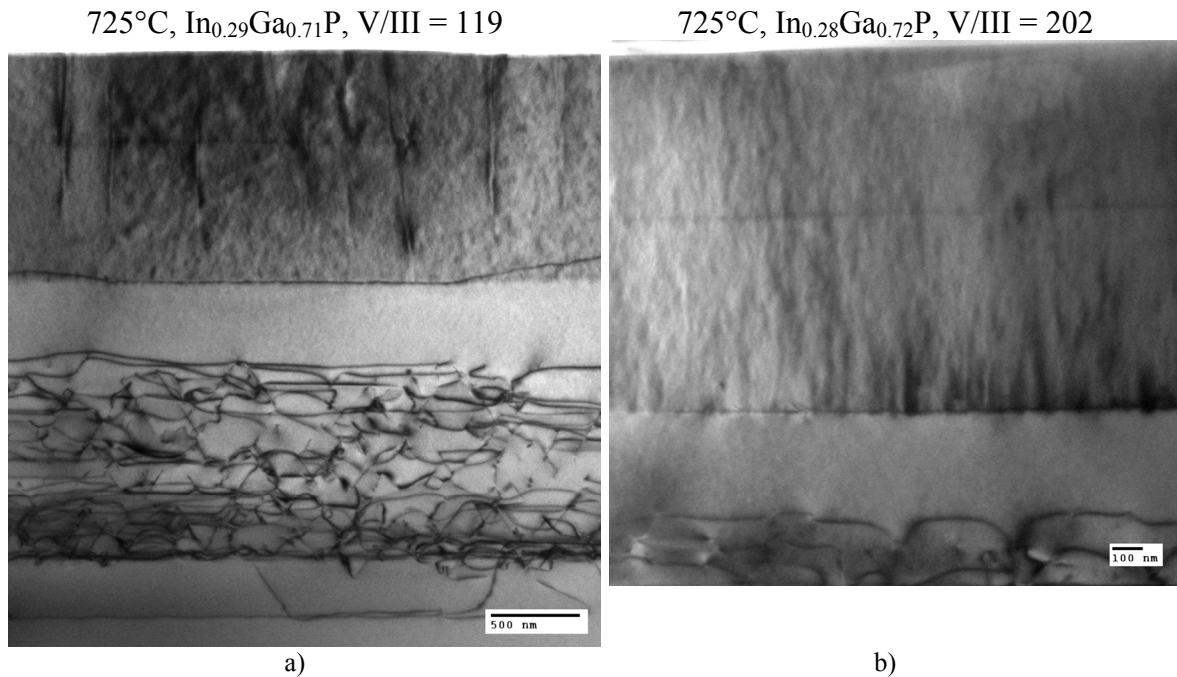


Figure 5.10 Comparison of V/III effect on defects in InGaP at higher In fraction (compared to Figure 5.9), where the alloy is more susceptible to phase separation defects. Note the higher V/III ratios as well as the contrast near the InGaP/GaAsP interface in b) which suggests minor phase separation defects despite the high V/III.

Note that at higher In fraction (Figure 5.10), much higher V/III ratios are required (compare to Figure 5.9) to prevent phase separation. This suggests that the presence of additional In at the surface increases the probability of developing the defect. This is in agreement with our supposition that phase separation is responsible for the defects.

Finally, using a small mass flow of TMSb, we investigated the impact of surfactant-mediated growth the formation of short-range order. Like high V/III ratio, we expect the effect of a surfactant to be largely confined to the surface and again to suppress the surface diffusivity required to initially obtain order. This is also confirmed, as shown in Figure 5.11.

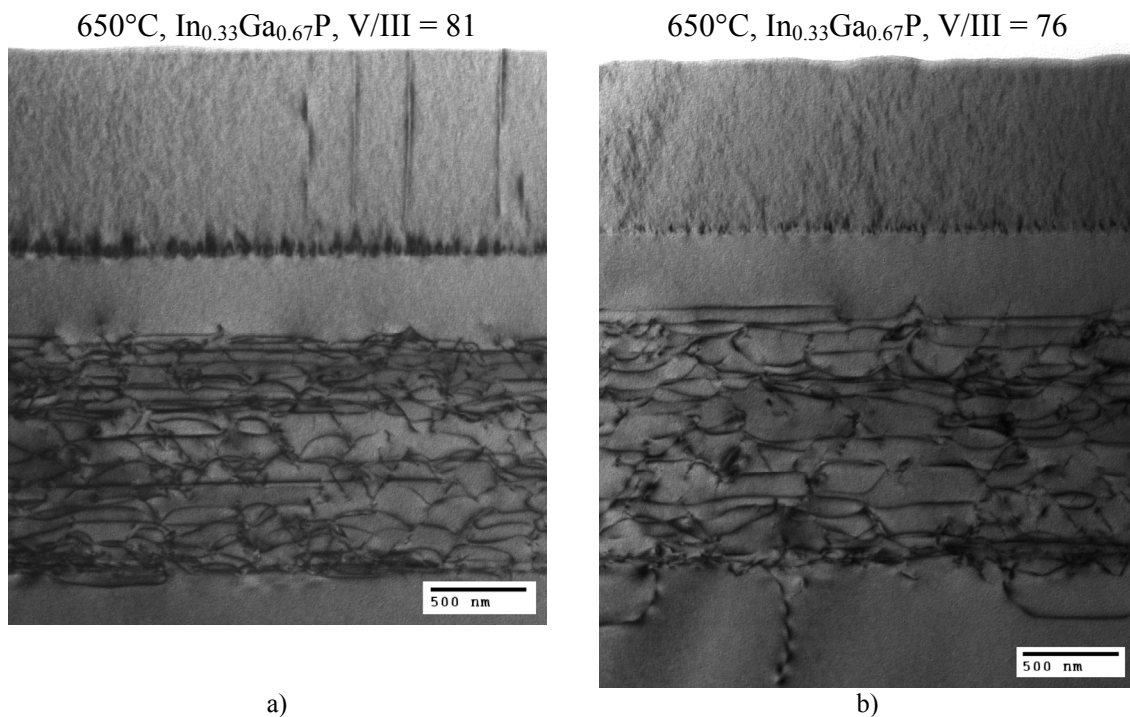


Figure 5.11 Comparison of InGaP grown under identical conditions a) without and b) with a small flow of TMSb.

Interestingly, we found that small changes in composition of InGaP had dramatic effect on the presence of phase separation defects. By increasing the In fraction in InGaP from 0.23 to only 0.33 under nominally equal conditions we observe nucleation of branch

defects. Figure 5.8b) shows $\text{In}_{0.23}\text{Ga}_{0.77}\text{P}$ with no phase separation defects and Figure 5.11a) shows $\text{In}_{0.33}\text{Ga}_{0.67}\text{P}$ with the defects. This strong sensitivity is likely due to the swiftly changing nature of InGaP over this composition range which is also evidenced by the solidus temperature of InGaP (see Figure 5.12). Most of the decrease in solidus temperature of InGaP occurs as the In fraction increases from 0 to 0.3; beyond this we might expect InGaP to behave more InP-like and less GaP-like.

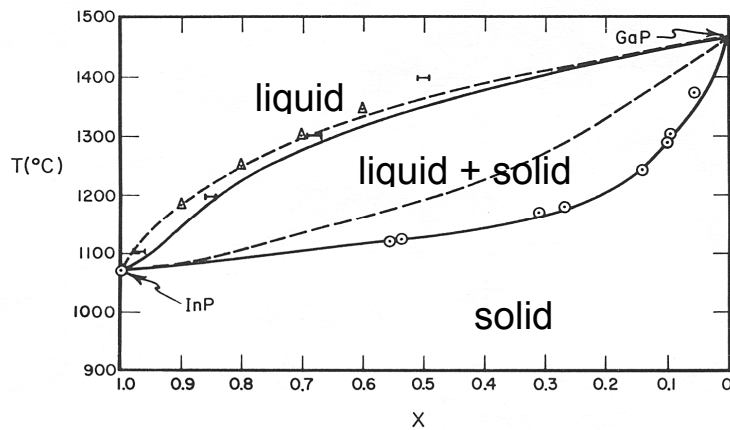


Figure 5.12 Phase diagram of InGaP, indicating the sensitivity of the InGaP solid to composition at In-fractions less than about 0.3. The melting point (solidus) of InGaP reveals much about the chemical nature of the alloy. Reproduced from Stringfellow³⁶.

It should be noted that another excellent growth parameter that ought to offer good control over short and long-range order defects is growth rate. By varying the rate at which adatoms must be incorporated into the bulk film we can manipulate their diffusion lifetimes at the surface and in the transition-layer. While this parameter is expected to behave similarly as those tested above it is often less convenient in a production setting as intentional low growth rates slow production and high growth rates can make high V/III ratios difficult to practically attain. Despite this we summarize our results as a function of V/III, growth rate, growth temperature and composition in Figure 5.13. It is immediately clear that in our reaction phase space we must either tolerate low

temperature growth (and hence CuPt-B order) or always maintain high V/III ratio at reasonable growth rate (upper right portion of Figure 5.13).

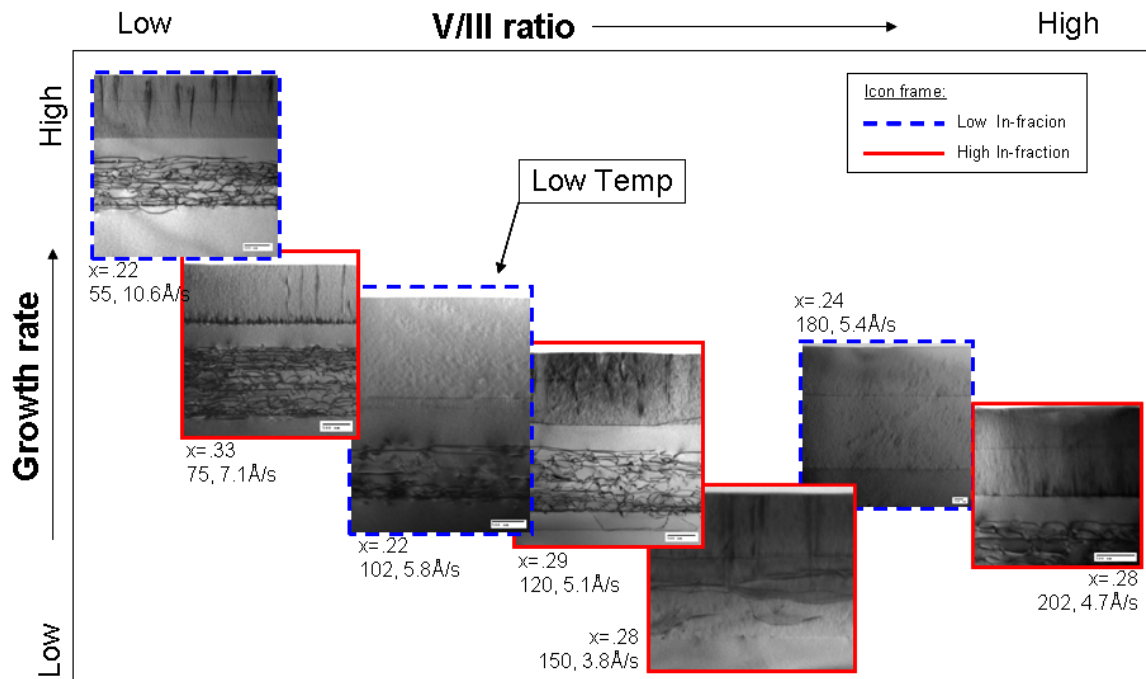


Figure 5.13 Phase space for formation of short-range order defects. Reactor limitations prevent growth in the upper right quadrant of the plot, the region where we expect the highest quality material. By maintaining high V/III and reasonable growth rates ($\sim 5 \text{ \AA/s}$) we can avoid short-range order in our system.

5.5 GaAsP/InGaP Interface

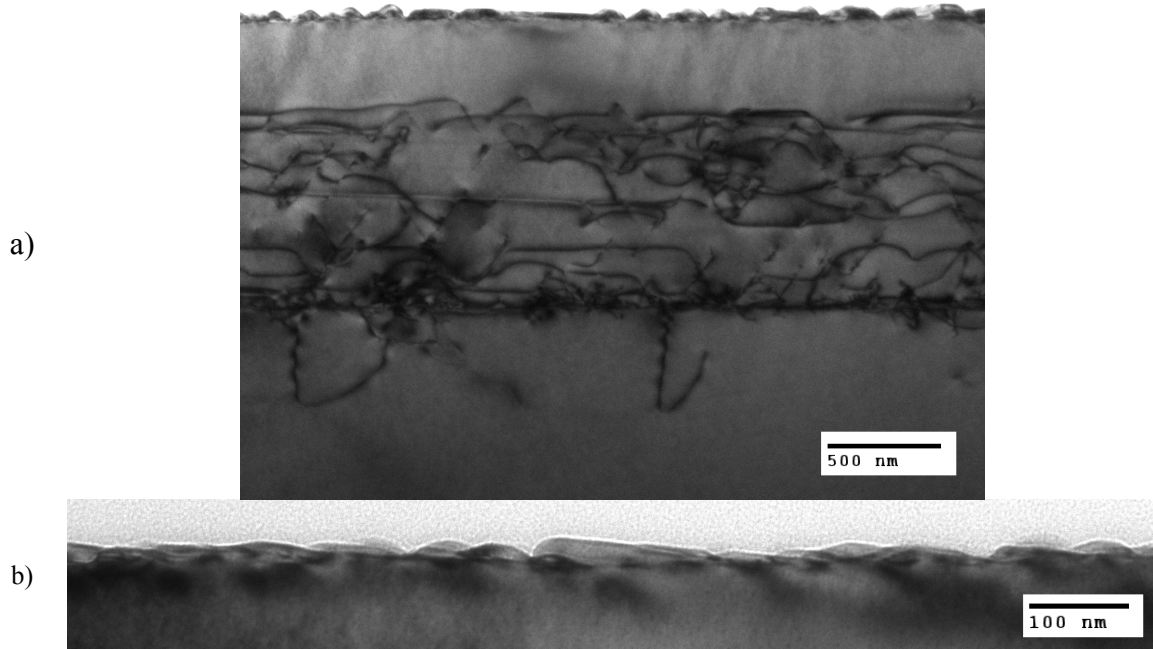


Figure 5.14 Cross section $\langle 022 \rangle$ bright field TEM of a) unprotected GaAsP compressive graded buffer. During the post-growth cool down, a fixed ratio of AsH_3 and PH_3 gas was flowed, resulting in undulation of the surface, as shown in b).

The final aspect of microstructural control we present here is the control of the GaAsP virtual substrate surface. We observed that undulation of the GaAsP surface occurs during temperature ramps when the group V overpressure is not carefully controlled. Figure 5.14 shows cross section TEM of a graded composition GaAsP virtual substrate which was cooled under fixed partial pressures of AsH_3 and PH_3 . As is apparent from AFM and PVTEM of a sample cooled under AsH_3 only (in Figure 5.16), the surface layers were depleted of P to such a degree that severe islanding occurred, and in fact the strain buildup from the compositional change in GaAsP was sufficient to nucleate misfit dislocations underneath the islands. From the PVTEM it is apparent the misfit dislocations (aligned to the substrate $\langle 100 \rangle$) terminate at the edge of the islands. With

subsequent growth of InGaP on the islanded substrate, these dislocations turn vertical and extend through the cap to the crystal surface as shown in Figure 5.15. Use of pre-grown substrates in subsequent runs or deposition of heterostructures at growth temperatures different than that of the virtual substrate are just two examples where stability will be an issue. We present here the atomic mechanism for this defect and solutions to prevent it.

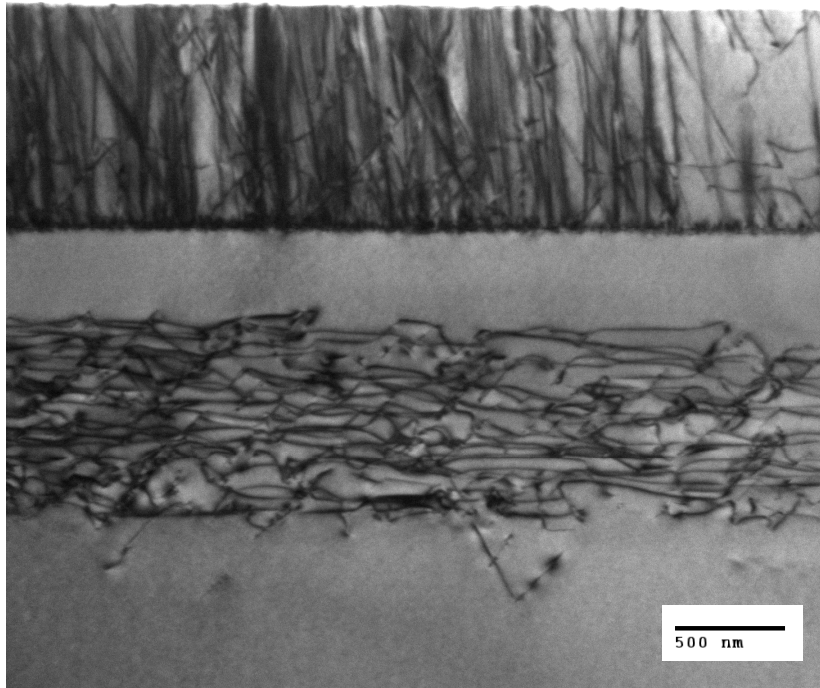


Figure 5.15 Growth of InGaP on top of undulated or islanded GaAsP results in highly defective growth unsuitable for optical device fabrication.

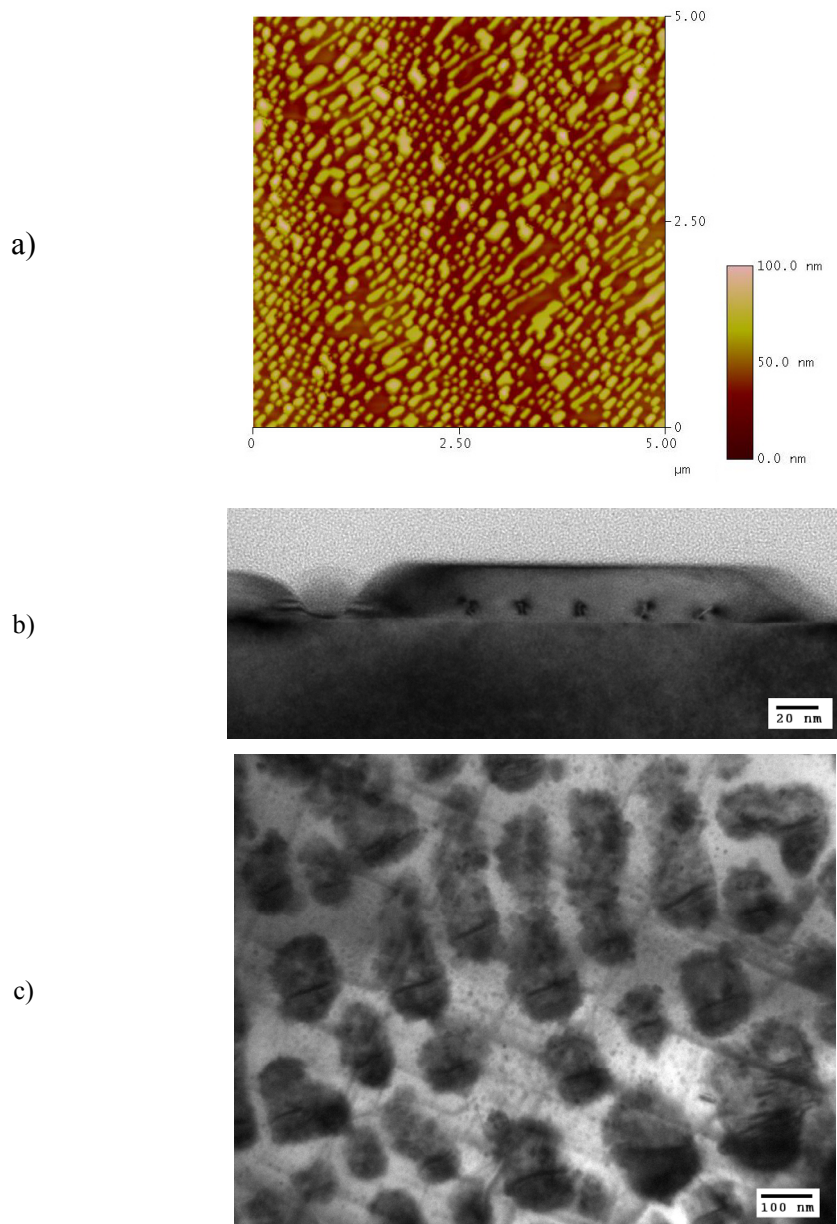


Figure 5.16 Three images of a GaAsP film capped with incomplete 25Å GaAs film and cooled under AsH₃ overpressure. In a), the AFM surface height profile shows the distribution and shape of the As-rich GaAsP islands. In b), cross section TEM shows the formation of misfit dislocations underneath the islands which are also visible in c) plan view TEM of the same sample.

In III-V materials, the group V species exhibit large vapor pressures at elevated temperature (>450°C). By providing group V overpressure during high-temperature

anneals and high V/III ratios during growth, desorption and creation of vacancies is avoided. This overpressure simply provides an oversaturation of anions at the surface (several monolayers worth) such that the V species desorption rate is countered by an equal V incorporation rate. But, for a mixed anion alloy, the relative overpressure of the V species must also be taken into account. When flowing AsH_3 and PH_3 at high temperature over a GaAsP surface, there are several mixed As-P monolayers at the crystal surface and their composition (As/P ratio) is dependent on the pyrolysis rates of AsH_3 and PH_3 over the wafer. Since there is a high rate of exchange of anions between the solid and the overlayer, the bulk crystal effectively “sees” and the gas composition of As and P. So even if no growth is taking place, the composition at the surface of a mixed anion alloy is a function of the As/P ratio in the gas phase over the wafer.

This situation is additionally complicated by the disparate pyrolysis rates of group V precursors. Generally, PH_3 molecules crack at higher temperatures than AsH_3 , but catalysis effects of the wafer (which may be compositionally dependent) and the chemical makeup of the MOCVD carrier gas (H_2 provides H radicals which aid decomposition of the precursors) further complicate the temperature dependence of the relative pyrolysis rates of the V precursors. Thus even if a set AsH_3/PH_3 ratio is maintained over GaAsP layers, as reactor temperature is varied relative cracking rates of the precursors varies and the composition of the AsP overlayer and therefore surface layers of GaAsP also vary. Due to the complexity of the situation, it is difficult to predict or even experimentally predetermine the reactor parameters (PH_3/AsH_3 injection ratio) as a function of reactor temperature which would be required to maintain a constant GaAsP composition in an exposed GaAsP layer.

In order to prevent surface undulation and dislocation formation, the GaAsP surface must be passivated such that mixed anion material is not exposed during temperature changes. As shown in Figure 5.17, use of a relatively thick (0.2 μm) layer of lattice matched InGaP served to isolate the underlying GaAsP such that cool down under PH_3 did not undulate the surface. In this case the interface is highly perfect and any subsequent layer of InGaP is not compromised.

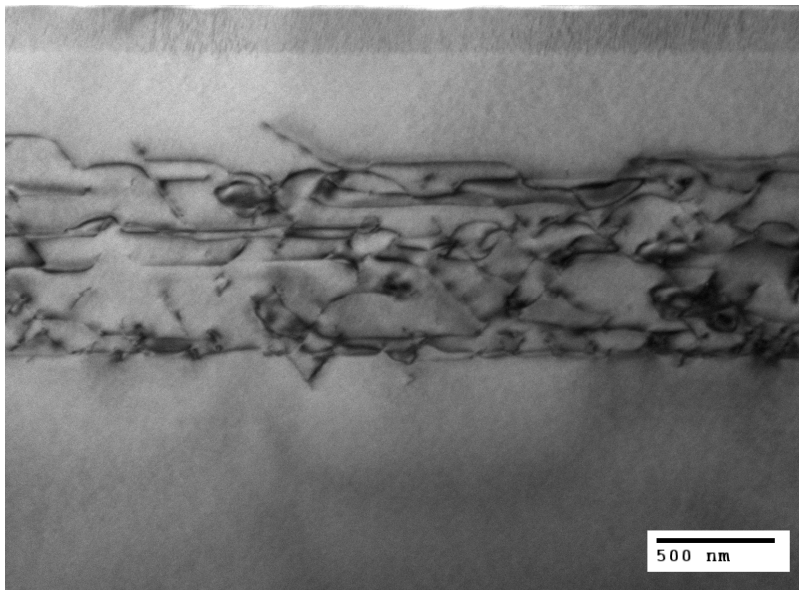


Figure 5.17 Compressive GaAsP buffer graded to final composition of $\text{GaAs}_{0.45}\text{P}_{0.55}$ with high quality lattice-matched $\text{In}_{0.22}\text{Ga}_{0.78}\text{P}$ cap.

We were able to further improve this stabilization scheme through the use of a very thin strained GaAs passivation layer. Just 25 \AA of compressive GaAs on GaAsP proved sufficient to stabilize GaAsP. Figure 5.18 shows an InGaP heterostructure which was grown in a separate growth run from the underlying GaAsP tensile graded buffer. As can be seen from the high resolution XTEM, the interface is quite flat and highly perfect despite the temperature fluctuations required of post-growth cool down and pre-growth

temperature ramp and anneal. This solution was consistently reliable for all tensile relaxed GaAsP graded buffers that we deposited.

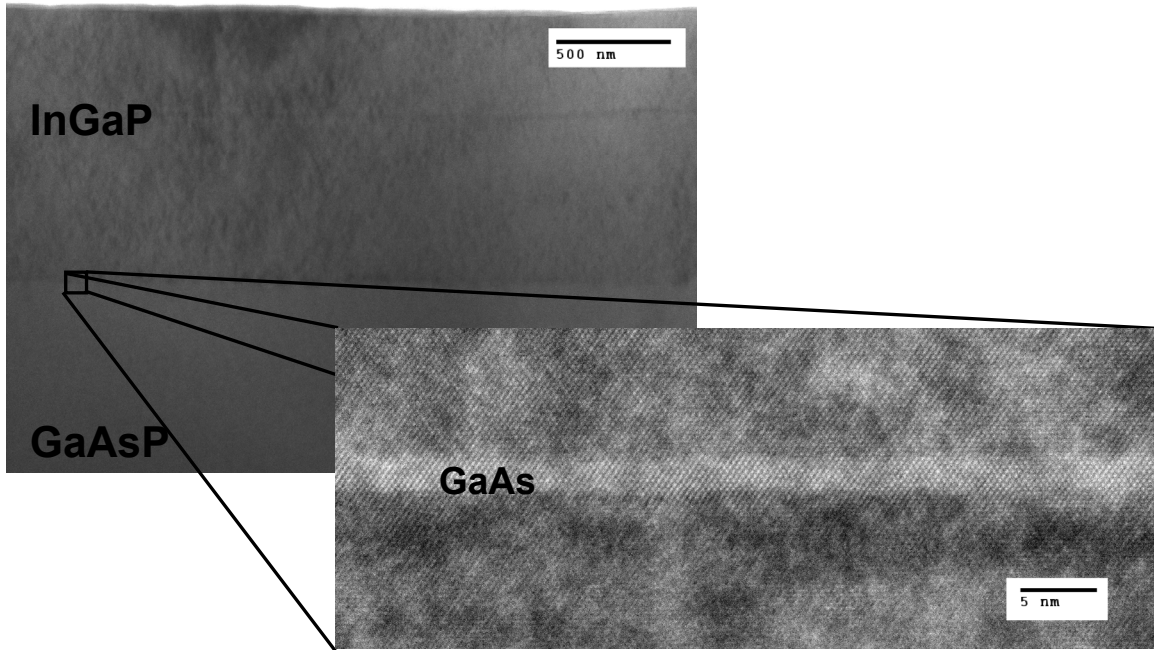


Figure 5.18 High resolution TEM of a compressively strained 25Å GaAs protective layer on a GaAsP graded buffer. This thin barrier allows the growth of high quality InGaP heterostructures lattice-matched to GaAsP virtual substrates.

The successful use of such a thin passivating layer sheds light on the nature of the subsurface transition-layer during GaAsP growth and annealing. In this case the diffusion of P atoms across just 25Å (8 atomic layers) is entirely repressed as long as the passivating layer is grown directly after GaAsP growth and without a growth break. This evidence suggests that the transition-layer described above is quite thin (<25Å)—otherwise transition-layer interdiffusion would inject P atoms into the GaAs layer leading to subsequent P leakage and surface undulation under cool down. But if the transition-layer is truly less than 25Å thick, how can such severe undulation (250Å amplitude) occur during cool down under an uncontrolled atmosphere? The answer to this lies in the injection of point defects at high temperature and their effect on the transition-layer

thickness. Under normal growth conditions vacancy density must be relatively low (few vacancies lead to a thin transition-layer), but without a passivating layer, then uncompensated V species at the surface leak to the vapor, introducing vacancies. Hence, despite the presence of a high V overpressure (of the wrong composition) vacancy populations will be high. These defects diffuse downwards and thicken the subsurface layer further exacerbating the problem. Hence we can conclude that the thickness of the subsurface layer increases by as much as an order of magnitude in the relatively small amount of time required to cool from 725°C to frozen conditions near ambient where solid-state diffusion is negligible.

Finally, we note that while 25Å of compressively strained GaAs successfully stabilized tensile relaxed GaAsP buffer, it was *not* successful on compressive relaxed GaAsP graded buffers at similar ultimate compositions. We believe that this is most likely due differences in vacancy populations during growth. Comparing GaAs and GaP growth, given the relatively lower pyrolysis rate of PH₃ compared to AsH₃ for the same injected V/III ratio, the GaP growth surface has a lower P adatom population than that of As on GaAs. This corresponds to greater vacancy populations on the GaP platform and thicker transition-layers. Compressive graded GaAsP (on GaP) suffered from higher residual vacancy populations such that a relatively thick (and therefore lattice matched) passivation layer was required. Perhaps very high V/III ratios during P-rich GaAsP graded growth might suppress this effect. An alternate explanation for the higher vacancy population on compressive graded buffers could be that the sense of strain relaxation is responsible. In this argument, compressive layers must have inherently higher V-vacancy populations than tensile.

5.6 Conclusions

AlInGaP at lattice constants less than that of GaAs is technologically important for state of the art solid-state light emitters. With potential applications in visible lasers, high efficiency green emission and monolithic integration with Si, we set out to understand its electronic properties. To lay the foundation for future work, we have studied and presented here methods to achieve a high degree of control over MOCVD-grown InGaP. We have extended a simple two-step adatom incorporation model (already used in regards to GaAs-matched InGaP) to explain control of CuPt-B atomic ordering, and also to describe short-range order in InGaP and the stability of mixed anion virtual substrates. Although it is difficult to avoid surface ordering of InGaP, high growth temperature serves to randomize the crystal, removing the effect of CuPt-B order on the band gap. Suppression of surface diffusivity through high V/III also discourages the formation of short-range order defects in InGaP. Lastly, injection of large vacancy populations in GaAsP destabilizes the GaAsP surface making surfaces unsuitable for epitaxy. Together, this exceptional control and understanding of these fundamental aspects of novel InGaP alloy thin films will aid in the realization of novel yellow, orange and possibly green solid-state LEDs and lasers.

Chapter 6 Device Fabrication

6.1 Introduction

Up to this point we have presented background and original research supporting the fabrication of green light emitting devices. In this chapter we present the culmination of this work, the fabrication and demonstration of several devices.

III-V materials systems for high-brightness light emitting diodes (HBLEDs) and laser diodes (LDs) in the blue and red regions of the visible spectrum are well established; however materials for green emission lag behind in performance. For applications such as red-green-blue mixed display, projection or lighting, an efficient and bright green source is needed. Despite technological advances in group III-nitride materials systems, much is still desired; the incorporation of large fractions of In necessary to push InGaN-based devices from blue into the green spectrum has proven deleterious to material quality and device performance. The lack of low-cost, high quality or large area substrates at green-InGaN lattice constants hinders this approach. Similarly, AlInGaP, a common red to yellow-green light emitting material, has been traditionally limited to use at the GaAs lattice constant Figure 6.1. Here, the increase of Al fraction in the active region (or the value of y in $\text{In}_x(\text{Al}_y\text{Ga}_{1-y})_{1-x}\text{P}$), extends emission towards green from the red end of the visible spectrum, but electrical and optical confinement decreases with corresponding decrease in efficiency and brightness.

Because of its large band gap (up to 2.5eV), AlInGaP that is not constrained to the GaAs lattice constant still offers untapped promise for a superior green emitting devices. GaAs-matched AlInGaP reaches only 2.3eV and the widest direct band gap material has relatively high Al content (near $y=0.5$), making devices susceptible to performance degradation from O-related defects⁷². More attractive alloys of AlInGaP exist at smaller

lattice constants where the direct band gap is wider, even with no Al, and the indirect band gap is much larger.

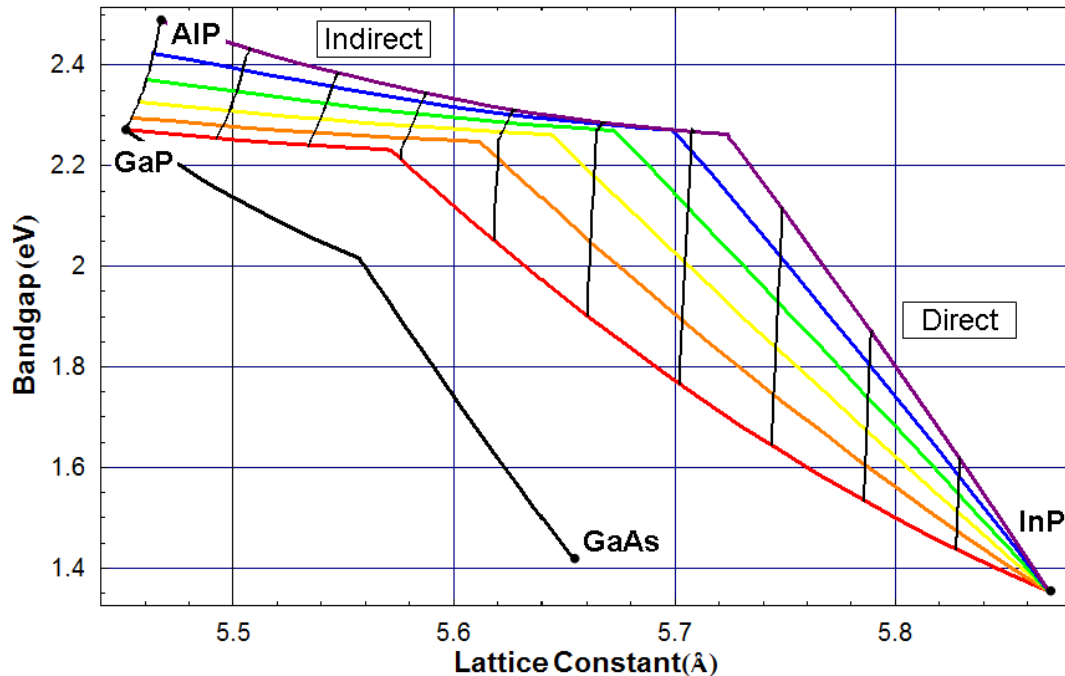


Figure 6.1 Band gap as a function of lattice constant for several material systems. AlInGaP offers wide band gap as well as a lattice constant amenable to integration on Si and Ge.

At AlInGaP compositions near the direct band gap maximum (at the direct-indirect crossover), the proximity of the X (indirect) and Γ (direct) conduction band valleys enables carrier leakage from the Γ to the X band. To design AlInGaP devices with the shortest possible wavelength, the material must be close to a direct-indirect crossover, regardless of its lattice constant. By implementing a QW design we hope to counteract the negative influence on the internal quantum efficiency of the device. While releasing the lattice constant constraint does not also release this crossover constraint, it does allow us to choose a device composition where the crossover is at a higher energy, and where there is greater electrical and optical confinement provided by the higher band gap and index contrast of higher Al-fraction materials at similar lattice constants. This along with

overall lowered Al-fraction (and O-defects) will significantly improve efficiency and enable LDs with record low wavelength. We have already developed technology to break the lattice match constraint. Using thin (1-4 μm) GaAsP compositionally graded buffers we have access to any lattice constant between GaP and GaAs without significant degradation of material quality (the ultimate threading dislocation densities are as low as 10^4cm^{-2} for GaAs_{0.5}P_{0.5}). We have also successfully investigated the growth of high quality virtual substrate-matched InGaP (with In fractions ranging from 0.18 to 0.44) that is free from the detrimental effects of CuPt-B atomic ordering or phase separation defects.

Using this platform we have successfully fabricated light emitting diodes which we present and discuss here. Our previously published results³⁰ investigated similar structures. We have been able to improve upon the previous results through higher quality virtual substrates and better microstructural control in AlInGaP.

6.2 Device Modeling

Figure 6.2 is a schematic representation of our proposed device structure. In it, a wide band gap, indirect cladding is used in conjunction with a lattice-matched separate confinement heterostructure (SCH) and strained quantum well (SQW). The entire structure is capped with a thin, lattice matched InGaP layer to protect the Al-containing material from oxidization in ambient.

It should be noted that, unlike McGill's AlInGaP virtual substrate, even a thin GaAsP graded layer on transparent GaP will significantly absorb emitted photons. For application as an edge emitting laser, substrate transparency is not required. Instead the

higher quality of the GaAsP virtual substrate is expected to increase the performance of a laser diode (with a lower threshold density, for example). But, for high photon extraction efficiency (external quantum efficiency) such as that desired in an LED, a transparent substrate is a plus and in fact in high volume production, GaAs substrates are regularly removed from epitaxial devices and replaced with GaP in a wafer bonding process⁷³⁻⁷⁵. An AlAsP graded layer which is fully transparent is theoretically possible for this application, but difficulties in growing high Al-fraction material might become a factor, in fact no previous reports of AlAsP growth could be found.

Extending the model we presented in³⁰, we used the normalized infinite quantum well approximation for confined levels⁴² to estimate the emission wavelength and confinement available for various thicknesses of quantum well up to the estimated experimentally achievable critical thickness⁷⁶ with quantum well composition as a parameter. This model calculates the position of energy states in a strained AlInGaP QW sandwiched in an unstrained AlInGaP barrier layer.

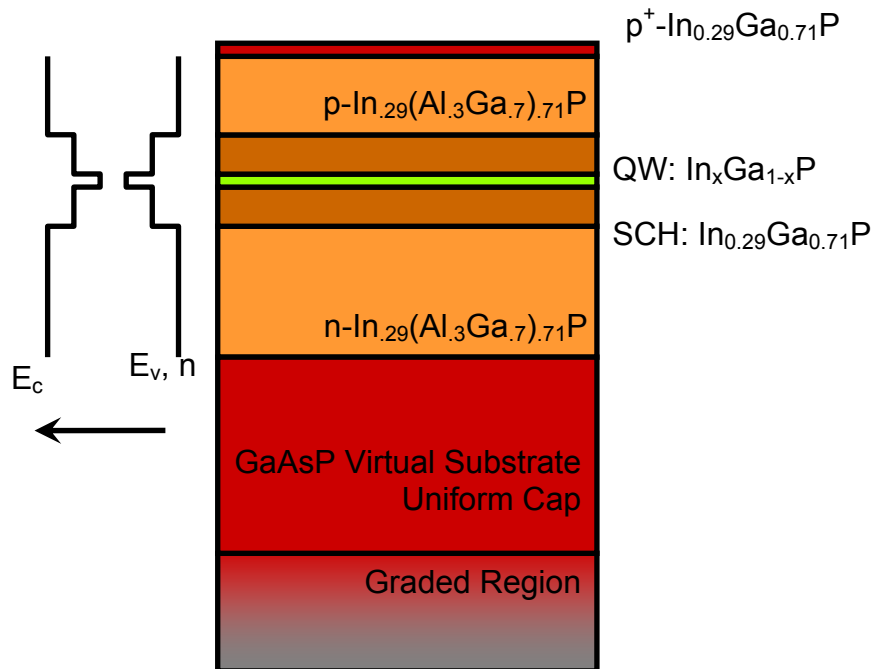


Figure 6.2 Schematic of an example light emitting structure. The virtual substrate can be adapted for any AlInGaP composition required up to the GaAs lattice constant. A lattice-matched SCH and strained QW provide optical and electrical confinement.

We found that, as predicted, our device design will be limited at short wavelengths by the available confinement. An example calculation result is shown in Figure 6.3. As the quantum well is thinned, confinement pushes carrier energy levels higher, making a higher energy transition possible, but at the same time this brings the energy levels closer to the top of the well, reducing confinement. As strain is increased for a given substrate composition (by increasing In fraction in the quantum well), the dominant effect is that the lower band gap material shrinks the energy transition. From the model, we see that our strategy for decreasing emission wavelength must be to optimize the tradeoff between confinement and wavelength.

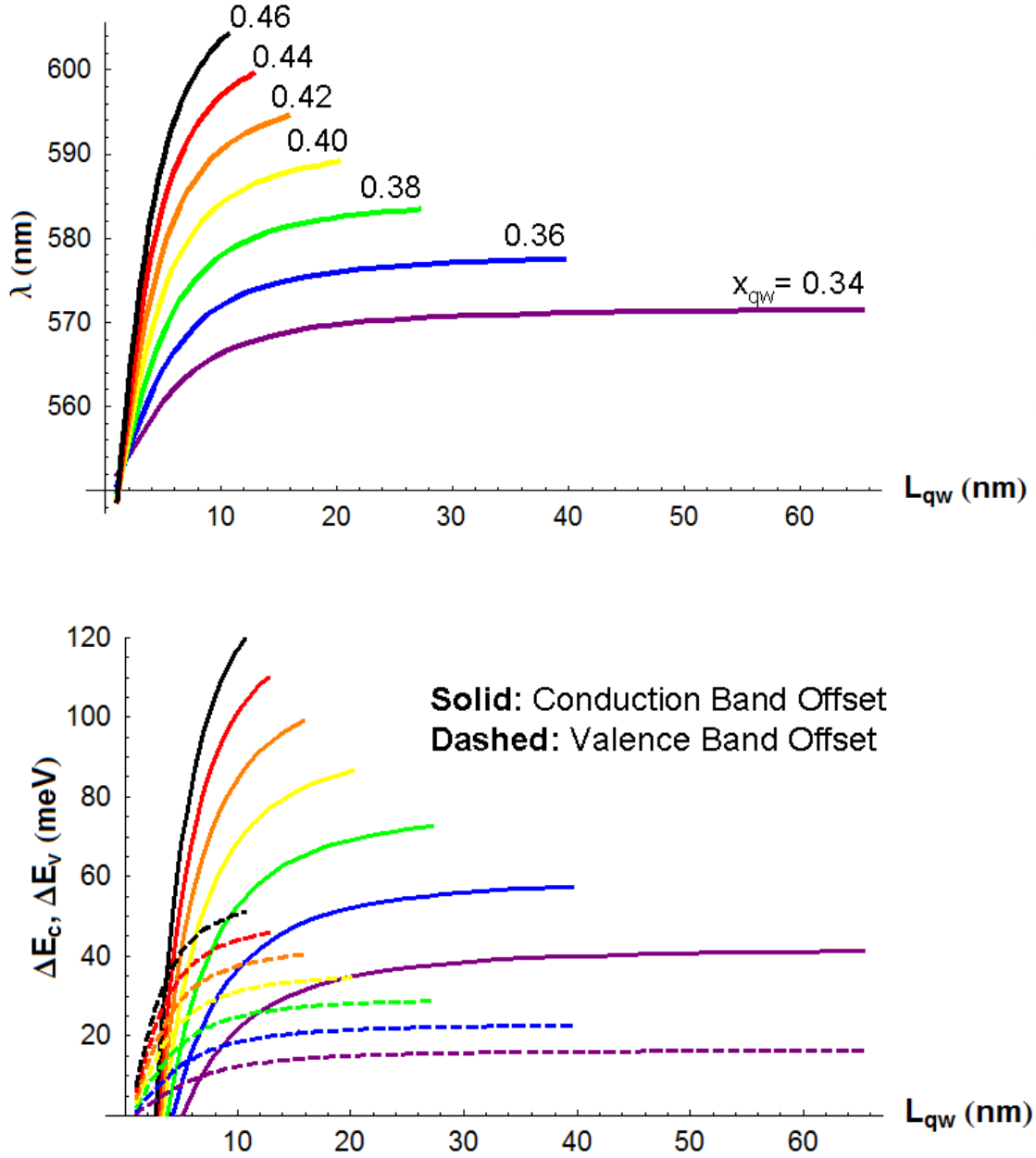


Figure 6.3 Some example results of the computer model. Here we have specified that the cladding material, $\text{In}_{.29}\text{Ga}_{.71}\text{P}$, is lattice matched to the substrate and that the thickness and composition of the $\text{In}_x\text{Ga}_{1-x}\text{P}$ QW is varied.

We expect that $\text{AlInGaP}/\text{InGaP}/\varepsilon\text{-InGaP}$ strained quantum well devices with light emission in the range 550nm to 620nm can be realized, but that a lack of a sufficient conduction band offset will limit devices at shorter wavelengths. The conduction band

edge of AlInGaP is predicted to be low due to the type-II valence band offset between AlP and GaP. In fact, at compositions where the direct band gap of InGaP is the largest available, the addition of Al increases the band gap but also decreases the height of the conduction band edge thus limiting available conduction band offset, as shown in Figure 6.4^{7, 77}. Since the material and electrical properties required to build the model are not well studied for InGaP compositions near a lattice constant of 5.57Å, we set out to empirically test the results of the model.

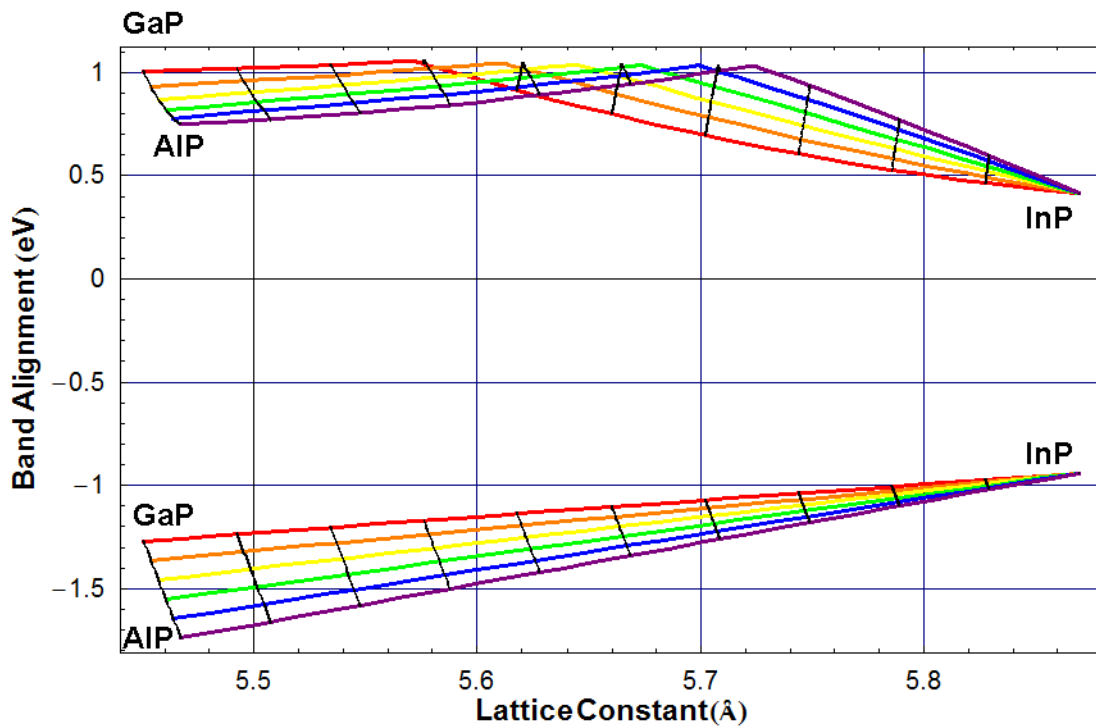


Figure 6.4 Band alignment (VB referenced to InSb) as a function of lattice constant for the entire AlInGaP system. The type-II alignment between GaP and AlP and type-I offset between GaP and InP cause a kink in the CB band edge with composition. Note that for the widest direct band gap InGaP (near 5.58Å) addition of Al lowers the CB edge.

We have demonstrated a large range of PL and CL wavelengths in this materials system. With room temperature CL measurements, we observed luminescence from bulk layers ranging from 540nm to beyond 620nm that are in good agreement with literature values (Figure 5.4). We have also observed PL and CL intensity from strained QW

heterostructures ranging from about 550nm to 610nm, corresponding to that predicted by the model as well (Figure 6.5 and Figure 6.6).

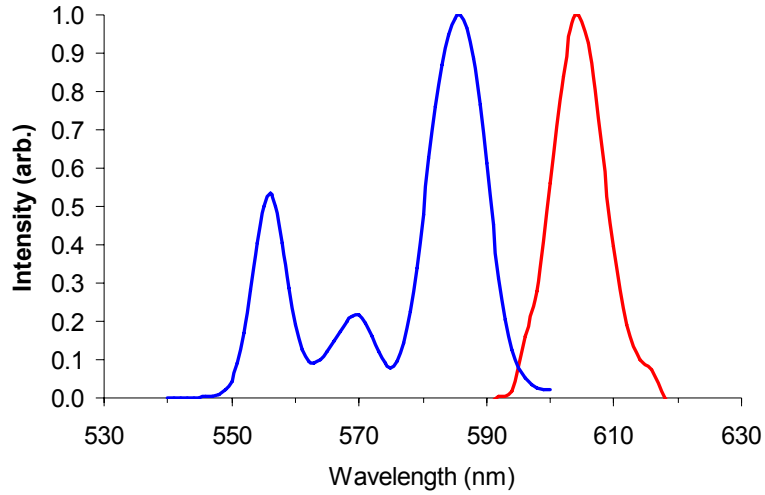


Figure 6.5 20K PL intensity for two samples with different structures designed to demonstrate the range of accessible wavelengths. The left trace is a sample which contains three quantum wells and three characteristic peaks while the right trace has a single quantum well.

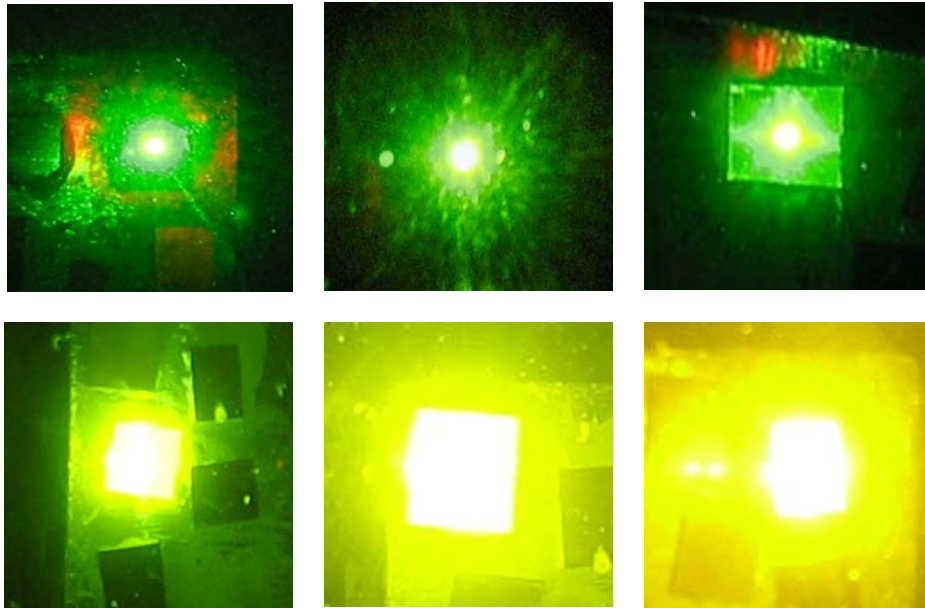


Figure 6.6 Ar-ion laser filtered photographs of 20K PL of various InGaP heterostructures showing luminescence ranging from 562nm (top left) to 584nm (lower right).

Perhaps the greatest difficulty predicted is the type II offset between compositions of AlInGaP and InGaP near the lattice constant of 5.58\AA , where we expect the greenest devices to be possible. To test the alignment we intentionally built a predicted type-II heterostructure and tested its luminescence behavior. This structure is a nominally unstrained 300\AA $\text{In}_{0.3}\text{Ga}_{0.7}\text{P}$ QW clad by $\text{In}_{0.31}(\text{Al}_{0.45}\text{Ga}_{0.55})_{0.69}\text{P}$; the predicted conduction band offset is approximately $-2kT$ at room temperature. Without any conduction band confinement, very little emission from the 300\AA InGaP layer is expected. Possible transitions are indicated in Figure 6.7. Room temperature CL yielded a strong peak at 566nm with no clear peak at 580nm (see Figure 6.8). The intensity of the detected peak was significantly greater than that of high quality InGaP and GaAsP bulk layers, indicating that the dominant transition was recombination of a confined state in the $\text{In}_{0.3}\text{Ga}_{0.7}\text{P}$ layer. We conclude that the structure likely has a type-I alignment with AlInGaP. Thus we see that our literature-based prediction is likely incorrect and that significant confinement may exist for heterostructures at this lattice constant. Such confinement gives additional promise for the fabrication of an AlInGaP laser diode operating at a pure green wavelength as short as 550nm .

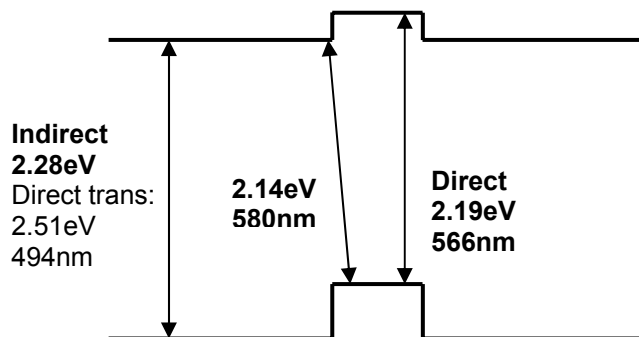


Figure 6.7 Predicted band schematic of the alignment test sample. Type-I transitions are expected at 566nm while type-II are expected at 580nm .

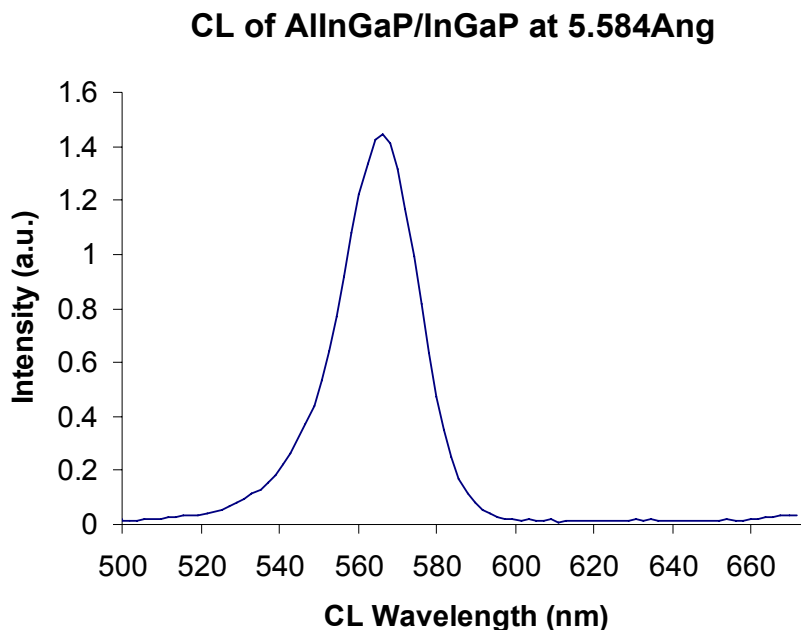


Figure 6.8 The observed CL emission of the sample indicated in Figure 6.7. The primary emission is precisely where expected, at 566nm and there is no significant peak at 580 or longer, indicating that the alignment is likely to be type-I.

6.3 Device Fabrication and Testing

In order to fully explore the device possibilities for this system, MOCVD growth of several device heterostructures on GaAsP virtual substrates was carried out using an 8” Thomas Swan/Aixtron close coupled showerhead reactor operated at 100mTorr with 20slm of N₂ as the carrier. Precursors were TMGa, TMIIn and PH₃, as well as DMZn and H₂ diluted Si₂H₆ as the dopants. Cross section TEM was performed to confirm layer thicknesses along with XRD to confirm cladding compositions. SIMS measurements were carried out to confirm dopant concentrations. For all devices, donor and acceptor target concentrations were $2 \times 10^{18} \text{cm}^{-3}$. Cladding thicknesses were approximately 1 μm with QW ranging from 70Å to 150Å. TEM images of two devices presented here are shown in Figure 6.9.

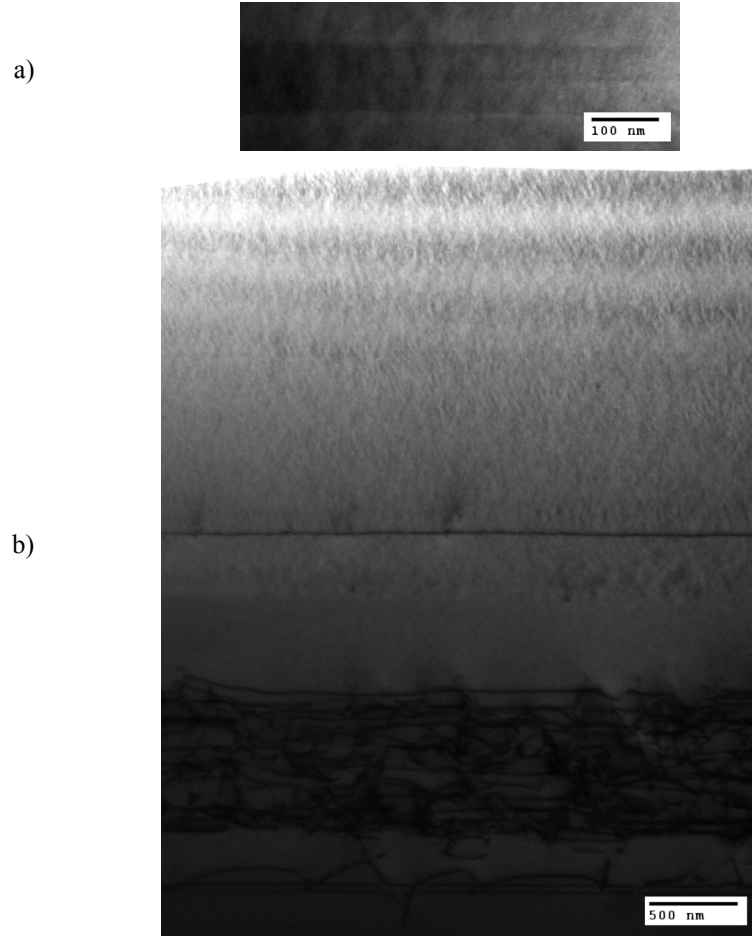


Figure 6.9 Cross section $\langle 022 \rangle$ bright field TEM images of two device heterostructures. In a), and AlInGaP-based SCH structure is shown while b) is an Al-free InGaP strained QW.

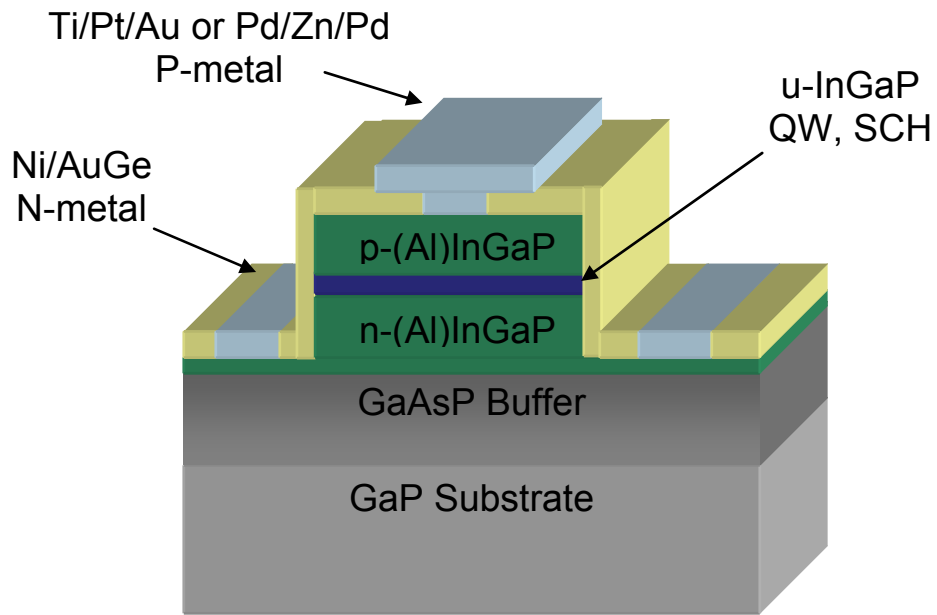


Figure 6.10 Schematic of top contact ridge waveguide laser showing wet etched mesas, SiO₂ passivation and lift-off metallization.

Wafers were fabricated with a ridge waveguide stripe laser design as shown schematically in Figure 6.10. Photolithography was performed using OCG825 positive resist and plasma enhanced CVD SiO₂ hard mask to define mesas 100 μ m wide. The ridges were wet etched using 3:1 HCl:HNO₃ (aqua regia) with an etch rate of about 330 \AA /s. Care was taken to etch to a depth slightly past the quantum well to maximize current spreading in the ultimate device. The mesas were then passivated with PECVD SiO₂, contact cuts were defined and etched using buffered oxide etchant; n-contacts were 40 μ m wide and p-contacts ranged from 3 μ m to 20 μ m. Next, n- and p-metallization was carried out separately using image reversal lithography, e-beam evaporation and lift-off. The n-contact consisted of 100 \AA of Ni followed by about 1500 \AA eutectic GeAu alloy. The p-contact was 300 \AA Pd, 700 \AA Zn and 1000 \AA Pd. Rapid thermal anneals (RTA) of the contacts for 30s at 450 $^{\circ}$ C or 500 $^{\circ}$ C was performed to obtain ohmic behavior. Finally,

device facets were cleaved by hand along a $\langle 110 \rangle$ direction such that bars approximately 1mm in width could be tested. It should be noted that this device design is intended to produce a laser. In contrast, modern LED device designs typically incorporate extraordinary measures to aid photon extraction. We emphasize that these devices were not optimized LEDs and as such external quantum efficiency was expected to be low.

The finished devices were manually probed and tested under forward bias using pulsed and CW power supplies. Lasing was not observed, but incoherent EL was bright to the unaided eye in ambient room lighting. Spectra of the emission were also measured.

6.4 Device Performance

I-V curves under forward bias are compared for the two annealing conditions used in Figure 6.11. RTA is required for both n- and p-contacts to facilitate interfacial reactions meant to enhance ohmic behavior^{78, 79}. Ni/AuGe n-contacts are typically used for GaP-, InP- and GaAs-based devices and were expected to perform well for this intermediate alloy. On the other hand, given that p-alloys have had varied success in different systems and tend to be tailored to the alloy to which they are paired, we expected the p-contact to dominate diode series resistance. From the I-V characteristics we see that the 500°C anneal reduced diode turn on voltage and series resistance. In fact, resistance of the 500°C annealed sample approaches that of conduction through the n-layer, from n- to n-contact underneath the device. This indicates that parasitic resistance in the p-contacts is close to that in the n-contact. We expect that the contacts can be significantly improved through other RTA treatments or use of different alloys.

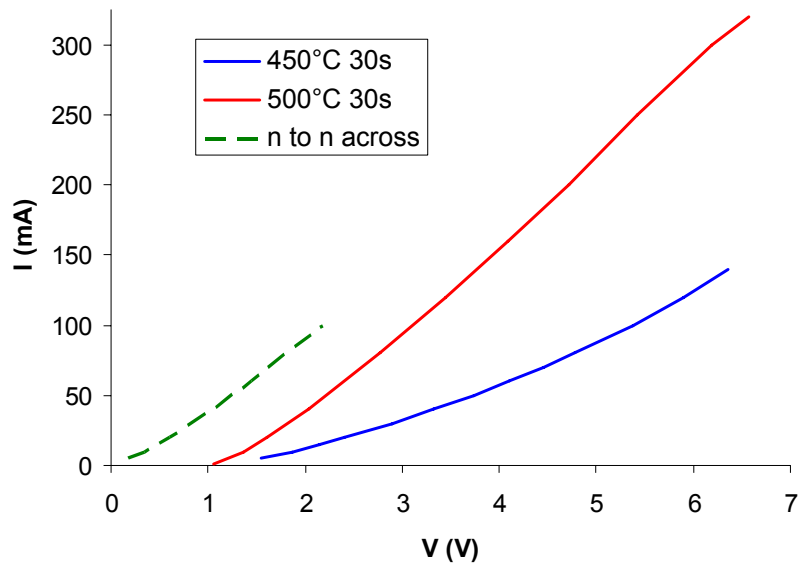


Figure 6.11 Comparison of I-V characteristics of a diode subjected to a 30s anneal at 450°C or 500°C. For comparison, also shown is data for conduction across the 500°C annealed device, from n to n contacts.

Devices tested span a lattice constant range of 5.534Å to 5.569Å corresponding to an In fraction of 0.2 to 0.28 in InGaP. Figure 6.12 and Figure 6.13 show spectra for these devices and demonstrates access to a wide range of colors (from green, 570nm, to amber, 606nm). Light extraction efficiency from the devices was poor and predominantly from the top near the contacts. Use of thicker current spreading layers would have generated photons away from underneath the contacts, raising the probability that they escape from the surface of the device. The magnitude of the measured intensity therefore was largely arbitrary and depended on how well the fiber coupling to the spectrometer was aligned to minor defects or scratches in the metallization where light emission was stronger. For this reason all spectra are given in normalized form and no optical power measurements are presented.

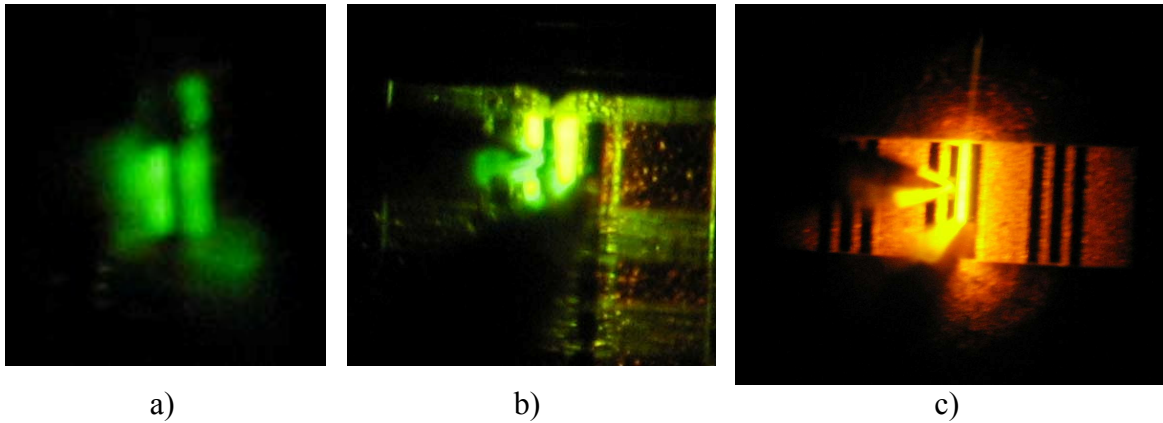


Figure 6.12 Photomicrographs of electroluminescence as seen from the top side of the devices. Colors correspond to a) 570nm (green), b) 575nm (yellow-green) and c) 606nm(amber).

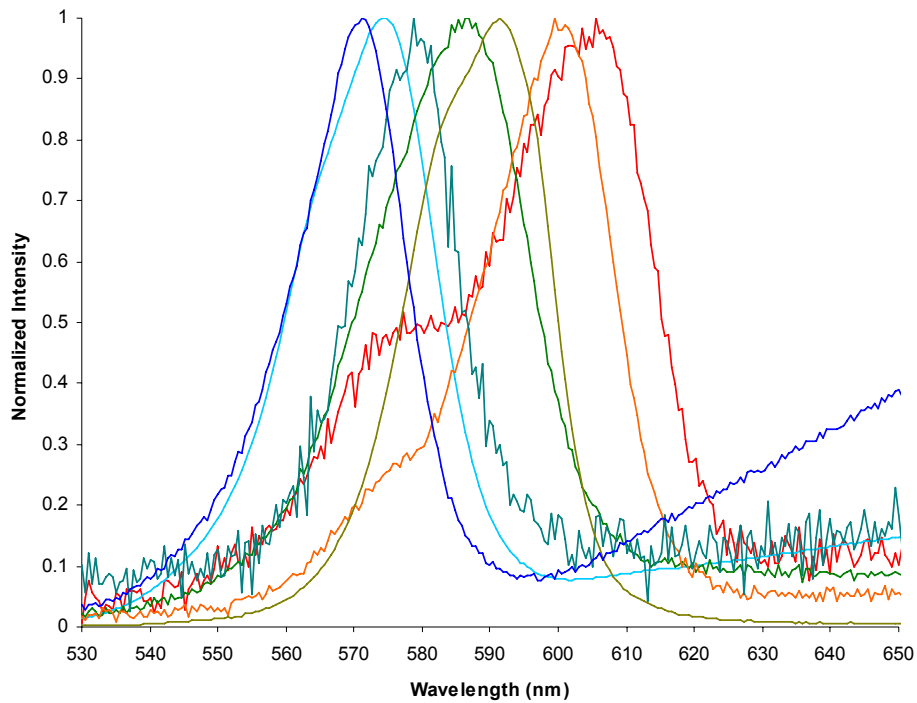


Figure 6.13 Normalized spectra for a variety of devices tested, demonstrating access to a wide range of the visible spectrum with our very flexible device platform.

Through variation of the MOCVD growth temperature we were able to control the presence of CuPt-B ordering in the active layers. Figure 6.14 and Figure 6.15 compare spectra from devices with ($T_g=650^\circ\text{C}$) and without ordering ($T_g=725^\circ\text{C}$). We believe that

radiative recombination happens preferentially in ordered domains of active layers where band gap is locally reduced. The result is the presence of superimposed peaks from ordered and disordered regions. At higher growth temperatures the effect of ordering is much reduced; this is also apparent in the spectral shape of the devices grown at 725°C, where the blue “disordered” shoulder is missing.

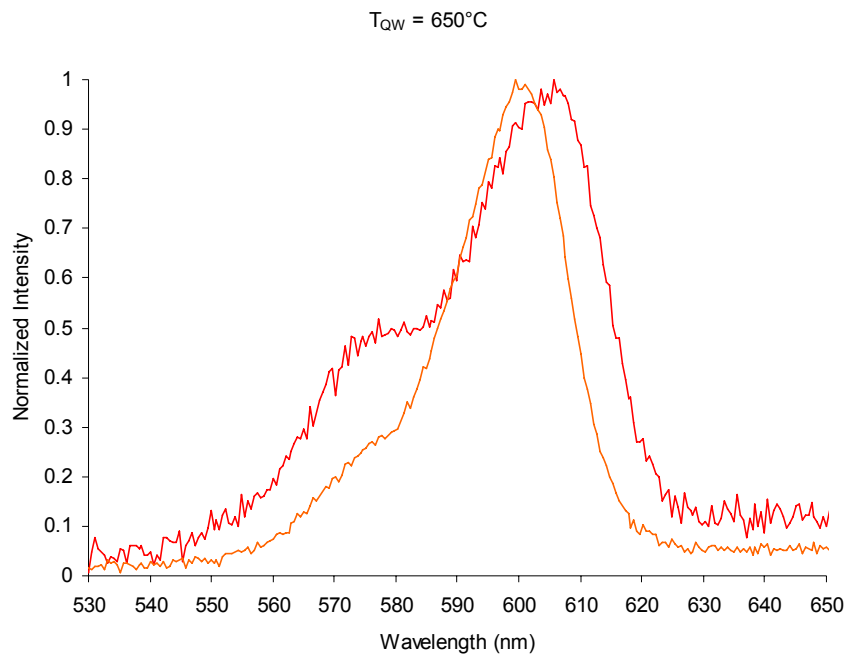


Figure 6.14 LED spectra from two similar devices with ordered domains in the QW, due to a relatively low growth temperature of 650°C. Preferential recombination in the lower bandgap ordered regions results in a primary “red” peak as compared to the secondary “blue,” disordered shoulder. Both devices consisted of In_{0.32}Ga_{0.68}P QWs with slightly varied cladding compositions.

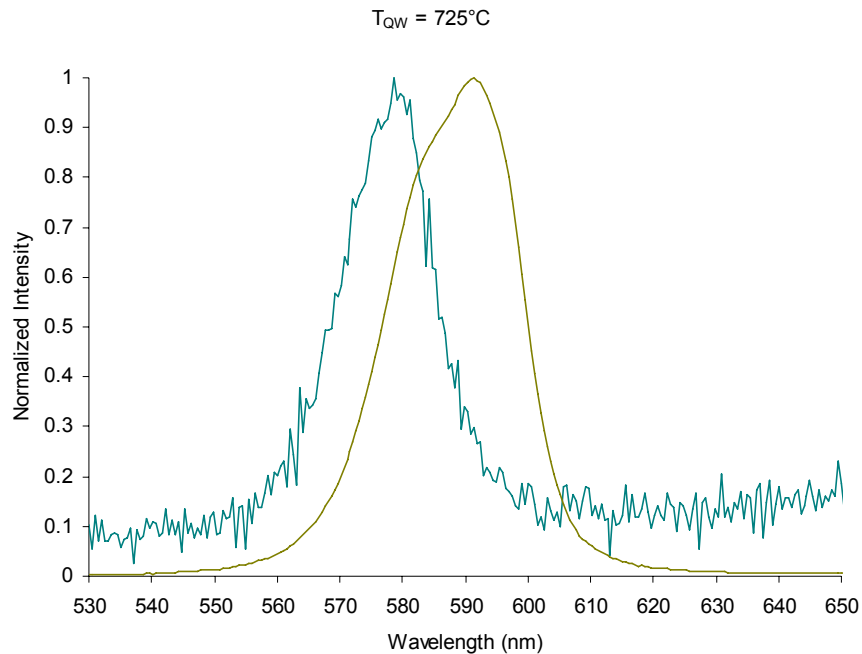


Figure 6.15 LED spectra from two devices with disordered QWs grown at 725°C. Note the large blue-shift of the peaks compared to those in Figure 6.14 despite the fact that their QWs contain significantly more In (579nm peak from a $\text{In}_{0.38}\text{Ga}_{0.62}\text{P}$ QW and 592nm from a $\text{In}_{0.36}\text{Ga}_{0.64}\text{P}$ QW).

The effects of InGaP composition and defects inside the active layers are shown quite well in Figure 6.16 where spectra of the greenest devices are presented. Several devices fabricated on a single wafer are shown. In this growth run, a slight variation of growth temperature across the wafer resulted in a composition gradient in the active InGaP. As a result, portions of the wafer deficient in In underwent tensile relaxation resulting in a high density of defects while other portions had much lower defect densities. The effect on the spectra is clear: the defective devices exhibit greener emission due to the higher band gap of the cladding and QW, but also have a broad red secondary peak arising from deep defect levels. Despite the limitations of the LED design, each of the devices tested illuminated brightly, even as they approached the indirect crossover of InGaP.

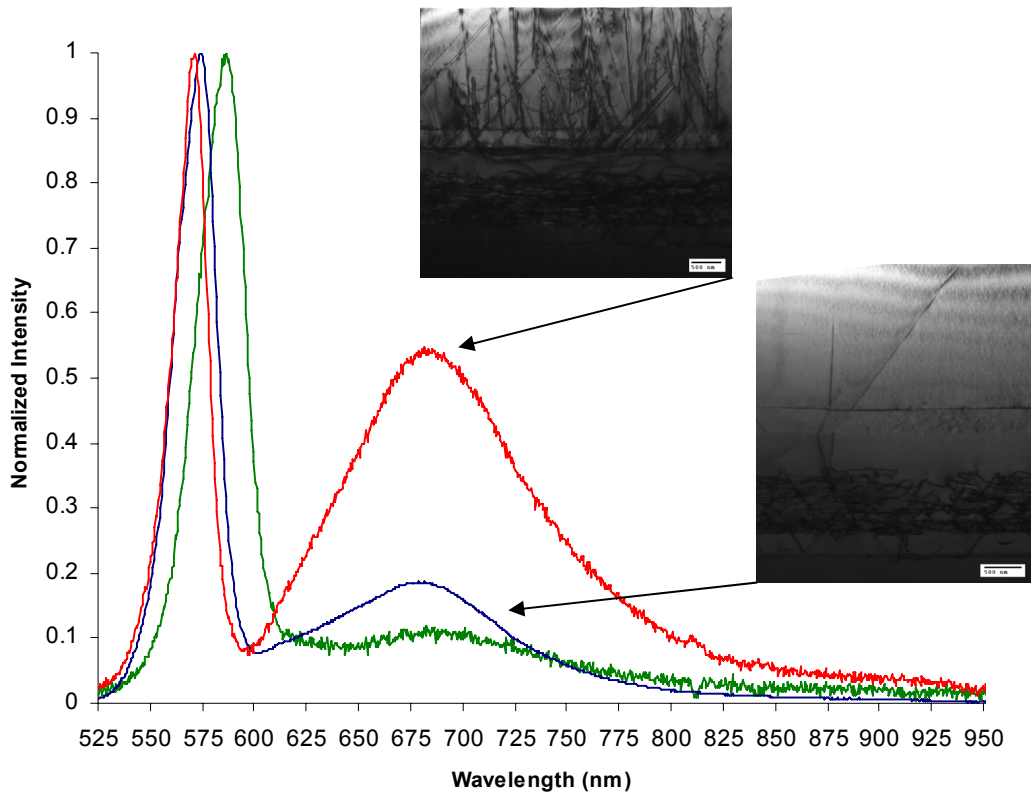


Figure 6.16 LED spectra from several devices from the same wafer where a composition gradient across the wafer resulted in tensile mismatch in the InGaP and incorporation of a high density of defects. Changes in In fraction of just 3-4% result in large shifts in color, of greater than 15nm.

6.5 Conclusions and Future Work

We have successfully fabricated light emitting diodes emitting across a range of colors, from green to amber. GaAsP buffer layers provide a low threading dislocation density materials base in which we can access novel AlInGaP compositions to probe possible green and yellow emission from solid-state devices. By providing excellent control of the microstructure of (Al)InGaP on GaAsP, we are able to demonstrate that lasers and LEDs from the orange to the green-yellow are possible in this materials system. Pure green lasers, down to approximately 550nm, may also be possible with fine-tuning of this materials system. In future work we suggest that investigation of simple

LED designs will shed more light on the nature of the transition of the band gap from direct to indirect and confinement in the QW. Understanding the electronic structure will better enable the experimenter to successfully fabricate a laser diode near these wavelengths.

Chapter 7 Results Summary, Suggestions for Future Work

7.1 Overview

The overarching theme of this thesis project has been MOCVD growth of heterostructures in support of integration of novel materials on a variety of substrates for yellow to green emitting semiconductor optical devices. The ultimate goal was fabrication of high efficiency green and yellow-green devices on a versatile and manufacturable platform. Through the use of modern MOCVD technology we successfully demonstrated unprecedentedly high quality virtual substrates with access to any lattice constant between GaP and GaAs. Using this platform we showed definitive evidence for the mechanisms of formation of several defects in the optical material and we demonstrated methods to avoid them. Finally we successfully fabricated light emitting devices with access to a wide range of the visible spectrum. In a collaborative effort with Carl Dohrman, this work also led to the successful integration of the GaAsP and SiGe virtual substrate platforms.

7.2 Summary of Results

Virtual Substrate Technology

Initial efforts focused on improving the quality of compressively graded InGaP and AlInGaP virtual substrates on GaP. Previously, techniques were identified to delay onset and diminish the strength of branch defects, the primary obstacle to efficient dislocation glide and threading defect reduction in InGaP metamorphic graded buffers. Here we focused on the use of new materials and optimization techniques, but failed to significantly further improve the graded InGaP platform.

Instead we looked toward an older, technologically obsolete platform, hydride vapor epitaxial GaAsP, and applied modern MOCVD to produce a novel system. This route yielded excellent results, enabling virtual substrates with extremely low threading defect density (10^4cm^{-2} to 10^5cm^{-2}) while also reducing the thickness of the metamorphic buffer to as thin as $1.3\mu\text{m}$. Excellent thermodynamics of mixing prevents phase separation defects in the GaAsP, the primary obstacle encountered in InGaP grades. Tensile GaAsP on GaAs exhibited unusually smooth morphologies effectively starving the system of dislocation nucleation, but was limited by the thickness of films required to prevent onset of cracking. Compressive GaAsP on GaP yielded very low threading defect densities at extremely thin graded layer thicknesses.

Microstructure Studies

The difficulties of working with mixed anion GaAsP were overcome through the use of single anion stabilizing layers which allowed the GaAsP virtual substrates to be used just as their name suggests, as substrate replacements where lattice constant is no longer constrained. This method permitted the use of the very simple-to-produce optimized compressive GaAsP graded buffers for the remainder of the project. On this platform we successfully controlled CuPt-B ordering in InGaP such that the maximum bandgap could be achieved in this system, an essential goal for obtaining the best green devices possible. We also successfully expanded upon previous work on phase separation defects in InGaP⁴¹, identifying conditions under which we avoided their formation which is so deleterious to optical devices. Above all, in this portion of the thesis we were able to identify the atomic mechanism for each of the defects (GaAsP surface undulation, CuPt-B order and phase separation in InGaP) and the necessary optimizations to growth to

defeat them. In a competitive two-step adatom incorporation model, we see that surface and sublayer atomic diffusivity determines the degree of formation of short- and long-range order at the MOCVD growth surface and how this order is subsequently destroyed. By manipulating MOCVD growth parameters we are able to control the mechanisms which determine the final atomic configuration.

Fabrication of Light Emitting Devices

The previous successes of the project were quickly leveraged for successful fabrication of LEDs. Although this portion of the project did not yield a yellow solid-state laser as hoped, prospects are excellent for future studies. We were able to demonstrate a variety of devices emitting from 606nm (amber) to 570nm (green). We also learned more about the electronic structure and behavior of these unconventional heterostructures.

The ridge waveguide laser fabrication process was pioneered for this system and metallization schemes were studied. Now equipped with the better understanding of device growth and fabrication, production of improved devices should be relatively straightforward.

Integration of GaAsP on SiGe

In collaborative work with Carl Dohrman (results not presented here), successful integration of GaAsP on the SiGe platform was also demonstrated. Monolithic integration of InGaP/GaAsP on the Si platform will expand the portfolio of technology of the Fitzgerald Group significantly. Through the combination of technology developed in this and Dohrman's thesis we expect that development of yellow to red light emitters on Si will also be straightforward.

7.3 Suggestions for Future Studies

The development of the GaAsP virtual substrates was truly exciting work and yielded excellent results, but better understanding of several aspects of the project would be satisfying. First, a careful comparison of similar grade rate compressive and tensile GaAsP on similar defect density substrates could shed more light on the similarities and differences in dislocation dynamics in the tensile and compressive systems. Second, implementing crack-toughening structures (several integrated compressive layers within the tensile grade, perhaps) to tensile strained GaAsP could lead to *simultaneously* extremely low defect density and extremely thin virtual substrates.

While the microstructural quality of AlInGaP was highly controlled by the end of this work, more study for a wider range of alloys would be helpful. For example, successful growth and characterization of AlInP might allow fabrication of interesting visible light emitters both at lattice constants less than and *greater than* GaAs (which could be supported by InGaAs grades). Modification of the MOCVD reactor might also enable a wider range of access to high V/III and high growth rate regimes where even greater flexibility might be achieved. Additionally finer control over TMSb flow would enable richer study of surfactant-mediated growth of InGaP materials, perhaps again enabling greater growth regime flexibility.

The most promising avenues (at smallest cost) for further research will of course be in further development of the light emitting device fabrication. First, simple incremental improvement of the fabrication process in areas such as metallization (ohmic behavior of the contacts without large series resistances) and optimization of device doping could have significant overall impact on device performance. Now that growth processes are

well understood and finalized for a variety of device designs, full studies of the electronic structure of these exotic alloys can be conducted. Most important will be the determination of optimized device parameters for a solid-state laser. Fabrication of several rounds of devices should be straightforward and are likely to lead to successful demonstration of a laser. We expect that the ultimate short wavelength limit of the system will be around 550nm and should be obtainable by using AlInGaP alloys with greater Al fraction than those studied here. Given that AlInGaP/InGaP heterostructures appear to luminesce well, AlInGaP/AlInGaP heterostructures with higher Al fraction also hold promise for even shorter wavelength devices. Perhaps the route with greatest promise for developing the yellow laser would be to start with the GaAs lattice constant where red LDs are relatively well known and should be simple to fabricate, then move to smaller lattice constant incrementally, analyzing the effect on LD performance as progress towards GaP is made.

Alternately, focus could be shifted from obtaining the solid-state laser to the efficient green LED. Fabrication of simpler homojunction, double sided contact LEDs should be low-cost and very straight-forward. Again, performance as a function of lattice constant should be evaluated. A study of quantum efficiency with the alloys proximity to the indirect/direct crossover point would be very helpful—this part of the project was never fully addressed and remains as one of the primary arguments against using these low-In alloys of InGaP. Perhaps most exciting for this line of work would be the implementation of an AlAsP graded buffer which could potentially simultaneously realize the high quality of the GaAsP virtual substrates as well as function as a fully

transparent epitaxial substrate with its associated benefit of improved photon extraction. Unfortunately this research path is likely to encounter the greatest difficulties.

Lastly we come to suggestions for integration of InGaP/GaAsP/SiGe. Great progress in this arena was made in a relatively short time. With improved surface preparation and wafer handling, I believe that full 6" wafers of high quality GaAsP on SiGe will be possible. This prediction, along with the success of Chilukuri⁶ indicates that any success afforded by further research on yellow-green emitters will translate directly to monolithic-CMOS applications.

Appendix A Example GaAsP Growth Sheet

SEL GaPAs Linear Graded Buffer on GaP

Constant Grading Rate, Chosen Step Time, VIII Ratio and Step Thickness, Varying Composition

Target Grading Rate	-1.80%	1.8E-06	3.14
Target VIII Ratio	See below		436 Å/min
Effective TMG SCCM			8.27 Å/s
GaAsP growth rate			9924 Å
Total Thickness			233955
total time			

PH3 corr	0.7500192
ASH3 corr	0.6734706
aGaAs	5.65265 Å
aGaP	5.49060 Å

Growth Process Sequence

Step Number	PH3 MFC	ASH3-1 output	ASH3-2 Req	zP	MF	Solid	Step Time	Step Thickness	Step Mismatch Rate	Grading	PH3 / (ASH3+PH3)	required		needed		Lattice Equation				
												calculated	desired	PH3	ASH3		SCCM	Constant Rate	Growth	Desired Grade Rate
0	413.5	0.0	0.0	100.0%	0.0	100.0%	10	4362 Å	0.000%	0.000%	1.0000	100	0.04	436 Å/min	313.85	0.00	5.4906 Å	436 Å/min	5.49060 Å	0.20275
1	409.8	0.0	4.1	98.8%	1.3333	662 Å	1.3333	662 Å	-0.18%	-1.800%	0.9911	100	0.03	436 Å/min	310.7	2.78	5.4570 Å	436 Å/min	5.49060 Å	0.20275
2	405.7	0.0	8.3	93.6%	1.3333	662 Å	1.3333	662 Å	-0.18%	-1.800%	0.9811	100	0.07	436 Å/min	307.91	5.94	5.4635 Å	436 Å/min	5.49060 Å	0.20275
3	401.0	0.0	14.1	90.4%	1.3333	662 Å	1.3333	662 Å	-0.18%	-1.800%	0.9698	100	0.10	436 Å/min	304.37	9.48	5.4700 Å	436 Å/min	5.49060 Å	0.20275
4	395.8	0.0	20.0	87.2%	1.3333	662 Å	1.3333	662 Å	-0.18%	-1.800%	0.9571	100	0.14	436 Å/min	300.39	13.48	5.4765 Å	436 Å/min	5.49060 Å	0.20275
5	389.9	0.0	26.6	83.9%	1.3333	662 Å	1.3333	662 Å	-0.18%	-1.800%	0.9430	100	0.18	436 Å/min	295.95	17.30	5.4831 Å	436 Å/min	5.49060 Å	0.20275
6	383.4	0.0	33.9	80.7%	1.3333	662 Å	1.3333	662 Å	-0.18%	-1.800%	0.9273	100	0.22	436 Å/min	291.02	22.83	5.4896 Å	436 Å/min	5.49060 Å	0.20275
7	375.4	0.0	41.9	77.5%	1.3333	662 Å	1.3333	662 Å	-0.18%	-1.800%	0.9102	100	0.26	436 Å/min	285.66	28.19	5.4962 Å	436 Å/min	5.49060 Å	0.20275
8	365.8	0.0	50.4	74.3%	1.3333	662 Å	1.3333	662 Å	-0.18%	-1.800%	0.8919	100	0.31	436 Å/min	279.92	33.93	5.5027 Å	436 Å/min	5.49060 Å	0.20275
9	355.9	0.0	59.3	71.0%	1.3333	662 Å	1.3333	662 Å	-0.18%	-1.800%	0.8727	100	0.36	436 Å/min	273.80	39.95	5.5092 Å	436 Å/min	5.49060 Å	0.20275
10	345.7	0.0	68.6	67.8%	1.3333	662 Å	1.3333	662 Å	-0.18%	-1.800%	0.8529	100	0.41	436 Å/min	267.67	46.18	5.5158 Å	436 Å/min	5.49060 Å	0.20275
11	344.2	0.0	78.1	64.5%	1.3333	662 Å	1.3333	662 Å	-0.18%	-1.800%	0.8325	100	0.46	436 Å/min	261.28	52.57	5.5224 Å	436 Å/min	5.49060 Å	0.20275
12	335.6	0.0	87.8	61.3%	1.3333	662 Å	1.3333	662 Å	-0.18%	-1.800%	0.8116	100	0.51	436 Å/min	254.73	59.12	5.5290 Å	436 Å/min	5.49060 Å	0.20275
13	325.8	0.0	97.8	58.0%	1.3333	662 Å	1.3333	662 Å	-0.18%	-1.800%	0.7902	100	0.57	436 Å/min	248.02	65.84	5.5356 Å	436 Å/min	5.49060 Å	0.20275
14	317.6	0.0	108.8	54.8%	1.3333	662 Å	1.3333	662 Å	-0.18%	-1.800%	0.7682	100	0.63	436 Å/min	241.08	72.77	5.5422 Å	436 Å/min	5.49060 Å	0.20275
15	308.1	0.0	118.9	51.5%	1.3333	662 Å	1.3333	662 Å	-0.18%	-1.800%	0.7452	100	0.70	436 Å/min	233.88	79.97	5.5488 Å	436 Å/min	5.49060 Å	0.20275
16	298.1	0.0	130.0	48.3%	1.3333	662 Å	1.3333	662 Å	-0.18%	-1.800%	0.7210	100	0.77	436 Å/min	226.30	87.55	5.5554 Å	436 Å/min	5.49060 Å	0.20275
17	287.5	0.0	142.0	45.0%	1.3333	662 Å	1.3333	662 Å	-0.18%	-1.800%	0.6953	100	0.85	436 Å/min	218.23	95.62	5.5620 Å	436 Å/min	5.49060 Å	0.20275
18	276.0	0.0	154.9	41.7%	1.3333	662 Å	1.3333	662 Å	-0.18%	-1.800%	0.6671	100	0.93	436 Å/min	209.52	104.33	5.5687 Å	436 Å/min	5.49060 Å	0.20275
19	263.4	0.0	169.1	38.4%	1.3333	662 Å	1.3333	662 Å	-0.18%	-1.800%	0.6371	100	1.02	436 Å/min	199.96	113.89	5.5753 Å	436 Å/min	5.49060 Å	0.20275
20	249.4	0.0	184.9	35.2%	1.3333	662 Å	1.3333	662 Å	-0.18%	-1.800%	0.6031	100	1.11	436 Å/min	189.30	124.85	5.5820 Å	436 Å/min	5.49060 Å	0.20275
21	233.5	2.9	200.0	31.9%	1.3333	662 Å	1.3333	662 Å	-0.18%	-1.800%	0.5647	100	1.21	436 Å/min	177.22	136.63	5.5886 Å	436 Å/min	5.49060 Å	0.20275
22	215.3	23.3	200.0	28.6%	1.3333	662 Å	1.3333	662 Å	-0.18%	-1.800%	0.5208	100	1.30	436 Å/min	163.44	150.41	5.5953 Å	436 Å/min	5.49060 Å	0.20275
23	194.9	46.4	200.0	25.3%	1.3333	662 Å	1.3333	662 Å	-0.18%	-1.800%	0.4713	100	1.39	436 Å/min	147.90	165.95	5.6019 Å	436 Å/min	5.49060 Å	0.20275
24	172.7	71.4	200.0	22.0%	1.3333	662 Å	1.3333	662 Å	-0.18%	-1.800%	0.4176	100	1.48	436 Å/min	131.06	182.79	5.6086 Å	436 Å/min	5.49060 Å	0.20275
25	149.9	97.1	200.0	18.7%	1.3333	662 Å	1.3333	662 Å	-0.18%	-1.800%	0.3624	100	1.57	436 Å/min	113.75	200.10	5.6153 Å	436 Å/min	5.49060 Å	0.20275
26	127.3	100.0	200.0	15.4%	1.3333	662 Å	1.3333	662 Å	-0.18%	-1.800%	0.3079	100	1.69	436 Å/min	96.62	217.23	5.6220 Å	436 Å/min	5.49060 Å	0.20275
27	105.1	100.0	200.0	12.1%	1.3333	662 Å	1.3333	662 Å	-0.18%	-1.800%	0.2542	100	1.85	436 Å/min	79.78	234.07	5.6287 Å	436 Å/min	5.49060 Å	0.20275
28	82.8	100.0	200.0	8.8%	1.3333	662 Å	1.3333	662 Å	-0.18%	-1.800%	0.2002	100	2.08	436 Å/min	62.83	251.02	5.6354 Å	436 Å/min	5.49060 Å	0.20275
29	59.1	100.0	200.0	5.5%	1.3333	662 Å	1.3333	662 Å	-0.18%	-1.800%	0.1428	100	2.46	436 Å/min	44.83	269.02	5.6421 Å	436 Å/min	5.49060 Å	0.20275
30	30.6	100.0	200.0	2.2%	1.3333	662 Å	1.3333	662 Å	-0.18%	-1.800%	0.0740	100	3.35	436 Å/min	23.24	290.61	5.6488 Å	436 Å/min	5.49060 Å	0.20275
31	-0.3	100.0	200.0	0.0%	1.3333	662 Å	1.3333	662 Å	-0.18%	-1.800%	-0.0007	100	#DIV/0!	436 Å/min	-0.22	314.07	5.6555 Å	436 Å/min	5.49060 Å	0.20275

Appendix B Mathematica Code for InGaP strained QW Model

InGaP Strained QW Model

```
(*Needs["Graphics`Master`"]*)
Remove["Global`*"]
Off[FindRoot::cvnwt]
Off[FindRoot::frnum]
Off[FindRoot::frsec]
Off[General::stop]
Off[General::spell]
Off[General::spell1]
Off[Plot::plnr]

(* Enter plotting parameters here *)
xstart = .33;
xinc = .02;
(* Enter device parameters here *)
xsch = .263;
ysch = 0.36;
xqw = .36;
yqw = 0;
xclad = xsch;
yclad = ysch;
h = 40; (* in nanometers *)

(* Materials Constants *)
T = 300.;  $\hbar = \frac{4.136 \times 10^{-15}}{2\pi}$ ; mo = 5.69 \times 10^{-16};

(* Lattice Parameters *)
aGaP = 5.4505 \times 10^{-8} + 2.92 \times 10^{-13} (T - 300);
aInP = 5.8697 \times 10^{-8} + 2.79 \times 10^{-13} (T - 300);
aAlP = 5.4672 \times 10^{-8} + 2.92 \times 10^{-13} (T - 300);
aGaAs = 5.65325 \times 10^{-8} + 3.88 \times 10^{-13} (T - 300);

(* Lattice parameter bowing parameters-- Vegard's law makes these zero. *)
CaInGaP = 0; CaInAlP = 0; CaAlGaP = 0; CaGaAsP = 0;

(* Stiffnesses *)
C11GaP = 14.05 \times 10^{11};
C12GaP = 6.203 \times 10^{11};
C44GaP = 7.033 \times 10^{11};
C11InP = 10.11 \times 10^{11};
C12InP = 5.61 \times 10^{11};
C44InP = 4.56 \times 10^{11};
C11AlP = 13.3 \times 10^{11};
C12AlP = 6.3 \times 10^{11};
C44AlP = 6.15 \times 10^{11};
```

```

(* Stiffness bowing parameters-- no data *)
CC11InGaP = 0; CC11AlGaP = 0; CC11InAlP = 0; CC12InGaP = 0;
CC12AlGaP = 0; CC12InAlP = 0; CC44InGaP = 0; CC44AlGaP = 0; CC44InAlP = 0;

(* Carrier effective masses *)
(** Updated 3/3/06 to Vurgaftman's recommended  $m_{0c}^*$ ,
 $m_{lh}^*$  and  $m_{hh}^*$  interpolating technique **)
(*****
    meGaP=.13 mo;
    meInP=.0795 mo;
    meAlP=.22 mo;
    mlhGaP=.14 mo;
    mlhInP=.089 mo;
    mlhAlP=.155 mo;
    mhhGaP=.79 mo;
    mhhInP=.85 mo;
    mhhAlP=.8 mo;*****)

(* Effective mass bowing parameters-- no data *)
CmeInGaP = 0; CmeAlGaP = 0; CmeInAlP = 0;
CmlhInGaP = 0; CmlhAlGaP = 0; CmlhInAlP = 0;
CmhhInGaP = 0; CmhhAlGaP = 0; CmhhInAlP = 0;

(* Materials Constants for Calculation of Electron Effective Mass *)
EpGaP = 31.4; EpAlP = 17.7; EpInP = 20.7;
FGaP = -2.04; FAlP = -.65; FInP = -1.31;
AsoGaP = .08; AsoAlP = .07; AsoInP = .108;
(* Bowing Data *)
CAsoInGaP = 0; CAsoAlGaP = 0; (* no data *) CAsoInAlP = -.19;
CFInGaP = .78; CFAAlGaP = 0; (* no data *) CFInAlP = 0; (* no data *)
CEpInGaP = 0; (* no data *) CEpAlGaP = 0; (* no data *) CEpInAlP = 0; (* no data *)

(* Materials Constants for Calculation of Hole Masses *)
 $\gamma_{1GaP} = 4.05$ ;  $\gamma_{1AlP} = 3.35$ ;  $\gamma_{1InP} = 5.08$ ;
 $\gamma_{2GaP} = .49$ ;  $\gamma_{2AlP} = .71$ ;  $\gamma_{2InP} = 1.6$ ;
 $\gamma_{3GaP} = 2.93$ ;  $\gamma_{3AlP} = 1.23$ ;  $\gamma_{3InP} = 2.1$ ;
(* Bowing Parameters -- no data *)
C $\gamma_{1InGaP} = 0$ ; C $\gamma_{2InGaP} = 0$ ; C $\gamma_{3InGaP} = 0$ ;
C $\gamma_{1AlGaP} = 0$ ; C $\gamma_{2AlGaP} = 0$ ; C $\gamma_{3AlGaP} = 0$ ;
C $\gamma_{1InAlP} = 0$ ; C $\gamma_{2InAlP} = 0$ ; C $\gamma_{3InAlP} = 0$ ;

(* Band data *)
Eg $\Gamma GaP = 2.886 + .1081 * \left( 1 - \text{Coth} \left[ \frac{164}{T} \right] \right)$ ;
EgXGaP =  $2.35 - \frac{\alpha XGaP T^2}{T + \beta XGaP}$ ;  $\alpha XGaP = .5771 * 10^{-3}$ ;  $\beta XGaP = 372$ ;
EgLGaP =  $2.72 - \frac{\alpha LGaP T^2}{T + \beta LGaP}$ ;  $\alpha LGaP = .5771 * 10^{-3}$ ;  $\beta LGaP = 372$ ;
Eg $\Gamma InP = 1.4236 - \frac{\alpha \Gamma InP T^2}{T + \beta \Gamma InP}$ ;  $\alpha \Gamma InP = .363 * 10^{-3}$ ;  $\beta \Gamma InP = 162$ ;

```

```

EgXInP = 2.384 - 3.7*^-4 T;
EgLinP = 2.014 -  $\frac{\alpha_{LinP} T^2}{T + \beta_{LinP}}$ ;  $\alpha_{LinP} = .363*^-3$ ;  $\beta_{LinP} = 162$ ;
EgAlP = 3.63 -  $\frac{\alpha_{AlP} T^2}{T + \beta_{AlP}}$ ;  $\alpha_{AlP} = .5771*^-3$ ;  $\beta_{AlP} = 372$ ;
EgXAlP = 2.52 -  $\frac{\alpha_{XAlP} T^2}{T + \beta_{XAlP}}$ ;  $\alpha_{XAlP} = .318*^-3$ ;  $\beta_{XAlP} = 588$ ;
EgLAlP = 3.57 -  $\frac{\alpha_{LAlP} T^2}{T + \beta_{LAlP}}$ ;  $\alpha_{LAlP} = .318*^-3$ ;  $\beta_{LAlP} = 588$ ;
EgGaAs = 1.519 -  $\frac{\alpha_{GaAs} T^2}{T + \beta_{GaAs}}$ ;  $\alpha_{GaAs} = .5405*^-3$ ;  $\beta_{GaAs} = 204$ ;
EgXGaAs = 1.981 -  $\frac{\alpha_{XGaAs} T^2}{T + \beta_{XGaAs}}$ ;  $\alpha_{XGaAs} = .460*^-3$ ;  $\beta_{XGaAs} = 204$ ;
EgLGaAs = 1.815 -  $\frac{\alpha_{LGaAs} T^2}{T + \beta_{LGaAs}}$ ;  $\alpha_{LGaAs} = .605*^-3$ ;  $\beta_{LGaAs} = 204$ ;

(* Band bowing parameters. *)
CEgInGaP = .65(*.76 (*.65 is Vurgaftman's recommendation*));
CEgXInGaP = .2(*.2 is Vurgaftman's recommendation*); CEgLinGaP = 1.03;
CEgInAlP = -.48; CEgXInAlP = .38; CEgLinAlP = -.48;
CEgAlGaP = 0; CEgXAlGaP = .13; CEgLAlGaP = 0;
CEgGaAsP = .19; CEgXGaAsP = .24; CEgLGaAsP = .16;

(* Deformation Potentials, using Chuang's sign convention *)
acGaP = -8.2; avGaP = 1.7; bGaP = -1.6;
acInP = -6; avInP = .6; bInP = -2; acAlP = -5.7;
avAlP = 3; bAlP = -1.5;
(* Deformation Potential Bowing Params -- no data so far *)
CacInGaP = 0; CavInGaP = 0; CbInGaP = 0; CacInAlP = 0;
CavInAlP = 0; CbInAlP = 0; CacAlGaP = 0; CavAlGaP = 0; CbAlGaP = 0;

(* Valence Band Offsets (referenced to InSb), assuming no bowing -- Vurgaftman *)
VBOGaP = -1.27;
VBOInP = -.94;
VBOAlP = -1.74;

(* Valence Band Offsets (referenced to Gold),
   assuming no bowing -- Tiwari, approx *)
(*VBOGaP=-.797;
VBOInP=-.857;
VBOAlP=-1.27;*)

(* Valence Band Offsets (referenced to GaP), assuming no bowing --
   Made up values (ideal!:VBOGaP=0;VBOInP=.2;VBOAlP=-.05;) *)
(*VBOGaP=0;
VBOInP=0;
VBOAlP=0;*)

```

```

(* VBO bowing paramters -- no data *)
CVBOInGaP = 0; CVBOAlGaP = 0; CVBOInAlP = 0;

(* General quaternary interpolation code *)
(* Al=D In=B Ga=C P=A *)
u[x_, y_] :=  $\frac{1-x+y}{2}$ ;
v[x_, y_] :=  $\frac{2-x-2y}{2}$ ;
w[x_, y_] :=  $\frac{2-2x-y}{2}$ ;

(* These fetch the binary compound data for the desired property, f. *)
AB[f_] := ToExpression[ToString[f] <> "InP"];
AC[f_] := ToExpression[ToString[f] <> "GaP"];
AD[f_] := ToExpression[ToString[f] <> "AlP"];

(* These fetch the ternary bowing data for the desired property, f. *)
CABC[f_] := ToExpression["C" <> ToString[f] <> "InGaP"];
CACD[f_] := ToExpression["C" <> ToString[f] <> "AlGaP"];
CABD[f_] := ToExpression["C" <> ToString[f] <> "InAlP"];

(* These return the ternary interpolation for the desired property,
f and appropriate composition var. Note the form: AX1-varYvar *)
ABC[var_, fun_] := var AC[fun] + (1 - var) AB[fun] - var (1 - var) CABC[fun];
ACD[var_, fun_] := var AD[fun] + (1 - var) AC[fun] - var (1 - var) CACD[fun];
ABD[var_, fun_] := var AD[fun] + (1 - var) AB[fun] - var (1 - var) CABD[fun];

(* ABCD[x,y,f] yields the quaternary interpolation of f property where the
quaternary has the form form ABm Cn Do with 0 ≤ (m,n,o) ≤ 1 and m+n+o=1. *)
(* Q (x, y, z) =  $\frac{yx T_{12}(u) + yz T_{23}(v) + xz T_{13}(w)}{xy + yz + xz}$  *)
(* u =  $\frac{1-x+y}{2}$ , v =  $\frac{1-y+z}{2}$ , w =  $\frac{1-x+z}{2}$  *)
(* In this file, Al=D In=B Ga=C P=A such that we have Alo Inm Gan P *)
(* In this file x and y refer to Inx (Aly Ga1-y)1-x P *)
(* So n=(1-x)(1-y) and m=x *)
(* This formulation is indeterminate if either or both x and y equal 0. Hence the
need for a switch to take care of the x=0, y=0, or x=y=0 cases. *)
ABCDtest[x_, y_, fun_] := (x (1-x) (1-y) ABC[u[x, (1-x) (1-y)], fun] +
((x-1)2 (1-y) y ACD[v[x, (1-x) (1-y)], fun] +
x y (1-x) ABD[w[x, (1-x) (1-y)], fun]) / ((1-x) (x+y-x y-y2+x y2));
ABCD[x_, y_, fun_] := Switch[{x == 0, y == 0, x == 1}, {False, True, True},
ABCDtest[.99999, 10-6, fun], {False, True, False},
ABCDtest[x, 10-6, fun], {True, False, False}, ABCDtest[10-6, y, fun],
{True, True, False}, ABCDtest[10-6, 10-6, fun], {False, False, True},
ABCDtest[.99999, 10-6, fun], {False, False, False}, ABCDtest[x, y, fun]];

(***** UPDATED 3/2/06 WITH QUATERNARY INTERPOLATION FORMULAE*****

(* Inx Ga1-x P *)
EgIInGaP = (1 - x) EgIGaP + x EgIInP - x (1 - x) CEgIInGaP;
EgXInGaP = (1 - x) EgXGaP + x EgXInP - x (1 - x) CEgXInGaP;

```

```

EgLinGaP = (1 - x) EgLGaP + x EgLinP - x (1 - x) CEgLinGaP;

(* Inx Al1-x P *)
EgΓInAlP = (1 - x) EgΓAlP + x EgΓInP - x (1 - x) CEgΓInAlP;
EgXInAlP = (1 - x) EgXAlP + x EgXInP - x (1 - x) CEgXInAlP;
EgLInAlP = (1 - x) EgLAlP + x EgLinP - x (1 - x) CEgLInAlP;

(*****
  (* Inx (Aly Ga1-y)1-x P *)
  EgΓAlInGaP=(1-y) EgΓInGaP+y EgΓInAlP-y (1-y) CEgΓAlGaP;
  EgXAlInGaP=(1-y) EgXInGaP+y EgXInAlP-y (1-y) CEgXAlGaP;
  EgLAlInGaP=(1-y) EgLInGaP+y EgLInAlP-y (1-y) CEgLAlGaP;
  *****)

EgΓAlInGaP = ABCD[x, y, EgΓ];
EgXAlInGaP = ABCD[x, y, EgX];
EgLAlInGaP = ABCD[x, y, EgL];

(* GaAs1-z Pz *)
EgΓGaAsP = (1 - z) EgΓGaAs + z EgΓGaP - z (1 - z) CEgΓGaAsP;
EgXGaAsP = (1 - z) EgXGaAs + z EgXGaP - z (1 - z) CEgXGaAsP;
EgLGaAsP = (1 - z) EgLGaAs + z EgLGaP - z (1 - z) CEgLGaAsP;

Eg = Min[EgΓAlInGaP, EgXAlInGaP, EgLAlInGaP];
EgGaAsP = Min[EgΓGaAsP, EgXGaAsP, EgLGaAsP];
(** Forcing direct bandgap for calculations on In-rich side of crossover *)
Eg=EgΓAlInGaP III-V reference self consistent,
different crossover points compared to LMM *)

(* Lattice Parameter *)
aInGaP = (1 - x) aGaP + x aInP;
aInAlP = (1 - x) aAlP + x aInP;
(*****aAlInGaP=(1-y) aInGaP+y aInAlP;*****)
aAlInGaP = ABCD[x, y, a];
aGaAsP = (1 - z) aGaAs + z aGaP;

(* Deformation Potentials *)
acInGaP = (1 - x) acGaP + x acInP - x (1 - x) CacInGaP;
acInAlP = (1 - x) acAlP + x acInP - x (1 - x) CacInAlP;
(*****acAlInGaP=(1-y) acInGaP+y acInAlP-y (1-y) CacAlGaP;*****)
acAlInGaP = ABCD[x, y, ac];
avInGaP = (1 - x) avGaP + x avInP - x (1 - x) CavInGaP;
avInAlP = (1 - x) avAlP + x avInP - x (1 - x) CavInAlP;
(*****avAlInGaP=(1-y) avInGaP+y avInAlP-y (1-y) CavAlGaP;*****)
avAlInGaP = ABCD[x, y, av];
bInGaP = (1 - x) bGaP + x bInP - x (1 - x) CbInGaP;
bInAlP = (1 - x) bAlP + x bInP - x (1 - x) CbInAlP;
(*****bAlInGaP=(1-y) bInGaP+y bInAlP-y (1-y) CbAlGaP;*****)
bAlInGaP = ABCD[x, y, b];

(* Valence Band Offsets *)

```

```

VBOInGaP = (1 - x) VBOGaP + x VBOInP;
VBOInAlP = (1 - x) VBOAlP + x VBOInP;
(*****VBOAlInGaP=(1-y) VBOInGaP+y VBOInAlP;*****)
VBOAlInGaP = ABCD[x, y, VBO];

(* Stiffness *)
C11InGaP = (1 - x) C11GaP + x C11InP;
C11InAlP = (1 - x) C11AlP + x C11InP;
(*****C11AlInGaP=(1-y) C11InGaP+y C11InAlP;*****)
C11AlInGaP = ABCD[x, y, C11];
C12InGaP = (1 - x) C12GaP + x C12InP;
C12InAlP = (1 - x) C12AlP + x C12InP;
(*****C12AlInGaP=(1-y) C12InGaP+y C12InAlP;*****)
C12AlInGaP = ABCD[x, y, C12];
C44InGaP = (1 - x) C44GaP + x C44InP;
C44InAlP = (1 - x) C44AlP + x C44InP;
(*****C44AlInGaP=(1-y) C44InGaP+y C44InAlP;*****)
C44AlInGaP = ABCD[x, y, C44];

(* Effective Masses *)
(*****
meInGaP =  $\frac{1}{\frac{1-x}{m_{eGaP}} + \frac{x}{m_{eInP}}}$ ; meInAlP =  $\frac{1}{\frac{1-x}{m_{eGaP}} + \frac{x}{m_{eInP}}}$ ; meAlInGaP =  $\frac{1}{\frac{1-y}{m_{eInGaP}} + \frac{y}{m_{eAlInP}}}$ ;
mlhInGaP =  $\frac{1}{\frac{1-x}{m_{lhGaP}} + \frac{x}{m_{lhInP}}}$ ; mlhInAlP =  $\frac{1}{\frac{1-x}{m_{lhGaP}} + \frac{x}{m_{lhInP}}}$ ; mlhAlInGaP =  $\frac{1}{\frac{1-y}{m_{lhInGaP}} + \frac{y}{m_{lhAlInP}}}$ ;
mhhInGaP =  $\frac{1}{\frac{1-x}{m_{hhGaP}} + \frac{x}{m_{hhInP}}}$ ; mhhInAlP =  $\frac{1}{\frac{1-x}{m_{hhGaP}} + \frac{x}{m_{hhInP}}}$ ; mhhAlInGaP =  $\frac{1}{\frac{1-y}{m_{hhInGaP}} + \frac{y}{m_{hhAlInP}}}$ ;
*****)
EpAlInGaP = ABCD[x, y, Ep];
FA1InGaP = ABCD[x, y, F];
AsoAlInGaP = ABCD[x, y, Aso];
meAlInGaP =  $\frac{m_0}{(1 + 2 FA1InGaP) + \frac{EpAlInGaP (EgFalInGaP - 2 AsoAlInGaP/3)}{EgFalInGaP (EgFalInGaP - AsoAlInGaP)}}$ ;

(* Assuming that the pertinent hole
masses are the 100 masses. Using Luttinger paramters. *)
(* Note that these result in quite different values than
Vurgaftman's "recommended" values despite the fact that
they are calculated in the recommended fashion. *)
mhhGaP =  $\frac{m_0}{\gamma_1GaP - 2 \gamma_2GaP}$ ; mhhAlP =  $\frac{m_0}{\gamma_1AlP - 2 \gamma_2AlP}$ ; mhhInP =  $\frac{m_0}{\gamma_1InP - 2 \gamma_2InP}$ ;
mhhAlInGaP = ABCD[x, y, mhh];
mlhGaP =  $\frac{m_0}{\gamma_1GaP + \gamma_2GaP}$ ; mlhAlP =  $\frac{m_0}{\gamma_1AlP + \gamma_2AlP}$ ; mlhInP =  $\frac{m_0}{\gamma_1InP + \gamma_2InP}$ ;
mlhAlInGaP = ABCD[x, y, mlh];

(* Calculate device parameters *)
(* Put in parameters for relaxation of clad, sch *)
asch = aAlInGaP /. {x → xsch, y → ysch};
aqw = aAlInGaP /. {x → xqw, y → yqw};
C11sch = C11AlInGaP /. {x → xsch, y → ysch};
C12sch = C12AlInGaP /. {x → xsch, y → ysch};
C44sch = C44AlInGaP /. {x → xsch, y → ysch};

```

```

C11qw = C11AlInGaP /. {x → xqw, y → yqw};
C12qw = C12AlInGaP /. {x → xqw, y → yqw};
C44qw = C44AlInGaP /. {x → xqw, y → yqw};
Egclad = Eg /. {x → xclad, y → yclad};
Egsch = Eg /. {x → xsch, y → ysch};
Egblkqw = Eg /. {x → xqw, y → yqw};
meqw = meAlInGaP /. {x → xqw, y → yqw};
mlhqw = mlhAlInGaP /. {x → xqw, y → yqw};
mhhqw = mhhAlInGaP /. {x → xqw, y → yqw};
meb = meAlInGaP /. {x → xsch, y → ysch};
mlhb = mlhAlInGaP /. {x → xsch, y → ysch};
mhbb = mhhAlInGaP /. {x → xsch, y → ysch};
VBOclad = VBOAlInGaP /. {x → xclad, y → yclad};
VBOsch = VBOAlInGaP /. {x → xsch, y → ysch};
VBOqw = VBOAlInGaP /. {x → xqw, y → yqw};
acqw = acAlInGaP /. {x → xqw, y → yqw};
avqw = avAlInGaP /. {x → xqw, y → yqw};
bqw = bAlInGaP /. {x → xqw, y → yqw};

ε =  $\frac{asch - aqw}{aqw}$ ;

(* astar is .05 for tensile and .15 for compressive *)
astar = If[ε > 0, .05, .15];

Gsch = C44sch -  $\frac{2 C44sch + C12sch - C11sch}{2}$ ;
Gqw = C44qw -  $\frac{2 C44qw + C12qw - C11qw}{2}$ ;
Yqw = C11qw + C12qw -  $\frac{2 C12qw^2}{C11qw}$ ;
vqw =  $\frac{C12qw}{C11qw + C12qw}$ ;
bcqw =  $\frac{aqw}{\sqrt{2}}$ ;
α =  $\frac{60}{180 \pi}$ ;

(* Calculate Device Characteristics *)

(* Critical thickness *)
hcomp = astar (Abs[ε])-3/2 * 10-8;
(* To use the M-B crit-thickness calculation,
all parameters must be specified, ie xqw *)
(*hcmb=FindRoot[hc -  $\frac{Gqw Gsch bcqw}{\pi (Gqw + Gsch) (1 - vqw)}$  (1 - vqw) (Cos[α])2  $\frac{(\text{Log}[\frac{hc}{bcqw}] - 1)}{Yqw \text{Abs}[\epsilon]}$ ,
{hc, 2*^-5}][[1]][[2]];*)

(* Strain effect on qw band edges, following Chuang *)

```

```

EstrainCB = 2 acqw  $\left(1 - \frac{C12qw}{C11qw}\right) \epsilon$ ;
Pe = -2 avqw  $\left(1 - \frac{C12qw}{C11qw}\right) \epsilon$ ;
Qe = -bqw  $\left(1 + 2 \frac{C12qw}{C11qw}\right) \epsilon$ ;
EstrainLH = Pe - Qe; (* switching Chuang' s signs,
Estrain > 0 corresponds to increase in bandgap *)
EstrainHH = Pe + Qe;

(* Offset calculation: Starting with difference in SCH and QW bulk gaps,
and using VBO from data, subtract off strain contributions and VBO to get CBO *)
(* Change 1/14/05: Henry Chow suggests better results in InGaAs qw
lasers when CBO, confinement calculated before strain is applied. *)
(* Change back temporarily 2/9/05: calculating offsets after
strains. Leaving both ways in code so can be switched back and forth. *)
(* III-V band structure review paper data, Vurgaftman Meyer *)

(* Henry' s Way: *)
 $\Delta E_{vlh} = -1 * (VBO_{sch} - VBO_{qw}) (*-EstrainLH*)$ ;
 $\Delta E_{vhh} = -1 * (VBO_{sch} - VBO_{qw}) (*-EstrainHH*)$ ;
(* Note that  $\Delta E_c$  is calculated by referencing to hh VB edge *)
 $\Delta E_c = E_{gsch} - E_{gblkqw} - \Delta E_{vhh} (*-EstrainCB*)$ ;

(*****
(* Not Henry' s Way: *)
 $\Delta E_{vlh} = -1 * (VBO_{sch} - VBO_{qw}) - EstrainLH$ ;
 $\Delta E_{vhh} = -1 * (VBO_{sch} - VBO_{qw}) - EstrainHH$ ;
(* Note that  $\Delta E_c$  is calculated by referencing to hh VB edge *)
 $\Delta E_c = E_{gsch} - E_{gblkqw} - \Delta E_{vhh} - EstrainCB$ ;
*****)

(* Old code relocated below. Relocation set 1 *)

(*
(* Now, based on strained bandgaps and alignment,
calculate energy levels due to confinement: *)
(* Square finite quantum well model *)
(* Calculate electron energy levels in CB well *)
(* EngwCB is the energy difference
of the lowest electron level and bottom of the well *)
 $k = \sqrt{\frac{2 m_e q_v E_{ngwCB}}{\hbar^2}}$ ;
EngwCB =
FindRoot[ $\frac{m_{hh}}{m_e q_v} k \tan\left[k \frac{\hbar * 10^{-7}}{2}\right] - \sqrt{\frac{2 m_{hh} (\Delta E_c - E_{ngwCB})}{\hbar^2}}$ , {EngwCB, {0, .01}}] [[1]] [[2]];
(* Calculate for heavy holes in VB well *)
 $k = \sqrt{\frac{2 m_{hh} q_v E_{ngwVBhh}}{\hbar^2}}$ ;
EngwVBhh =

```

```

FindRoot[ $\frac{m_{hh}}{m_{hqw}} k \tan\left[k \frac{h \cdot 10^{-7}}{2}\right] - \sqrt{\frac{2 m_{hh} (\Delta E_{vh} - E_{qwVBhh})}{\hbar^2}}$ , {EnqwVBhh, {0, .01}}][[1]][[2]];
(* Calculate for light holes in VB well *)
k =  $\sqrt{\frac{2 m_{hqw} E_{qwVBlh}}{\hbar^2}}$ ;
EnqwVBlh =
FindRoot[ $\frac{m_{lh}}{m_{hqw}} k \tan\left[k \frac{h \cdot 10^{-7}}{2}\right] - \sqrt{\frac{2 m_{lh} (\Delta E_{vlh} - E_{qwVBlh})}{\hbar^2}}$ , {EnqwVBlh, {0, .01}}][[1]][[2]];
*)

(* Coldren & Corzine,
normalized infinite quantum well approximation for confined levels. *)
(* 1/14/05: note that ΔEv is now the same for lh and
hh. Should change code to calculate confined hh and lh
(ElinfVBlh and ElinfVBhh) resulting in EnqwVBhh and EnqwVBlh *)
ElinfCB =  $\frac{\hbar^2 \pi^2}{2 m_{eqw} (h \cdot 10^{-7})^2}$ ;
ElinfVBhh =  $\frac{\hbar^2 \pi^2}{2 m_{hhqw} (h \cdot 10^{-7})^2}$ ;
ElinfVBlh =  $\frac{\hbar^2 \pi^2}{2 m_{lhqw} (h \cdot 10^{-7})^2}$ ;
nmaxCB =  $\sqrt{\frac{\Delta E_C}{E_{linfCB}}}$ ;
nmaxVBhh =  $\sqrt{\frac{\Delta E_{vh}}{E_{linfVBhh}}}$ ;
nmaxVBlh =  $\sqrt{\frac{\Delta E_{vlh}}{E_{linfVBlh}}}$ ;
nqwCB =  $\frac{2}{\pi} \text{ArcTan}[n_{maxCB} (1 + .6^{n_{maxCB}+1})]$ ;
nqwVBhh =  $\frac{2}{\pi} \text{ArcTan}[n_{maxVBhh} (1 + .6^{n_{maxVBhh}+1})]$ ;
nqwVBlh =  $\frac{2}{\pi} \text{ArcTan}[n_{maxVBlh} (1 + .6^{n_{maxVBlh}+1})]$ ;
EnqwCB = nqwCB2 ElinfCB;
EnqwVBhh = nqwVBhh2 ElinfVBhh;
EnqwVBlh = nqwVBlh2 ElinfVBlh;

(*EnqwCB+Egblkqw+EnqwVBlh
EnqwCB+Egblkqw+EnqwVBhh
EnqwCB=Min[EnqwCBlh,EnqwCBhh];*)

(*If[Im[EnqwCB]≠0|Re[EnqwCB]<0,
Print["Warning: electron level improperly calculated: EnqwCB = ",EnqwCB]]*)
Eelectron = EstrainCB + EnqwCB;

(*
If[Im[EnqwVBhh]≠0|Re[EnqwVBhh]<0,
Print["Warning: heavy hole level improperly calculated: EnqwVBhh = ",EnqwVBhh]]

```

```

If[Im[EnqwVBlh]≠0|Re[EnqwVBlh]<0,
  Print["Warning: light hole level improperly calculated: EnqwVBlh = ",EnqwVBlh]]

If[(EnqwVBlh+EstrainLH)<(EnqwVBhh+EstrainHH),
  Print["Using LH transition."],Print["Using HH transition."]]
*)

(* Note: to make generalized plots,
cannot use Which statement. Must assume hh transition. *)
(*Ehole=Which[Im[EnqwVBlh]≠0|Re[EnqwVBlh]<0,EstrainHH+EnqwVBhh,
  Im[EnqwVBhh]≠0|Re[EnqwVBhh]<0,EstrainLH+EnqwVBlh,
  True,Min[EstrainHH+EnqwVBhh,EstrainLH+EnqwVBlh]];*)
Print["Warning: automatically assuming HH transition"]
Ehole = EstrainHH + EnqwVBhh;
(*Ehole=Min[EnqwVBlh+EstrainLH,EnqwVBhh+EstrainHH];*)

(* Calculate final transition energy and offsets, accounting for strain,
confinement, using the lowest energy LH/HH hole level. *)
Etrans = Egblkqw + Eelectron + Ehole;

(* fix this! *)
(* 1/14/05: ΔEvhh and ΔEvlh are still the same at this point. ΔEc is calculated
with Ehole which takes into account the appropriate lh or hh transition. *)
ΔEc = Egsch - Egblkqw - Eelectron - Ehole - ΔEvhh;
ΔEv = ΔEvhh - EnqwVBhh;

(*Plot[{EnqwCB,EnqwVB,Egblkqw,EstrainCB,EstrainVB,Etrans},
  {xqw,0,1},PlotStyle→{Red,Green,Blue,Purple,Yellow,Black}];
Plot[1000* $\frac{1.24}{Etrans}$ , {xqw,0,1}];*)
ΔEg = Egsch - Egstrnqw // Simplify;
If[ΔEg < .15,
  Print["WARNING: ΔEg is less than 150meV", " ΔEg=", ΔEg], Print["ΔEg=", ΔEg]];

Print["Transition Energy: ", Etrans, " eV"]
Print["Emission Wavelength: ", 1240 / Etrans, " nm"]
Print["CB Offset: ", 1000 * ΔEc, " meV"]
Print["VB Offset: ", 1000 * ΔEv, " meV"]

```

Output of GaAsP and AlInGaP Parameters

```

T = 300;
x = .36;
y = 0.;
z = .459;
Print["GaAsP X = ", 1.24 / EgXGaAsP, "   Γ = ", 1.24 / EgΓGaAsP]
Print["InGaP X = ", 1.24 / EgXAlInGaP, "   Γ = ", 1.24 / EgΓAlInGaP]
EgΓAlInGaP

```

Direct Band Alignment Calculation for Unstrained Layers

```

T = 300;
xclad = .304;
yclad = .446;
xact = .30;
yact = 0;
x = xclad;
y = yclad;
cladCBE = VBOAlInGaP + Eg;
cladVBE = VBOAlInGaP;
Print["clad VB edge = ", VBOAlInGaP, "   clad Eg = ", Eg,
      "   clad CB edge = ", cladCBE, "   clad Γλ = ", 1240 / (EgΓAlInGaP)]
x = xact;
y = yact;
actCBE = VBOAlInGaP + EgΓAlInGaP;
actVBE = VBOAlInGaP;
Print["act VB edge = ", VBOAlInGaP, "   act Eg = ", Eg,
      "   act CB edge = ", actCBE, "   act Γλ = ", 1240 / (EgΓAlInGaP)]
Print["   CBO = ", cladCBE - actCBE, "   VBO = ", actVBE - cladVBE,
      "   TypeII trans = ", cladCBE - actVBE, "   TypeII λ = ", 1240 / (cladCBE - actVBE) ]

(*ΔEc-Eelectron
  1.24/Eg/.{x→.33,y→0}
  aAlInGaP/.{x→.33,y→0}
  Plot [Eg/.y→0,{x,.28,.35}];*)

```

Output of Device Parameters

```
(* xstart now set above *)
(*xstart=.29;*)
λplotList = Array[λplotArray, 7, 0];
ΔEcplotList = Array[ΔEcplotArray, 7, 0];
ΔEvplotList = Array[ΔEvplotArray, 7, 0];
colorList = {Red, Orange, Yellow, Green, Blue, Purple, Black};
(*colorList=
  {CobaltGreen,DarkGreen,Goldenrod,Apricot, Red,DeepCadmiumRed, Black};*)

For[i = 0, i ≤ 6, i++,
  λplotArray[i] = Plot[1240 / Etrans /. xqw → (xstart + xinc i),
    {h, 1, (hcomp * 107) (*50*) /. xqw → (xstart + xinc i)},
    PlotStyle → {colorList[[i + 1]], Thickness[.007]}, DisplayFunction → Identity];
];
For[i = 0, i ≤ 6, i++,
  ΔEcplotArray[i] = Plot[1000 * ΔEc /. xqw → (xstart + xinc i),
    {h, 1, (hcomp * 107) (*50*) /. xqw → (xstart + xinc i)},
    PlotStyle → {colorList[[i + 1]], Thickness[.007]}, DisplayFunction → Identity];
];
For[i = 0, i ≤ 6, i++,
  ΔEvplotArray[i] = Plot[1000 * ΔEv /. xqw → (xstart + xinc i),
    {h, 1, (hcomp * 107) (*50*) /. xqw → (xstart + xinc i)},
    PlotStyle → {colorList[[i + 1]], Dashing[ {.01, .01}], Thickness[.007]},
    DisplayFunction → Identity];
];
Show[λplotList, (*PlotRange→{550,625},*) AxesLabel → {"Lqw (nm)", "λ (nm)"},
  DisplayFunction → $DisplayFunction];
Show[{ΔEcplotList, ΔEvplotList}, PlotRange → {0, 180},
  AxesLabel → {"Lqw (nm)", "ΔEc, ΔEv (meV)"}, DisplayFunction → $DisplayFunction];
```

Plot Platform Alignment

```
VBOc = VBOAlInGaP;
CBOc = VBOAlInGaP + Eg;
p1 = ParametricPlot[{{aAlInGaP108 /. y → 0, VBOc /. y → 0},
  {aAlInGaP108 /. y → 0.2, VBOc /. y → .2}, {aAlInGaP108 /. y → .4, VBOc /. y → .4},
  {aAlInGaP108 /. y → 0.6, VBOc /. y → .6}, {aAlInGaP108 /. y → .8, VBOc /. y → .8},
  {aAlInGaP108 /. y → 1, VBOc /. y → 1}}, {x, 0, 1}, DisplayFunction → Identity,
  PlotStyle → {Red, Orange, Yellow, Green, Blue, Purple}];
p2 = ParametricPlot[{{aAlInGaP108 /. x → 0, VBOc /. x → 0},
  {aAlInGaP108 /. x → 0.2, VBOc /. x → .2}, {aAlInGaP108 /. x → .4, VBOc /. x → .4},
  {aAlInGaP108 /. x → 0.6, VBOc /. x → .6}, {aAlInGaP108 /. x → .8, VBOc /. x → .8},
  {aAlInGaP108 /. x → 1, VBOc /. x → 1}, {aAlInGaP108 /. x → 0.1, VBOc /. x → 0.1},
  {aAlInGaP108 /. x → 0.3, VBOc /. x → .3}, {aAlInGaP108 /. x → .5, VBOc /. x → .5},
  {aAlInGaP108 /. x → 0.7, VBOc /. x → .7}, {aAlInGaP108 /. x → .9, VBOc /. x → .9}},
  {y, 0, 1}, DisplayFunction → Identity];
p3 = ParametricPlot[{{aAlInGaP108 /. y → 0, CBOc /. y → 0},
  {aAlInGaP108 /. y → 0.2, CBOc /. y → .2}, {aAlInGaP108 /. y → .4, CBOc /. y → .4},
  {aAlInGaP108 /. y → 0.6, CBOc /. y → .6}, {aAlInGaP108 /. y → .8, CBOc /. y → .8},
  {aAlInGaP108 /. y → 1, CBOc /. y → 1}}, {x, 0, 1}, DisplayFunction → Identity,
  PlotStyle → {Red, Orange, Yellow, Green, Blue, Purple}];
p4 = ParametricPlot[{{aAlInGaP108 /. x → 0, CBOc /. x → 0},
  {aAlInGaP108 /. x → 0.2, CBOc /. x → .2}, {aAlInGaP108 /. x → .4, CBOc /. x → .4},
  {aAlInGaP108 /. x → 0.6, CBOc /. x → .6}, {aAlInGaP108 /. x → .8, CBOc /. x → .8},
  {aAlInGaP108 /. x → 1, CBOc /. x → 1}, {aAlInGaP108 /. x → 0.1, CBOc /. x → 0.1},
  {aAlInGaP108 /. x → 0.3, CBOc /. x → .3}, {aAlInGaP108 /. x → .5, CBOc /. x → .5},
  {aAlInGaP108 /. x → 0.7, CBOc /. x → .7}, {aAlInGaP108 /. x → .9, CBOc /. x → .9}},
  {y, 0, 1}, DisplayFunction → Identity];
Show[{p1, p2, p3, p4}, FrameLabel → {"Lattice Constant (Å)", "Band Alignment (eV)",
  "", ""}, GridLines → Automatic, Frame → True, DisplayFunction → $DisplayFunction];
```

Plot AlInGaP Eg vs a

```
p1 = ParametricPlot[
  {{aAlInGaP108 /. y → 0, Eg /. y → 0}, {aAlInGaP108 /. y → 0.2, Eg /. y → .2},
  {aAlInGaP108 /. y → .4, Eg /. y → .4}, {aAlInGaP108 /. y → 0.6, Eg /. y → .6},
  {aAlInGaP108 /. y → .8, Eg /. y → .8}, {aAlInGaP108 /. y → 1, Eg /. y → 1}}, {x, 0, 1},
  DisplayFunction → Identity, PlotStyle → {Red, Orange, Yellow, Green, Blue, Purple}];
p2 = ParametricPlot[{{aAlInGaP108 /. x → 0, Eg /. x → 0},
  {aAlInGaP108 /. x → 0.2, Eg /. x → .2}, {aAlInGaP108 /. x → .4, Eg /. x → .4},
  {aAlInGaP108 /. x → 0.6, Eg /. x → .6}, {aAlInGaP108 /. x → .8, Eg /. x → .8},
  {aAlInGaP108 /. x → 1, Eg /. x → 1}, {aAlInGaP108 /. x → 0.1, Eg /. x → 0.1},
  {aAlInGaP108 /. x → 0.3, Eg /. x → .3}, {aAlInGaP108 /. x → .5, Eg /. x → .5},
  {aAlInGaP108 /. x → 0.7, Eg /. x → .7}, {aAlInGaP108 /. x → .9, Eg /. x → .9}},
  {y, 0, 1}, DisplayFunction → Identity];
p3 = ParametricPlot[{aGaAsP108, EgGaAsP}, {z, 0, 1},
  AxesLabel → {"a (cm)", "Eg"}, DisplayFunction → Identity];
Show[{p1, p2, p3}, FrameLabel → {"Lattice Constant (Å)", "Bandgap (eV)", "", ""},
  GridLines → Automatic, Frame → True, DisplayFunction → $DisplayFunction];
```

AllnGaP Calibration Calculation

```
(* Note that to solve for x and y simultaneously,
Mathematica has to have a nicely behaving function to work with,
so I define aFast and EgGammaFast. These are nice to work with,
but blow up at x=0 or y=0, so they are not good for plotting. *)
aFast =
  (x (1 - x) (1 - y) ( ( (1 - x + (1 - x) (1 - y)) / 2 ) aGaP + ( 1 - ( (1 - x + (1 - x) (1 - y)) / 2 ) ) aInP ) +
  ((x - 1)^2 (1 - y) y)
  ( ( (2 - x - 2 ((1 - x) (1 - y))) / 2 ) aAlP + ( 1 - ( (2 - x - 2 ((1 - x) (1 - y))) / 2 ) ) aGaP ) + x y
  (1 - x) ( ( (2 - 2 x - ((1 - x) (1 - y))) / 2 ) aAlP + ( 1 - ( (2 - 2 x - ((1 - x) (1 - y))) / 2 ) ) aInP ) ) /
  ((1 - x) (x + y - x y - y^2 + x y^2));
EgGammaFast = (x (1 - x) (1 - y) ( ( (1 - x + (1 - x) (1 - y)) / 2 ) EgGammaGaP +
  ( 1 - ( (1 - x + (1 - x) (1 - y)) / 2 ) ) EgGammaInP - ( (1 - x + (1 - x) (1 - y)) / 2 )
  ( 1 - ( (1 - x + (1 - x) (1 - y)) / 2 ) ) CEgGammaInGaP ) + ((x - 1)^2 (1 - y) y)
  ( ( (2 - x - 2 ((1 - x) (1 - y))) / 2 ) EgGammaAlP + ( 1 - ( (2 - x - 2 ((1 - x) (1 - y))) / 2 ) ) EgGammaGaP -
  ( (2 - x - 2 ((1 - x) (1 - y))) / 2 ) ( 1 - ( (2 - x - 2 ((1 - x) (1 - y))) / 2 ) ) CEgGammaAlGaP ) +
  x y (1 - x) ( ( (2 - 2 x - ((1 - x) (1 - y))) / 2 ) EgGammaAlP + ( 1 - ( (2 - 2 x - ((1 - x) (1 - y))) / 2 ) )
  EgGammaInP - ( (2 - 2 x - ((1 - x) (1 - y))) / 2 ) ( 1 - ( (2 - 2 x - ((1 - x) (1 - y))) / 2 ) )
  CEgGammaInAlP ) ) / ((1 - x) (x + y - x y - y^2 + x y^2));

CLWavelength = 561;
RelaxedLatticeConstant = 5.65325;
NSolve[{1.24*^3 / EgGammaFast == CLWavelength, aFast * 10^8 == RelaxedLatticeConstant}, {x, y}];

Solve[1.24 / .643 == EgGaAsP]

Show[lambdaPlotList, (*PlotRange->{550,625},*)AxesLabel->{"L_qv (nm)", "lambda (nm)"},
  AspectRatio->1.5, TextStyle->{FontSize->12},
  DisplayFunction-> $DisplayFunction];
Show[{deltaEPlotList, deltaEvPlotList}, PlotRange->{0, 100},
  AxesLabel->{"L_qv (nm)", "deltaE_c, deltaE_v (meV)"}, AspectRatio->1.5,
  TextStyle->{FontSize->12}, DisplayFunction-> $DisplayFunction];
```

```

EnqwCB
EstrainCB
Egsch - Egblkqw - EstrainCB - EstrainHH
Egblkqw + EstrainCB + EstrainHH
ΔEvhh
EstrainHH
EnqwVBhh
ΔEv
Egblkqw
Etrans

```

Plot Band Schematic

```

(* Band schematic *)
(*h=5*^-7;*)
tclad = 200;
tsch = 100;
tqw = 10;
ttot = 2 tclad + 2 tsch + tqw;
Evsch = VBOsch - VBOclad;
Evqw = VBOqw - VBOclad;
      (*(* Assuming Type I offset *)
      Evsch=.45 (Egclad-Egsch);
      Evqw=.45 (Egclad-Egblkqw);*)
Evdevice[z_] := 0 /; z < tclad
Evdevice[z_] := Evsch /; tclad ≤ z ≤ tclad + tsch
Evdevice[z_] := Evqw /; tclad + tsch < z ≤ tclad + tsch + tqw
Evdevice[z_] := Evsch /; tclad + tsch + tqw < z ≤ tclad + 2 tsch + tqw
Evdevice[z_] := 0 /; z > tclad + 2 tsch + tqw
Ecdevice[z_] := Egclad /; z < tclad
Ecdevice[z_] := Evsch + Egsch /; tclad ≤ z ≤ tclad + tsch
Ecdevice[z_] := Evqw + Egstrnqw /; tclad + tsch < z ≤ tclad + tsch + tqw
Ecdevice[z_] := Evsch + Egsch /; tclad + tsch + tqw < z ≤ tclad + 2 tsch + tqw
Ecdevice[z_] := Egclad /; z > tclad + 2 tsch + tqw
Evqwlevel[z_] := Evdevice[z] /; z ≤ tclad + tsch
Evqwlevel[z_] := Evqw - EnqwVB /; tclad + tsch < z < tclad + tsch + tqw
Evqwlevel[z_] := Evdevice[z] /; z ≥ tclad + tsch + tqw
Ecqwlevel[z_] := Ecdevice[z] /; z ≤ tclad + tsch
Ecqwlevel[z_] := Evqw + Egstrnqw + EnqwCB /; tclad + tsch < z < tclad + tsch + tqw
Ecqwlevel[z_] := Ecdevice[z] /; z ≥ tclad + tsch + tqw
Plot[{Ecqwlevel[z], Ecdevice[z]},
      {z, 0, ttot}, PlotStyle → {Green, Red}, PlotRange → {2., 2.35}];
Plot[{Evqwlevel[z], Evdevice[z]}, {z, 0, ttot},
      PlotStyle → {Green, Blue}, PlotRange → {-.05, .3}];

```

```

Plot3D[Abs[1240 / Etrans /. h -> 5*^-7], {xqw, 0, 1}, {yqw, 0, 1},
PlotPoints -> 30, AxesLabel -> {"xqw", "yqw", "\lambda"}, FaceGrids -> All];
Plot3D[Abs[Etrans /. h -> 5*^-7], {xqw, 0, 1}, {yqw, 0, 1},
PlotPoints -> 30, AxesLabel -> {"xqw", "yqw", "\lambda"}];

Print["ysch=", ysch]
Print["xsch=", xsch]
Plot3D[ΔEc, {xqw, 0, 1}, {yqw, 0, 1}, PlotPoints -> 30,
AxesLabel -> {"xqw", "yqw", "ΔEc"}, ViewPoint -> {1.3, -2.4, 1}, FaceGrids -> All];
Plot3D[ΔEv, {xqw, 0, 1}, {yqw, 0, 1}, PlotPoints -> 30,
AxesLabel -> {"xqw", "yqw", "ΔEv"}];

(*ContourPlot[ΔEc, {xqw, 0, 1},
{yqw, 0, 1}, PlotPoints -> 30, AxesLabel -> {"xqw", "yqw"}]
ContourPlot[ΔEv, {xqw, 0, 1}, {yqw, 0, 1}, PlotPoints -> 30,
AxesLabel -> {"xqw", "yqw"}]
ShowLegend[ContourPlot[ΔEc, {xqw, 0, 1}, {yqw, 0, 1},
PlotPoints -> 30, AxesLabel -> {"xqw", "yqw"}],
{GrayLevel[1-#]&, 10, " 1", "-1", LegendPosition -> {1.1, -.4}}];
ContourPlot[ΔEv, {xqw, 0, 1}, {yqw, 0, 1}, PlotPoints -> 30,
AxesLabel -> {"xqw", "yqw"}];*)

ParametricPlot[
{{aAlInGaP /. y -> 0, EgΓAlInGaP /. y -> 0}, {aAlInGaP /. y -> 0.2, EgΓAlInGaP /. y -> .2},
{aAlInGaP /. y -> .4, EgΓAlInGaP /. y -> .4}, {aAlInGaP /. y -> 0.6, EgΓAlInGaP /. y -> .6},
{aAlInGaP /. y -> .8, EgΓAlInGaP /. y -> .8}, {aAlInGaP /. y -> 1, EgΓAlInGaP /. y -> 1},
{aAlInGaP /. y -> 0, EgXAlInGaP /. y -> 0}, {aAlInGaP /. y -> 0.2, EgXAlInGaP /. y -> .2},
{aAlInGaP /. y -> .4, EgXAlInGaP /. y -> .4}, {aAlInGaP /. y -> 0.6, EgXAlInGaP /. y -> .6},
{aAlInGaP /. y -> .8, EgXAlInGaP /. y -> .8}, {aAlInGaP /. y -> 1, EgXAlInGaP /. y -> 1},
{aAlInGaP /. y -> 0, EgLAlInGaP /. y -> 0}, {aAlInGaP /. y -> 0.2, EgLAlInGaP /. y -> .2},
{aAlInGaP /. y -> .4, EgLAlInGaP /. y -> .4}, {aAlInGaP /. y -> 0.6, EgLAlInGaP /. y -> .6},
{aAlInGaP /. y -> .8, EgLAlInGaP /. y -> .8}, {aAlInGaP /. y -> 1, EgLAlInGaP /. y -> 1}},
{x, 0, 1}, PlotRange -> {1, 2.6}, AxesOrigin -> {5.44*^-8, 1}, GridLines -> Automatic,
Frame -> True, PlotStyle -> {Red, Red, Red, Red, Red, Red, Blue, Blue,
Blue, Blue, Blue, Blue, Green, Green, Green, Green, Green, Green,}}];

p1 = ParametricPlot[{{aAlInGaP /. y -> 0, Eg /. y -> 0}, {aAlInGaP /. y -> 0.2, Eg /. y -> .2},
{aAlInGaP /. y -> .4, Eg /. y -> .4}, {aAlInGaP /. y -> 0.6, Eg /. y -> .6},
{aAlInGaP /. y -> .8, Eg /. y -> .8}, {aAlInGaP /. y -> 1, Eg /. y -> 1}},
{x, 0, 1}, AxesLabel -> {"a (cm)", "Eg"}, DisplayFunction -> Identity];
p2 = ParametricPlot[{{aAlInGaP /. x -> 0, Eg /. x -> 0},
{aAlInGaP /. x -> 0.2, Eg /. x -> .2}, {aAlInGaP /. x -> .4, Eg /. x -> .4},
{aAlInGaP /. x -> 0.6, Eg /. x -> .6}, {aAlInGaP /. x -> .8, Eg /. x -> .8},
{aAlInGaP /. x -> 1, Eg /. x -> 1}, {aAlInGaP /. x -> 0.1, Eg /. x -> 0.1},
{aAlInGaP /. x -> 0.3, Eg /. x -> .3}, {aAlInGaP /. x -> .5, Eg /. x -> .5},
{aAlInGaP /. x -> 0.7, Eg /. x -> .7}, {aAlInGaP /. x -> .9, Eg /. x -> .9}},
{y, 0, 1}, AxesLabel -> {"a (cm)", "Eg"}, DisplayFunction -> Identity];
p3 = ParametricPlot[{{aGaAsP, EgGaAsP}, {z, 0, 1},
AxesLabel -> {"a (cm)", "Eg"}, DisplayFunction -> Identity];
Show[{p1, p2, p3}, PlotRange -> {1, 2.6}, AxesOrigin -> {5.44*^-8, 1},
GridLines -> Automatic, Frame -> True, DisplayFunction -> $DisplayFunction];

```

Critical Thickness Calculations

```
Plot[{astar (Abs[ε])-3/2,
      108 * FindRoot[hc -  $\frac{G_{qw} G_{sch} b}{\pi (G_{qw} + G_{sch}) (1 - v_{qw})} (1 - v_{qw} (\cos[\alpha])^2) \frac{(\log[\frac{hc}{b}] + 1)}{Y_{qw} \text{Abs}[\epsilon]}$ ,
                    {hc, 2-5}]][[1]][[2]], {xqw, 0, 1},
      PlotRange → {0, 1000}, AxesLabel → {"xqw", "hc (Ang)"}, PlotStyle → {Red, Blue},
      PlotLegend → {"empir.", "M-B"},
      LegendPosition → {0, 0}, LegendSpacing → 0];
```

References

- 1 R. Stevenson, Four-Pronged Attack Promises Ultra-High Efficiency Lighting, 2008), p. 25.
- 2 Optoelectronics Industry Development Association (OIDA), Light Emitting Diodes (LEDs) for General Illumination, (Optoelectronics Industry Development Association (OIDA), 2002).
- 3 L. M. McGill, MOCVD Growth of InGaP-Based Heterostructures for Light Emitting Devices, Doctoral Thesis (MIT, Cambridge, MA, 2004).
- 4 J. M. Phillips, M. E. Coltrin, M. H. Crawford, A. J. Fischer, M. R. Krames, R. Mueller-Mach, G. O. Mueller, Y. Ohno, L. E. S. Rohwer, J. A. Simmons, and J. Y. Tsao, *Laser & Photonics Reviews* 1, 4 (2007).
- 5 R. F. Pierret, Semiconductor Device Fundamentals, (Addison-Wesley, 1996).
- 6 K. Chilukuri, M. J. Mori, C. L. Dohrman, and E. A. Fitzgerald, *Semiconductor Science and Technology* 22, 2 (2007).
- 7 I. Vurgaftman, J. R. Meyer, and L. R. Ram-Mohan, *J. Appl. Phys.* 89, 11 (2001).
- 8 S. L. Chuang, Physics of Optoelectronic Devices, (Wiley Interscience, 1995).
- 9 J. W. Matthews, A. E. Blakeslee, and S. Mader, *Thin Solid Films* 33, 2 (1976).
- 10 J. W. Matthews, and A. E. Blakeslee, *J. Cryst. Growth* 29, 3 (1975).
- 11 J. W. Matthews, and A. E. Blakeslee, *J. Cryst. Growth* 27, DEC (1974).
- 12 A. Y. Kim, Co-Evolution of Microstructure and Dislocation Dynamics in InGaP/GaP: Engineering High Quality Epitaxial Transparent Substrates, Doctoral Thesis (MIT, Cambridge, MA 2000).
- 13 J. P. Hirth, and J. Lothe, Theory of Dislocations, 2nd ed. (Wiley, New York, 1982).
- 14 D. Hull, and D. J. Bacon, Introduction to Dislocations, 3rd Ed. (Pergamon Press, Oxford, 1984).
- 15 F. R. N. Nabarro, Theory of Crystal Dislocations, (Clarendon Press, Oxford, 1967).
- 16 J. Weertman, and J. R. Weertman, Elementary Dislocation Theory, (Macmillan, New York, 1964).
- 17 M. J. Matragrano, J. R. Shealy, and V. Krishnamoorthy, *J. Appl. Phys.* 79, 11 (1996).
- 18 J. W. Matthews, Epitaxial Growth: Part B, (Academic Press, New York, 1975).

- 19 A. J. Pitera, Engineered Substrates for Coplanar Integration of Lattice-Mismatched Semiconductors with Silicon, Doctoral Thesis (MIT, Cambridge, MA, 2005).
- 20 E. A. Fitzgerald, *Material Science Reports* 7, 3 (1991).
- 21 C. C. Hu, C. S. Sheu, and M. K. Lee, *Mater. Chem. Phys.* 48, 1 (1997).
- 22 T. Egawa, T. Jimbo, J. Dong, K. Matsumoto, and M. Umeno, *Appl. Phys. Lett.* 67, 24 (1995).
- 23 Y. Komatsu, K. Hosotani, T. Fuyuki, and H. Matsunami, *Japanese Journal of Applied Physics Part 1-Regular Papers Short Notes & Review Papers* 36, 9A (1997).
- 24 S. Makan, Growth and Characterization of Mismatched Indium Gallium Phosphide Films for Reduced Area Dislocation Filtering, Master Thesis. (MIT, Cambridge, MA, 1997).
- 25 E. A. Fitzgerald, Y. - Xie, D. Monroe, P. J. Silverman, J. M. Kuo, A. R. Kortan, F. A. Thiel, and B. E. Weir, Relaxed $\text{Ge}_x\text{Si}_{1-x}$ Structures for III-V Integration with Si and High Mobility Two-Dimensional Electron Gases in Si, Death Valley, CA, USA, 1992), p. 1807.
- 26 E. A. Fitzgerald, Y. H. Xie, M. L. Green, D. Brasen, A. R. Kortan, J. Michel, Y. J. Mii, and B. E. Weir, *Appl. Phys. Lett.* 59, 7 (1991).
- 27 S. B. Samavedam, and E. A. Fitzgerald, *J. Appl. Phys.* 81, 7 (1997).
- 28 R. M. Sieg, J. A. Carlin, S. A. Ringel, M. T. Currie, S. M. Ting, T. A. Langdo, G. Taraschi, E. A. Fitzgerald, and B. M. Keyes, *Appl. Phys. Lett.* 73, 21 (1998).
- 29 A. Y. Kim, and E. A. Fitzgerald, Engineering High quality $\text{In}_x\text{Ga}_{1-x}\text{P}$ Graded Composition Buffers on GaP for Transparent Substrate Light-Emitting Diodes, (SPIE-Int. Soc. Opt. Eng, San Jose, CA, USA, 1999), p. 179.
- 30 L. McGill, J. W. Wu, and E. A. Fitzgerald, *J. Appl. Phys.* 95, 12 (2004).
- 31 M. E. Groenert, C. W. Leitz, A. J. Pitera, V. K. Yang, H. Lee, R. J. Ram, and E. A. Fitzgerald, Strategies for Direct Monolithic Integration of $\text{Al}_x\text{Ga}_{(1-x)}\text{As}/\text{In}_x\text{Ga}_{(1-x)}\text{As}$ LEDs and Lasers on Ge/GeSi/Si Substrates Via Relaxed Graded $\text{Ge}_x\text{Si}_{(1-x)}$ Buffer Layers, (Mater. Res. Soc, Boston, MA, USA, 2002), p. 513.
- 32 M. S. Abrahams, and J. J. Tietjen, Stacking Faults in $\text{GaAs}_{1-x}\text{P}_x$ Alloys, 1969), p. 2491.
- 33 M. S. Abrahams, L. R. Weisberg, C. J. Buiocchi, and J. Blanc, Dislocation Morphology in Graded Heterojunctions: $\text{GaAs}_{1-x}\text{P}_x$, 1969), p. 223.

- 34 M. S. Abrahams, L. R. Weisberg, and J. J. Tietjen, Stresses in Heteroepitaxial Layers: GaAs_{1-x}P_x on GaAs, 1969), p. 3754.
- 35 C. W. Leitz, M. T. Currie, A. Y. Kim, J. Lai, E. Robbins, E. A. Fitzgerald, and M. T. Bulsara, *J. Appl. Phys.* 90, 6 (2001).
- 36 G. B. Stringfellow, *Organometallic Vapor-Phase Epitaxy: Theory and Practice*, (Academic Press, 1989).
- 37 Y. P. Varshni, *Physica* 34, 149 (1967).
- 38 T. H. Glisson, J. R. Hauser, M. A. Littlejohn, and C. K. Williams, *J Electron Mater* 7, 1 (1978).
- 39 C. K. Williams, T. H. Glisson, J. R. Hauser, and M. A. Littlejohn, *J Electron Mater* 7, 5 (1978).
- 40 H. P. Hsu, Y. S. Huang, C. H. Wu, Y. K. Su, F. S. Juang, Y. G. Hong, and C. W. Tu, *Journal of Physics-Condensed Matter* 16, 31 (2004).
- 41 L. M. McGill, E. A. Fitzgerald, A. Y. Kim, J. -. Huang, S. S. Yi, P. N. Grillo, and S. A. Stockman, *Journal of Vacuum Science & Technology B (Microelectronics and Nanometer Structures)* 22, 4 (2004).
- 42 L. A. Coldren, and S. W. Corzine, *Diode Lasers and Photonic Integrated Circuits*, (Wiley Interscience, 1995).
- 43 J. S. Yuan, M. T. Tsai, C. H. Chen, R. M. Cohen, and G. B. Stringfellow, *J. Appl. Phys.* 60, 4 (1986).
- 44 H. Protzmann, F. Hohnsdorf, Z. Spika, W. Stolz, E. O. Gobel, M. Muller, and J. Lorberth, *J. Cryst. Growth* 170, 1-4 (1997).
- 45 R. M. Sieg, S. A. Ringel, S. M. Ting, E. A. Fitzgerald, and R. N. Sacks, *J Electron Mater* 27, 7 (1998).
- 46 A. Y. Kim, W. S. McCullough, and E. Fitzgerald, *Journal of Vacuum Science & Technology B (Microelectronics and Nanometer Structures)* 17, 4 (1999).
- 47 D. S. Cao, C. H. Chen, K. L. Fry, E. H. Reihlen, and G. B. Stringfellow, *J. Appl. Phys.* 65, 6 (1989).
- 48 M. J. Jou, J. F. Lin, C. M. Chang, C. H. Lin, M. C. Wu, and B. J. Lee, *Japanese Journal of Applied Physics Part 1-Regular Papers Short Notes & Review Papers* 32, 10 (1993).
- 49 J. F. Lin, M. C. Wu, M. J. Jou, C. M. Chang, and B. J. Lee, *J. Cryst. Growth* 137, 3-4 (1994).

- 50 T. Tanaka, K. Uchida, Y. Ishitani, and S. Minagawa, *Appl. Phys. Lett.* 66, 7 (1995).
- 51 M. S. Abrahams, C. J. Buiocchi, and G. H. Olsen, *J. Appl. Phys.* 46, 10 (1975).
- 52 W. G. Bi, and C. W. Tu, *J. Cryst. Growth* 165, 3 (1996).
- 53 T. P. Chin, J. C. P. Chang, K. L. Kavanagh, C. W. Tu, P. D. Kirchner, and J. M. Woodall, *Appl. Phys. Lett.* 62, 19 (1993).
- 54 N. J. Quitoriano, and E. A. Fitzgerald, *J. Appl. Phys.* 101, 7 (2007).
- 55 N. J. Quitoriano, and E. A. Fitzgerald, *J. Appl. Phys.* 102, 3 (2007).
- 56 I. Yonenaga, and K. Sumino, *J. Appl. Phys.* 73, 4 (1993).
- 57 I. Yonenaga, and K. Sumino, *J. Appl. Phys.* 71, 9 (1992).
- 58 I. Yonenaga, and K. Sumino, *Appl. Phys. Lett.* 58, 1 (1991).
- 59 A. Zunger, and S. Mahajan, *Handbook on Semiconductors; Vol. 3b*, (Elsevier, Amsterdam, 1994), p. 1402-1507.
- 60 Z. Wu, K. Lu, Y. Wang, J. Dong, H. Li, C. Li, and Z. Fang, *Physical Review B* 48, 12 (1993).
- 61 G. B. Stringfellow, *J. Cryst. Growth* 27, DEC (1974).
- 62 F. Cleton, B. Sieber, A. Bensaada, R. A. Masut, J. M. Bonard, and J. D. Ganiere, *J. Appl. Phys.* 80, 2 (1996).
- 63 F. Cleton, B. Sieber, A. Lefebvre, A. Bensaada, R. A. Masut, J. M. Bonard, J. D. Ganiere, and M. Ambri, *J. Appl. Phys.* 80, 2 (1996).
- 64 M. Kondow, H. Kakibayashi, S. Minagawa, Y. Inoue, T. Nishino, and Y. Hamakawa, *J. Cryst. Growth* 93, 1-4 (1988).
- 65 T. Suzuki, A. Gomyo, and S. Iijima, *J. Cryst. Growth* 93, 1-4 (1988).
- 66 C. H. Chen, S. A. Stockman, and M. J. Peanasky, *OMVPE Growth of AlInGaP for High-Efficiency Visible LEDs*, 1997), p. 97.
- 67 M. Zorn, P. Kurpas, A. I. Shkrebtii, B. Junno, A. Bhattacharya, K. Knorr, M. Weyers, L. Samuelson, J. T. Zettler, and W. Richter, *Physical Review B* 60, 11 (1999).
- 68 G. B. Stringfellow, L. C. Su, Y. E. Strausser, and J. T. Thornton, *Appl. Phys. Lett.* 66, 23 (1995).
- 69 G. B. Stringfellow, D. C. Chapman, B. J. Kim, and T. Y. Seong, *Electrochemical Proceedings Vol. 2003-08*, 2003).

- 70 S. R. Kurtz, J. M. Olson, and A. Kibbler, *Appl. Phys. Lett.* 57, 18 (1990).
- 71 K. A. Mader, and A. Zunger, *Appl. Phys. Lett.* 64, 21 (1994).
- 72 D. S. Cao, A. W. Kimball, and G. B. Stringfellow, *J. Appl. Phys.* 67, 2 (1990).
- 73 S. J. Chang, J. K. Sheu, Y. K. Su, M. J. Jou, and G. C. Chi, *Japanese Journal of Applied Physics Part 1-Regular Papers Short Notes & Review Papers* 35, 8 (1996).
- 74 F. A. Kish, D. A. Defever, D. A. Vanderwater, G. R. Trott, R. J. Weiss, and J. S. Major, *Electron. Lett.* 30, 21 (1994).
- 75 F. A. Kish, F. M. Steranka, D. C. Defever, D. A. Vanderwater, K. G. Park, C. P. Kuo, T. D. Osentowski, M. J. Peanasky, J. G. Yu, R. M. Fletcher, D. A. Steigerwald, M. G. Craford, and V. M. Robbins, *Appl. Phys. Lett.* 64, 21 (1994).
- 76 F. Much, M. Ahr, M. Biehl, and W. Kinzel, *Europhys. Lett.* 56, 6 (2001).
- 77 S. Tiwari, and D. J. Frank, *Appl. Phys. Lett.* 60, 5 (1992).
- 78 T. F. Lei, and G. K. Jeng, *Solid-State Electronics* 31, 1 (1988).
- 79 B. J. Li, E. K. Liu, and F. J. Zhang, *Solid-State Electronics* 41, 6 (1997).